To the Graduate Council:

I am submitting herewith a thesis written by Walter Norbert Fett entitled "The Biaxial Fatigue of Decarburized Steel." I have examined the final copy of this thesis for form and content and recommend that it be accepted in partial fulfillment of the requirements for the degree of Master of Science, with a major in Metallurgical Engineering.

W. T. Becker

William T. Becker, Major Professor

We have read this thesis
and recommend its acceptance:

Eric I. Allen

Archie Mathews

Accepted for the Council:

L. Evans Reed

Vice Chancellor
Graduate Studies and Research

THE BIAXIAL FATIGUE OF DECARBURIZED STEEL

A Thesis

Presented for the

Master of Science

Degree

The University of Tennessee, Knoxville

Walter Norbert Fett

March 1982

ACKNOWLEDGMENT

The author wishes to extend his gratitude to Dr. W. T. Becker, Associate Professor in the Department of Chemical, Metallurgical, and Polymer Engineering at The University of Tennessee for the opportunity to do graduate level research in the mechanical properties area. Dr. A. Mathews, Associate Professor in the Department of Engineering Science and Mechanics provided guidance in the operation of the fatigue machine and the use of laboratory space for the machine. Dr. B. F. Oliver, Professor in the Department of Chemical, Metallurgical, and Polymer Engineering has provided the author a great deal of encouragement to finish this research. Mr. H. B. Thompson, Supervisor, and Mr. J. G. French of the Machine Shop prepared the specimens. Mr. B. L. McGill, Senior Engineering Technician provided instruction and guidance in the operation of the Scanning Electron Microscope. Jennifer Leslie was typist for the thesis.

The author would also like to thank all those who gave technical or non-technical advise which includes almost everyone in the Department of Chemical, Metallurgical, and Polymer Engineering.

ABSTRACT

A completely reversed loading fatigue test program was used to determine the effect of the type of loading (bending or torsion) on the fatigue properties of SAE 1042 steel. The program utilized two series of specimens, decarburized (with a 0.042 inch decarburized layer) and non-decarburized. The results of the fatigue tests were analyzed using modern statistical curve fitting techniques. The results of the fatigue tests in bending and torsion were compared using multiaxial failure criteria, either the maximum shear stress criterion or the maximum octahedral shear stress criterion.

Examination of the fractured fatigue specimens by scanning electron microscopy (SEM) revealed important information on the macroscopic fracture modes of specimens tested in bending and torsion.

Some higher magnification SEM pictures are included to show the microscopic fracture appearance. Because of the microstructure of the material used, identification of features unique to fatigue failure was difficult.

In addition, surface roughness tests, tensile tests, microhardness tests, and metallography were used to characterize the properties and microstructure of the specimens.

In summary, the study showed that:

1. Decarburization lowers the hardness and decreases the amount of pearlite present in the surface layer of SAE 1042 steel.
2. Decarburization has only a slight effect on monotonic tensile properties.

3. The presence of a decarburized surface layer reduces fatigue strength and the fatigue limit in both bending and torsion.
4. When comparing fatigue strengths and the fatigue limit in bending and torsion, it was found that failure criteria based on an equivalent stress concept can be applied at 10^7 cycles, but not for fatigue strengths at less than 10^6 cycles.
5. Macroscopic fracture modes of specimens tested in bending and torsion were found to be quite different, although for both types of loading, crack propagation was observed on planes of maximum normal stress.
6. Using previous data as a comparison, it was found that the present data for fatigue life are dominated by cycles spent in fatigue crack propagation.

The fatigue properties were discussed in relation to fatigue processes and the fatigue testing machine.

TABLE OF CONTENTS

LIST OF TABLES

LIST OF FIGURES

FIGURE PAGE

FIGURE PAGE

INTRODUCTION

This research was undertaken to extend studies of the effect of decarburization on the fatigue behavior of plain carbon steels initiated by D. A. Bales (1). In the present study using normalized SAE 1042 steel, specimens were tested in bending and in torsion in both the decarburized and non-decarburized conditions. The fatigue limit and fatigue strength for the two types of loading are compared using accepted multiaxial failure criteria. In addition, macrofractography and microfractography were performed in an attempt to correlate fractographic features with the type of loading as well as the magnitude of the applied stress.

Fatigue failures have been recognized since the middle of the nineteenth century as the cause of failure of metals undergoing fluctuating stresses and strains. In 1903, the first metallographic study of fatigue crack initiation and propagation was done (reviewed by Fine (2)). This research is the basis for our present-day understanding of fatigue processes. Fatigue may be defined as:

> The process of progressive localized permanent structural change occurring in a material subjected to conditions which produce fluctuating stresses and strains at some point or points and which may culminate in cracks or complete fracture after a sufficient number of fluctuations. (3)

Most fatigue tests are done in bending or axial loading, giving a one-dimensional (uniaxial) state of stress in principal stress space. In torsion, there are shear stresses on a transverse cross section which result from the twisting action. These shear stresses generate two principal stresses of equal magnitude, but opposite sign, acting 90° apart in the body on planes rotated 45° from the applied torsion

stresses. The result is a biaxial state of stress in principal stress space.

It is of considerable interest in design to prevent fatigue failure to be able to predict failure for biaxial states of stress by using data from uniaxial tests and an equivalent stress failure criterion. Consequently, the data collected in this study are used to compare the degree to which the two most common failure criteria (maximum shear stress and octahedral shear stress) can predict the behavior of the decarburized specimens.

Fatigue failure criteria are usually given in terms of the stress or strain that a material can endure for a given number of cycles. A calculated value of stress for failure at an exact number of cycles is the fatigue strength. The limiting value as the number of cycles becomes very large is the fatigue limit or the endurance limit.

CHAPTER I

LITERATURE REVIEW

Decarburization

Decarburization is the loss of carbon from the surface of a ferrous alloy as a result of heating in an atmosphere that reacts with carbon at the surface. This is a common problem that may occur during forging or hot rolling or if furnace atmospheres are not controlled during heat treatment.

Fatigue failures. The effect of surface condition, including decarburization, on the fatigue properties was first investigated as a cause of the failure of leaf springs in the early 1930's (4, 5). These leaf springs were used in the as-forged condition. Decarburized steel wire for use as wire rope has also been the subject of fatigue investigations (6). The fatigue properties of as-forged or shot-peened axle shafts was investigated in 1951, where decarburization was an additional variable (7). With the advent of new aircraft designs in 1961, decarburization became a concern. Alloy sheet steel which had been heat treated to high strength levels was used for airframe parts (8). Here, the fatigue limit was lowered significantly by a small amount of decarburization. Decarburization was still of concern in the 1970's when Shah (9) examined failures of aircraft components. Decarburization in a layer 0.10 to 0.015 inch (0.25 to 0.38 mm) deep was found in a variety of forgings. A connecting rod and the exhaust rocker arms in an aircraft engine were decarburized. Also, main rotor drag brace clevises bolts, and the spring legs of the main landing gear were found to be

decarburized. In one instance, decarburization of a layer 0.010 to 0.030 inch (0.25 to 0.76 mm) deep was found in the failure of a spring leg of the main landing gear. This component had failed in fatigue and the decarburization was found to be a contributing factor.

Bales (1) has reviewed the literature on the fatigue of decarburized steels, pointing out the lack of quantitative data supporting the statements that decarburization is detrimental to fatigue life. There is still dispute over the degree of damage caused by decarburization. Gassner (10) has stated that a little decarburization may not be that bad. Gassner defined decarburization in terms of depth and severity. The depth is the distance below the surface where the hardness has risen to that of the core. Severity is the difference between the minimum specified hardness and the hardness at the surface. The data available in the open literature do not clearly define the amount of decarburization and the resultant fatigue performance.

It is common practice to use copper plating to protect parts where 0.003 inch (0.076 mm) maximum decarburization is specified. The copper plating is an effective barrier to carbon diffusion, but does add an extra expense to the price of heat treating.

Processes. Nauman and Spies (11) have described the fundamentals of decarburization in steels. In slightly oxidizing atmospheres, the rate of decarburization depends on the rate of diffusion of carbon in iron. In more oxidizing atmospheres, a scale will form, the removal of carbon oxides will be obstructed, and the rate of decarburization will be decreased radically. The depth of the decarburized layer depends on the length of time at temperature and the diffusion rate, which is primarily a function of temperature.

The structure of the decarburized layer depends on the temperature attained during heating. On heating to a temperature where the steel is austenitic at all carbon compositions, there will be a gradual decrease in carbon content towards the surface, with or without a zone of unorientated ferrite. If decarburized below the upper critical temperature, there will be free ferrite on the surface and a two-phase structure with no carbon gradient beneath the free ferrite. At temperatures where the steel is austenitic at only some carbon compositions, there will be free ferrite on the surface and a layer containing a carbon gradient below the layer of free ferrite. This is illustrated in Figure 1. If there is no carbon on the surface, there will be a gradient in carbon composition up to the composition where ferrite is in equilibrium with austenite (at the point (C_1, D_1) in Figure 1 (b)). The carbon composition then steps up to the composition of austenite in equilibrium with ferrite at that temperature (at (C_2, D_1)). This is followed by a gradient to the composition of carbon in the core of the sample (from C_2, D_1) to (C_3, D_2)). In oxidizing atmospheres, the formation of a scale may eliminate most of the free ferrite layer on the surface by the reaction of iron on the surface to form iron oxides.

After decarburization during annealing, normalizing, or austenitizing, cooling from temperature will produce various microstructures such as ferrite, pearlite, bainite, martensite, or tempered martensite in the core of the sample.

Andrew and Richardson (4) performed experiments to determine the extent of decarburization in various spring steels including plain carbon steel. They determined that heating in a furnace with an uncontrolled atmosphere resulted in a decarburized layer and scale on the

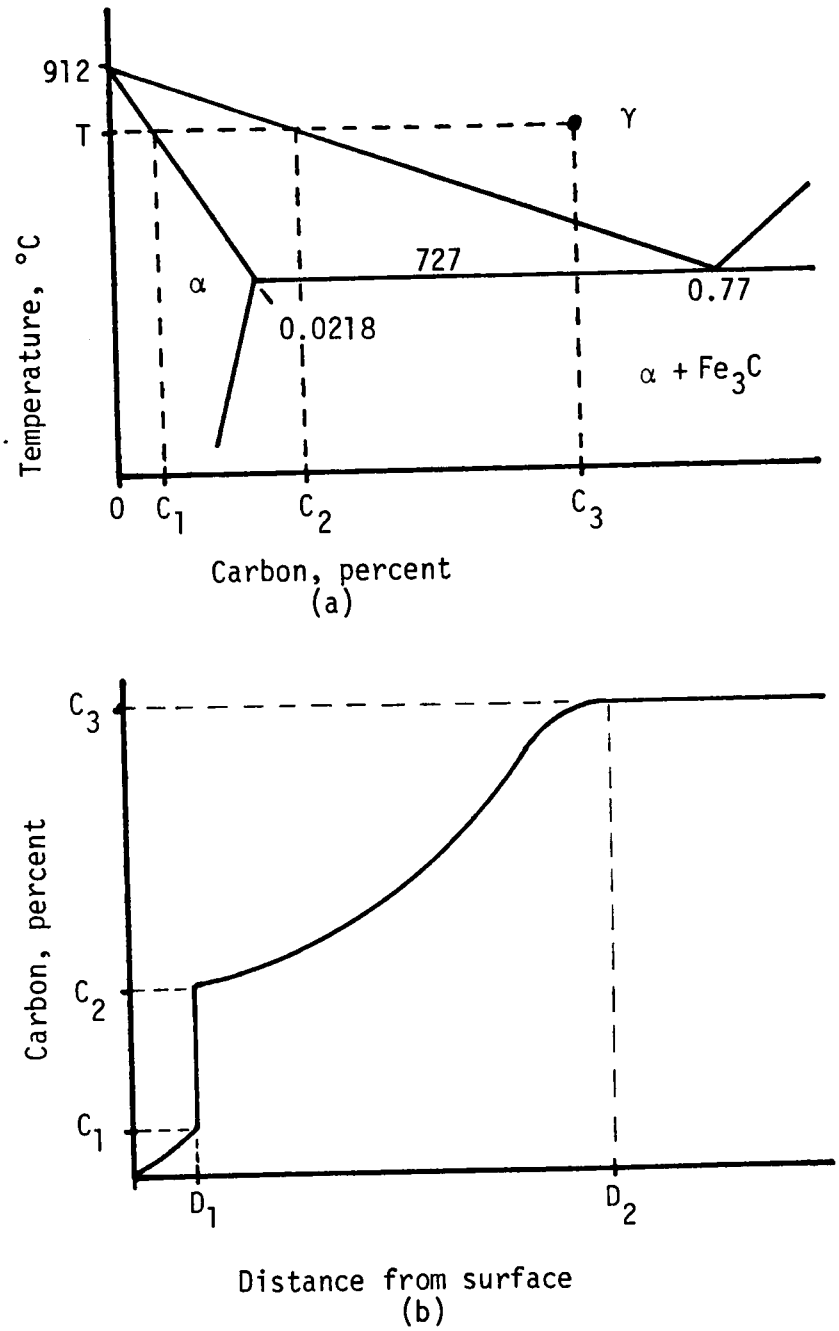

Figure 1. Distribution of carbon in a decarburized steel. (a) Schematic iron-iron carbide phase diagram. The temperature, T, is above the upper critical temperature (solid black line) for a steel with a carbon content, C_3. (b) Schematic diagram showing the carbon concentration as a function of distance from the surface as a result of diffusion.

surface. This can occur during the hot rolling process where the steel is heated as high as 1250°C (2282°F) prior to the first pass and then rolled, or during subsequent heat treatment.

Riddihough and DeBelin (12), using a hot rolled steel, as hot rolled, performed a detailed study to identify the presence of grain boundary oxides. Penetration of oxide into the grain boundaries occurred to a depth of about 0.001 inch (0.025 mm) for a 0.010 inch (0.25 mm) decarburized layer.

Fatigue Testing

Fatigue data for smooth specimens is usually presented as an S-N diagram, a plot of stress (S) versus the number of cycles to failure (N). The stress may be the maximum stress, the minimum stress, or the stress amplitude attained in the cycle. In addition, the mean stress, stress ratio or stress amplitude should be specified. The stress ratio (R) is the minimum stress in the cycle divided by the maximum stress in the cycle. Other terms are defined in Figure 2.

S-N plots may then be used to compare the performance of two materials, or may be used to predict the probability of failure at a given stress level or expected fatigue life. In either case, interpretation of the data depends on whether the test data were obtained under conditions of load control or deflection control.

For conditions of a constant load, the stress on the specimen increases as the crack propagates, as does the crack tip stress intensity factor. The result is an increasing crack propagation rate. Swanson (13) has examined this situation and suggests that for load controlled systems, the initiation stage of fatigue is responsible for most of the fatigue life of a specimen and that crack propagation is a small portion of the

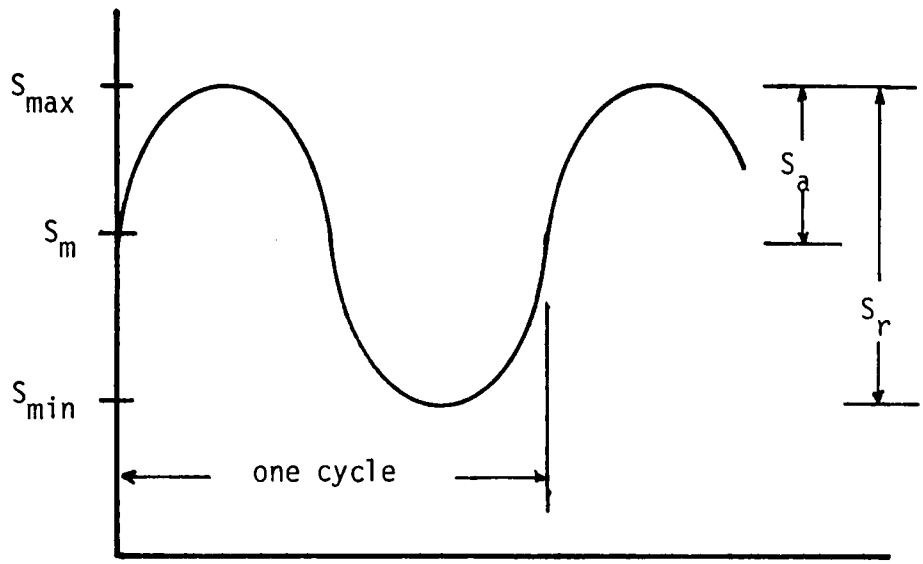

S_{max} = maximum stress

S_m = mean stress

S_{min} = minimum stress

S_a = stress amplitude

S_r = stress range

Figure 2. Stress-time schematic curve to define quantities used in describing fatigue behavior.

fatigue life. However, in a displacement controlled system, the range of motion at the end of the specimen is constant. When a crack develops, the specimen stiffness (or spring rate) decreases. With constant displacement, the applied load decreases and the resultant crack growth rate decreases. Swanson (13) states that in displacement controlled systems the propagation stage can be "quite the more predominant" stage in the fatigue life of the specimen.

Rozovsky, Weiss and Niedzwiedz (14) have examined in detail the problem of describing fatigue crack propagation in a displacement controlled system in bending. Using a model of a cantilever beam of rectangular cross-section containing a crack, they derived an expression for the load as a function of crack depth. As stated previously, the load decreases with increasing crack depth. But, the stress intensity factor at the crack tip increases with crack length, other things being equal (2, 15, 16). Rozovsky, et al. have derived an equation in which the stress intensity factor (and the resultant crack growth rate) initially increases with crack depth, and then decreases when the crack is nearly through the specimen. Crack growth rates, da/dN, were measured as a function of crack length, a, in a 0.61% carbon Si-Mn steel under constant deflection loading in bending. The equation

$$da/dN = C(\Delta K)^m \qquad (1)$$

was found to describe the crack propagation with the appropriate choice of constants C and m. ΔK is the range of the stress intensity factor defined as

$$\Delta K_i = S_r \sqrt{a_i \pi} \; f\left(\frac{a_i}{w}\right) \qquad (2)$$

a = crack length for a single-edge notched specimen

w = width of specimen

f = shape correction function for finite width specimens

i = a positive integer

Fatigue Processes

Dieter (16) has reviewed the basic structural changes that occur when a metal is subjected to cyclic stresses, as has Fine (2). Dieter describes the following sequence of events:

1. Crack initiation - includes the early development of fatigue damage which can be removed by a suitable thermal anneal. This stage culminates in the initiation of a microcrack.

2. Slip band crack growth - involves the deepening of an initial crack on planes of high shear stress. This is called Stage I crack growth.

3. Crack growth on planes of high tensile stress - involves growth of a well-defined crack in a direction normal to the maximum tensile stress. This is called Stage II crack growth.

4. Ultimate failure - occurs when the crack reaches sufficient load so that the remaining cross-section cannot support the applied load.

The first structural changes in fatigue become manifest as local plastic strains. Slip lines and slip bands are evidence of these strains in the grains. A slip line is the trace of a slip plane on a surface which was polished before straining. Plastic deformation has occurred on the slip plane by the movement of dislocations. A slip band is a group of closely spaced slip lines. Persistent slip bands are slip bands which are produced by fatigue cycling. They are called persistent

because they remain visible after electropolishing relatively large amounts of material from the surface of a fatigue specimen (2).

Kocanda (17) gives many examples of the development of slip bands and Stage I microcracking in persistent slip bands during fatigue cycling in Armco iron (0.02% carbon, commercially pure). Stage I cracks may propagate without any measurable macroscopic plastic deformation. Kocanda also shows examples of extrusions and intrusions of material on the surface near a microcrack in Armco iron.

Luther and Williams (18) have fatigue tested a normalized 0.08% carbon steel in axial loading to investigate fatigue crack initiation processes in steel. Previous investigators had assumed that grains at the surface would plastically deform prematurely because they were not supported on all sides by neighboring grains. Luther and Williams found that preferential strain hardening occurred at the outer surface of specimens cycled in fatigue, and that Stage I fatigue cracks formed in grains nearest the surface.

Klesnil and his co-workers (19) have shown that in carbon steel persistent slip bands form in ferrite grains but not in pearlite colonies. The ferrite grain boundaries impede the spread of these slip bands and play a controlling role in the first stage of the fatigue process. Klesnil, et al. have determined S-N curves for a 0.11% carbon steel. Tests were performed under axial loading with a constant load and a zero mean stress. The steel was heat treated to produce a ferrite-pearlite structure with varying ferrite grain sizes. A relation between the fatigue limit, σ_f, and the mean grain diameter, d (mm), was obtained:

$$\sigma_f = A + B\, d^{-1/2} \qquad (3)$$

$$\sigma_f = 155 + 5.11\ d^{-1/2}\ (MPa) \qquad (4)$$

Rahka (20) fatigue tested steels of 0.04 to 0.36% carbon in the annealed, cold worked, and quenched and tempered conditions to determine the size of the crack nucleus. The testing was done under axial loading with a stress ratio of 0.05 to 0.1 in the fatigue cycle. The crack nucleus was found to be a relatively flat region corresponding to a region of Stage I microcrack propagation on a crystallographic plane in a grain. Rahka related the tensile stress range, S_r to the crack nucleus size, a (mm), and found:

$$S_r = 6200\ (0.18\text{-}a)\quad (MPa) \qquad (5)$$

for all the steels and heat treatments tested. It was noted that this crack size may be tolerated indefinitely and that this size crack may be smaller than the critical crack size for Stage II propagation in smooth specimens. This critical crack size was expected to be dependent on the microstructure and loading environment.

Aita and Weertman (15) measured the Stage II crack growth rates in pearlitic steels as a function of stress intensity factor range, ΔK. The ability of the equation

$$da/dN = C(\Delta K)^m \qquad (6)$$

to describe crack propagation was again verified. It was also shown that for 0.23% carbon and 0.45% carbon steels, the crack growth rates for the low carbon steel were higher over the range of stress intensity factors tested. In general, the pearlite colonies acted as mechanical barriers to the growing crack.

In the detailed fractography performed by Aita and Weertman (15), it was determined that ductile fatigue striations formed in the ferrite only. These fatigue striations, an important fractographic feature associated with fatigue failure, are mutually parallel and equally spaced features appearing as lines on the fracture surface. The pearlite colonies did not contain fatigue striations. The pearlite fractured by two identified mechanisms, shear deformation of the pearlite when the platelets were perpendicular to the direction of crack growth, and void coalescence in the interlamellar ferrite when the platelets were about parallel to the direction of crack growth.

Masuda and his coworkers (21) reviewed the data correlating the fatigue crack growth rate and the striation spacing for steels. In their review, the crack growth rate coincided with the striation spacing for values of da/dN from 0.1 to 1.0 μ/cycles. Masuda, et al. experimentally determined the crack growth rate as a function of stress intensity factor and fatigue striation spacing. They used a quenched and tempered structural steel and stress ratios of R = 0 and R = 0.8 with center-cracked and compact tension specimens. They concluded that crack growth rates coincide with the fatigue striation spacing over a range of 0.1 μ/cycle to 70 μ/cycle.

Koterazawa, et al. (22) made detailed fractographic observations of rotating-bending fatigue specimens of an annealed carbon steel with 0.38% carbon and an aluminum alloy. They described features identified as fatigue striations and quasi-striations, and discussed mechanisms for their formation. Quasi-striations were patterns of jagged and unequally spaced lines on the fracture surface which had no correlation to the macroscopic crack growth rate. Quasi-striation patterns and rubbed areas

covered almost all of the fracture surface. The spacing of the fatigue striations was found to be roughly equal to the macroscopic crack growth rate. The observations were confirmed by Bales (1).

To summarize: the basic structural changes of fatigue are the same for a variety of alloys and loading conditions, although all stages are not always present. For instance, if there is a surface defect, the crack initiation and Stage I crack propagation stages may not be present; and Stage II propagation controls the fatigue life. The fatigue limit may depend on a critical stress for crack initiation (the formation of slip bands) and Stage I crack propagation, and/or a critical stress intensity factor for the propagation of fatigue cracks in Stage II.

Fatigue Behavior of Decarburized Steels

As previously noted, the fatigue behavior of decarburized steel was first studied in the 1930's (4, 5). Since that time, there have been many additional studies reported indicating that the effect of decarburization on subsequent performance is important to industry, but that its effects are still not completely understood. This section summarizes the work that has been reported.

In 1931, Hankins and Becker (5) examined the general problem of surface condition of quenched and tempered spring steels. They cite four factors of importance:

1. Surface irregularities of shape, such as small pits and scratches.
2. Surface cracks formed in heat treatment.
3. A defective layer on the surface of the metal such as that caused by decarburization.
4. The presence of residual stresses at or near the surface of the metal.

Hankins and Becker experimentally determined the fatigue limits of decarburized spring steels. The specimens were heat treated in a controlled atmosphere of CO_2 and CO which decarburized the metal, but did not produce much scale. The depth of decarburization was not reported. The specimens were tested in a rotating cantilever fatigue machine (constant load) with a zero mean stress. The decarburized specimens had a fatigue limit which was about half that expected from a quenched and tempered steel with a machined and polished surface.

Austin (23) performed fatigue tests on a 0.38% carbon steel in the decarburized and non-decarburized conditions. The decarburized specimens were heated to 700°C (1290°F) for eighteen hours in a wet hydrogen atmosphere. This produced a layer of free ferrite on the surface of the steel with a depth of decarburization of about 0.01 inch (0.25 mm). The specimens were then normalized and polished. Specimens that were not to be decarburized were machined to final size after normalizing and then polished. All specimens were tested in a rotating bending machine (constant load) with a zero mean stress. The fatigue limit at 10^7 cycles was decreased from 47 to 38 ksi (1000 pounds per square inch) (324 to 262 MPa), a decrease of 19% by decarburization.

Burns (24) performed a rotating cantilever (constant load) fatigue test on three silicon-mananese steels, two of 0.5%carbon, and one of 0.54% carbon, all in the quenched and tempered condition. In one group, the samples were machined and polished after heat treating. In the other group, the samples were machined and polished and then heat treated. This produced a surface which had a deep decarburized layer and a thin scale. The fatigue limit for the decarburized specimens was reduced by 17, 22, and 39% for the three steels tested. The greatest

reduction occurred for the highest strength steel which contained 0.51% carbon.

Gill and Goodacre in 1934 (6), examined the fatigue properties of decarburized steel wire which was used in wire rope. The wire was produced by cold drawing from wire which may have become decarburized during annealing before the final draw. The wires tested were of plain carbon steels of 0.36, 0.46, 0.55, and 0.79% carbon. A non-decarburized wire was produced for comparison by grinding off the surface of the stock before the final draw. Comparing the decarburized and non-decarburized specimens for wires drawn with 75% reduction in area, the reduction of the fatigue limit increased from 12 to 30% with increasing carbon content of the core material.

When comparing decarburized specimens with varying core compositions, Gill and Goodacre (6) found that the fatigue limits were about the same (that is, less than 10% difference). The decarburized surface of the steel wires obscured the effect of increasing the carbon content of the core material. They concluded that the fatigue properties of the decarburized steel wire were the properties of the surface layer.

Hankins, Becker, and Mills (25) determined that the combination of surface irregularities and decarburization are the major cause of the low fatigue resistance of unmachined steel plates. The experiments performed were rotating bending (constant load) fatigue tests on notched specimens to simulate the surface roughness of as-heat treated (quenched and tempered) spring steels. Tests were also done to determine the effect of the decarburized layer alone (i.e., not notched), in which case the fatigue limit was decreased by 50%. The addition of the notch decreased the fatigue limit even more. Decarburization was performed in

a container filled with strontium carbonate at 1000°C (1830°F), so that decarburization would occur without appreciable oxidation of the iron. The depth of decarburization was 0.02 inch (0.5 mm).

In 1947, Jackson and Pochapsky (26) reported on tests in rotating bending (at constant load) on decarburized and non-decarburized steels of grades SAE 2340, 4140, and 5140. Decarburization was done in a wet hydrogen atmosphere at 1040°C (1900°F). The specimens were quenched and tempered to two tensile strength levels, 140 ksi (965 MPa) and 250 ksi (1720 MPa), and then polished. The depth of decarburization was 0.05 inch (1.3 mm). The decarburized specimens had a lower fatigue strength and fatigue limit than the non-decarburized specimens. The fatigue limit was reduced by about 50% for the lower strength and 70% for the high strength levels for all three alloys. The results showed that the fatigue strength is determined by the strength (hardness) of the skin. The fatigue strength correlated directly with the strength of the ferrite which varied with alloy composition in the three grades of steel studied.

Garwood, Zurburg, and Erikson in 1951 (7) remarked on the considerable degradation in fatigue behavior of forged and heat treated axles due to even a small degree of decarburization. Using laboratory specimens, they determined a correlation between those specimens and results from testing full size components. The endurance limit of forged and heat treated (to Rockwell C 30) SAE 8650 axles containing an "excessive" amount of decarburization and scale was 26 ksi (179 MPa) (7). This is in comparison to a minimum fatigue limit of 38 ksi (262 MPa) for axles containing some "partial" decarburization and minimum scale (implied to be acceptable) which were shot peened after heat treating (7). Subsequent shot peening of the excessively decarburized axles increased the fatigue

limit from 26 to 30 ksi (179 MPa to 207 MPa). Thus, without peening, the fatigue limit was reduced 32% and subsequent peening of this material, although it improved the fatigue limit, still resulted in a decrease of 20% compared to the acceptable axles.

Lipsitt and Horne (27) tested SAE 1008 steel in the decarburized and non-decarburized conditions. The heat treatment consisted of 100 hours at 940°C (1725°F) and 100 hours at 700°C (1290°F) in a wet hydrogen atmosphere to produce a 0.003 to 0.005% carbon steel in which the entire cross-section was decarburized. One variable that was not controlled in the study was the ferrite grain size, which was ASTM 7 to 9 for the non-decarburized material and the ASTM 3 to 5 for the decarburized material. The S-N curves show a decrease in the fatigue strength and the fatigue limit for the specimens that were heat treated to decarburize the steel. This effect may be in part due to the larger grain size for the decarburized steel.

Robinson in 1957 (28) reported on fatigue tests of SAE 8660 leaf spring stock in the quenched and tempered condition. The testing was done under constant deflection loading in bending, with a minimum stress of zero. At a maximum initial stress of 150 ksi (1034 MPa) there was no significant difference in the fatigue life between the two types of specimens. But, at 100 ksi (690 MPa) the decarburized specimens did have a shorter fatigue life than those not decarburized. The tensile strength and yield strength were not reported.

In 1961, Simkovich and Loria (8) tested 0.042 inch (1.07 mm) thick sheet of 5% Cr-Mo-V steel heat treated to 210 ksi (1450 MPa) tensile strength in axial fatigue. The sheet specimens were decarburized to depths of 0.0005, 0.001, 0.002, and 0.003 inch (0.013, 0.025, 0.051, and 0.076 mm) at a temperature of 1010°C (1850°F). The fatigue specimens were lightly ground before testing. Oxidation at some of the grain boundaries was found. The S-N curves for each decarburization depth were plotted and show that an increased amount of decarburization decreased the fatigue limit by an increased percentage. The fatigue limits were decreased from 20 to 30% for these very small amounts of decarburization.

Spiegler, Weiss, and Taub (29) did fatigue tests on decarburized and non-decarburized 0.61% carbon steel with different microstructures. Decarburization was done in an air atmosphere furnace at 900°C (1650°F). S-N curves for each type of specimen were determined. For each microstructure, the fatigue strength and fatigue limit were decreased by decarburization. The reduction of the fatigue limit was 30% for a pearlitic microstructure, 40% for the tempered martensite, and 50% for the martensite. Also, four groups of pearlitic specimens were fatigue tested at a finite life with decarburized layers of 0.003 to 0.023 inch (0.08 to 0.58 mm) in depth. No difference could be found in the fatigue life at the same initial stress level with various depths of decarburization. The fatigue machine used was a constant displacement reversed bending machine. By careful observation of the growing crack, it was determined that crack propagation was a large portion of the fatigue life in the pearlitic and tempered martensitic structures.

Bron, Levites, and Pustovalov (30) did fatigue tests on a hot rolled 0.58% carbon steel in the quenched and tempered condition. The depth of decarburization was reported as 0.007 inch (0.18 mm) and the carbon content at the surface was 0.24%. The decarburized steel was compared to the same steel with the carbon restored to the surface layer. The steel was quenched and then tempered at temperatures of 250, 350, 450, and 550°C (482, 662, 842, and 932°F). In each case, the decarburized steel had a lower fatigue limit. For a tempering temperature of 250°C (480°F), the fatigue limit for the decarburized steel was about half that of the steel restored with carbon.

In 1976, there was still doubt as to the degree of degradation of fatigue properties caused by decarburization and the amount (depth and severity) of decarburization which was detrimental. Funke (31) tested four spring steels in torsion using reversed loading. (This is one of the few references available to indicate a difference in the fatigue behavior between torsional and bending loading). He developed S-N curves for steels with various degrees of decarburization and for non-decarburized steels. The carbon contents of the four steels which were used ranged from 0.55 to 0.65% carbon. The steels were quenched and tempered to a 220 to 230 ksi (1520 to 1590 MPa) tensile strength. The decarburized samples were heat treated to give a 25%, 50%, and 70% carbon loss at the surface compared to the carbon content of the core. These specimens were prepared by decarburizing to a 70% carbon loss, and then restoring the carbon to the surface to give a net loss of 25% or 50% at the surface. This procedure resulted in specimens with the same depth of decarburization, but with a different carbon concentration at the surface. The specimens were then quenched and tempered along with non-decarburized specimens and fatigue tested.

The results (31) showed that a carbon reduction of 25% did not reduce the fatigue limit as compared to non-decarburized specimens. Even a carbon loss at the surface of 50% led to only a slight (about 1%) impairment of the fatigue limit. But, with a 70% carbon loss, there was a 10% decrease in the fatigue limit.

In 1977, Bales (1) reported data for the fatigue strength of SAE 1042 steel with two different depths of decarburization. The specimens were decarburized in an air atmosphere furnace for periods of 8 and 24 hours to produce a total depth of decarburization of 0.038 and 0.080 inch (0.97 and 2.03 mm). Also a non-decarburized series of specimens was prepared and tested for comparison. All specimens were polished before testing and did not show intergranular oxidation remaining after the polish. The results showed that decarburization decreased the fatigue strength and the fatigue limit. The fatigue limit was decreased by 12% and 23% for depths of decarburization of 0.038 and 0.080 inch (0.97 and 2.03 mm) respectively.

The summarized results of the above work are shown in Table I. Most researchers determined the fatigue limits for a decarburized steel and for the same steel which did not have a decarburized layer. For brevity, only the percentage reduction of the fatigue limit for the decarburized steel is given in Table I.

The effect on fatigue properties of iron oxides at the grain boundaries has not, in general, been isolated from the effects of decarburization. Oxides at the grain boundaries may be assumed to be present in those cases (6, 24, 29, 30) where the specimens were heated in air, with the exception of Bales (1), who reported that no grain boundary oxides were present after the specimens were polished. Grain boundary oxides are expected to be absent in those cases (5, 7, 8, 23,

TABLE I

FINDINGS OF DECARBURIZATION RELATED FATIGUE TESTS

Ref.	Composition	Microstructure	Depth of Decarburization	Method of Decarburization	Type of Loading	Reduction of Fatigue Limit	Remarks
(5)	0.54% C, 1.95% Si 0.55% C, 0.27% V, 1.16% Cr	tempered martensite	NA	CO/CO_2 atmosphere at 900-950°C (1650-1740°F)	bending, constant load	54% 53%	
(23)	0.38% C	ferrite and pearlite	0.01 inch (0.25 mm)	wet H_2 atmosphere at 700°C (1290°F)	bending, constant load	19%	
(24)	0.54% C, 1.42% Si 0.51% C, 2.25% Si 0.51% C, 2.18% Si	tempered martensite	NA	air atmosphere at 900°C (1650°F)	bending, constant load	17% 39% 22%	
(6)	0.36% C 0.46% C 0.55% C 0.79% C	ferrite and pearlite, cold drawn	0.002 inch (0.05 mm)	air atmosphere at 1000°C (1830°F)	bending, constant deflection	18-24% 9-18% 26-28% 16-27%	The amount of cold work was 25%, 50%, 75%, 80%, 85%, and 90% reduction in area.
(25)	0.55% C, 1.16% Cr, 0.27% V 0.54% C, 1.95% Si	tempered martensite	0.02 inch (0.5 mm)	strontium carbonate pack at 1000°C (1830°F)	bending, constant load	50% 54%	
(26)	0.38% C, 3.48% Ni 0.40% C, 0.98% Cr, 0.18% Mo 0.38% C, 0.86% Cr	tempered martensite	0.05 inch (1.3 mm)	wet H_2 atmosphere at 1040°C (1900°F)	bending, constant load	47% and 71% 56% and 70% 55% and 77%	Two tempered temperatures were used, giving a medium and high strength steel, respectively.
(7)	0.40% C, 1.0% Cr, 0.2% Mo	tempered martensite	NA	wet H_2 atmosphere at 870°C (1600°F)	bending, constant load	40%	
(27)	0.09% C	ferrite and pearlite	NA	wet H_2 atmosphere at 940°C (1725°F)	bending, constant load	36%	
(28)	0.60% C, 0.55% Ni, 0.50% Cr, 0.20% Mo	tempered martensite	0.02 inch (0.5 mm)	NA	bending, constant deflection (S_{min} = 0)	NA	(28) compared fatigue lives at 150 ksi (1034 MPa) and 100 ksi (690 MPa)
(8)	0.35% C, 5.0% Cr, 1.35% Mo, 0.35% V	tempered martensite	0.0005 inch (0.013 mm) 0.001 inch (0.025 mm) 0.002 inch (0.051 mm) 0.003 inch (0.076 mm)	iron oxide and bone ash pack at 1010°C (1850°F)	axial (R=0.1), NA	19% 29% 30% 33%	
(29)	0.61% C, 1.86% Si	ferrite and pearlite tempered martensite martensite	0.025 inch (0.64 mm)	air atmosphere at 900°C (1650°F)	bending, constant deflection	30% 43% 52%	
(30)	0.58% C, 1.7% Si	tempered martensite	0.007 inch (0.18 mm)	hot rolled	bending, constant load	57% 42% 21% 32%	250°C (482°F) 350°C (662°F) 450°C (842°F) 500°C (932°F) } tempering temperatures
(31)	0.65% C, 1.65% Si 0.56% C, 0.79% Cr 0.55% C, 0.51% Cr 0.55% C, 1.08% Cr	tempered martensite	0.01 inch (0.25 mm)	NA	torsion, NA	No difference 1% 10%	25% 50% 75% } carbon loss compared to core composition
(1)	0.42% C	ferrite and pearlite	0.038 inch (0.97 mm) 0.080 inch (2.03 mm)	air atmosphere at 843°C (1550°F)	bending, constant load	12% 23%	

NA = Not available

Note: Specimens heated in air or the iron oxide/bone ash pack form iron oxides on the grain boundaries. Specimens heated in a wet hydrogen atmosphere or a strontium carbonate pack do not form grain boundary oxides. CO/CO_2 atmospheres may be adjusted to produce oxidizing or reducing atmospheres.

25, 26, 27) where the furnace atmosphere was controlled to produce no scale.

There is dispute in the available literature concerning the effect of increased depth of decarburization on the fatigue strength of specimens with finite lives (1). Two researchers (1, 8) reported data that showed a greater reduction of the fatigue strength for an increased depth of decarburization. However, one researcher (29) reported results that indicated that the fatigue life is not dependent on the depth of decarburization.

A review of the papers cited above indicates a trend in the extent of degradation in the fatigue limit of decarburized specimens with tensile strength. The high strength steels show a greater percent reduction of the fatigue limit than do the lower strength steels. The reduction of the fatigue limit of the decarburized steels generally decreased with increasing tempering temperatures for tempered martensitic microstructures (26, 30). The martensitic and tempered martensitic microstructures had a greater decrease of the fatigue limit for the decarburized specimens than did a steel heat treated to give a ferrite-pearlite microstructure (29). Also, for cold-worked ferrite and pearlite microstructures, those specimens which were cold worked to higher strength levels had a greater reduction of the fatigue limit for the decarburized specimens than those specimens which had a lower tensile strength (6).

There are some data available in the open literature that indicate that the fatigue strength and the fatigue limit depend mostly on the strength of the surface layer of the specimens (6, 26). One investigator (6) showed that a high carbon steel which was decarburized had about the same fatigue limit as a low carbon steel which was decarburized. Another

investigator (26) concluded that the value of the fatigue limit of decarburized specimens depends primarily of the strength of the ferrite, which varied with the alloy content of the steels used in the study.

Most of the above data are for specimens which were carbon free on the surface. There are two exceptions in the data summarized in Table I. One (30) had a 60% carbon loss (compared to the core composition) and reported a decrease of the fatigue limit for the decarburized specimens from 20% to 57% depending on the tensile strength of the steel. The other (31) reported that a carbon loss on the surface of 25% or 50% resulted in very little change in the fatigue limit, and that a carbon loss of 70% decreased the fatigue limit by about 10%.

It should be remembered that Funke (31) used torsional loading in contrast to bending loading used by all but one of the other investigators (8). A difference between the percentage reduction of the fatigue limit in bending and torsion is not expected. But if the results of Funke are attributed to the type of loading used (torsion), then there may be little reduction (less than about 10%) of the fatigue limit for the decarburized steels when tested in torsion, compared to the reduction in bending (roughly 15 to 50% from Table I). It is hoped that the present investigation will clarify the effect of torsional loading on the fatigue properties of decarburized steel.

Biaxial Fatigue

There are a number of fatigue failure criteria used to predict failure under multiaxial loading based on uniaxial data. The criteria described in the following discussion are the same as those for general yielding. The rationale for using these criteria for fatigue failure of

ductile metals is that failure in fatigue depends on whether or not plastic deformation is possible on a local scale.

Slip in grains is the process by which plastic deformation occurs on the local scale for most metals. Since slip is dependent on the resolved shear stress, it is expected that the equivalent stress to cause slip in an arbitrary stress state will depend on the shear components of the applied stress. The failure criteria discussed below are empirical formulations for an equivalent shear stress that causes slip. When this equivalent stress reaches a critical value, slip (yielding or fatigue failure) will initiate.

The failure criteria described in the following discussion are then primarily concerned with the crack initiation stage. The other fatigue processes are not accounted for. That is, the number of cycles in Stage I and Stage II crack propagation may not be predicted with the equivalent stress approach, although in application, the failure criteria are used to predict fatigue strength based on total fatigue life, consisting of both initiation and propagation stages. The principal justification for using the criteria will therefore be taken as empirical.

The following discussion is limited to isotropic ductile materials. In an isotropic material, or in a metal which, because of a sufficiently large number of randomly oriented grains may be considered to be isotropic, the orientation of the principal stresses in relation to the specimen axis is assumed to be of no consequence and only the magnitudes are considered. Furthermore, the effects of size and shape of the specimen are not considered at this time. This discussion will not involve the effects of superimposed static stresses (that is, only completely reversed loading will be discussed) or out-of-phase stresses.

The discussion will examine the fatigue strength at N cycles. If the combination of principal stresses is less than or equal to the critical stress stated in the criterion, failure will not occur in less than N cycles.

The symbols σ_x and τ_{xy} refer to the maximum value in the stress cycle of the bending (or normal) stress σ_x, and the torsion (or shear) stress, τ_{xy}. The transformations from a general biaxial stress state, σ_x, σ_y, and τ_{xy} to principal stresses are:

$$\sigma_1 = +\sqrt{\left(\frac{\sigma_x - \sigma_y}{2}\right)^2 + \tau_{xy}^2} + \frac{\sigma_x + \sigma_y}{2} \qquad (6)$$

$$\sigma_2 = 0 \qquad (7)$$

$$\sigma_3 = -\sqrt{\left(\frac{\sigma_x - \sigma_y}{2}\right)^2 + \tau_{xy}^2} \quad \frac{\sigma_x + \sigma_y}{2} \qquad (8)$$

where σ_1, σ_2, and σ_3 are the principal stresses.

The maximum shear stress criterion (also called Coulomb's, Guest's, or Tresca theory) (32) considers the shear stress having the greatest numerical value on planes in a cube of material whose axes are in the same direction as the principal axes (33).

So, if

$$\sigma_1 > \sigma_2 > \sigma_3 \qquad (9)$$

then for no failure

$$\frac{\sigma_1 - \sigma_3}{2} < \tau_c \qquad (10)$$

where τ_c is a critical shearing stress to cause failure as determined from a uniaxial or other suitable test. If σ_f is the failure stress in a uniaxial test, then

$$\sigma_1 - \sigma_3 = \sigma_f \qquad (11)$$

This criterion is represented in principal stress space for the biaxial case in Figure 3. In the first and fourth quadrants of the failure surface, the minimum and maximum principal stresses, respectively, are zero.

Another criterion used is called the octahedral shear stress criterion (34), maximum shear strain energy criterion (33), maximum distortion energy criterion (32), or variously the Huber, Hencky, or Von Mises theories (32). These are derived somewhat differently, but the algebraic form of the resultant failure criterion for an isotropic material is the same.

The derivation of the expression for octahedral shear stress consists of determining the shearing stress on the octahedral planes. An octahedral plane is any plane whose normal makes equal angles with the three principal axes. The octahedral shear stress criterion in effect averages the effect of shear stresses on many differently orientated slip planes (34).

The maximum shear strain energy criterion uses a critical value of the shear strain energy stored per unit volume to predict failure (33). The maximum distortion energy theory considers the total strain energy of the stresses material and subtracts the elastic strain energy corresponding to the volume change. This is because hydrostatic stresses

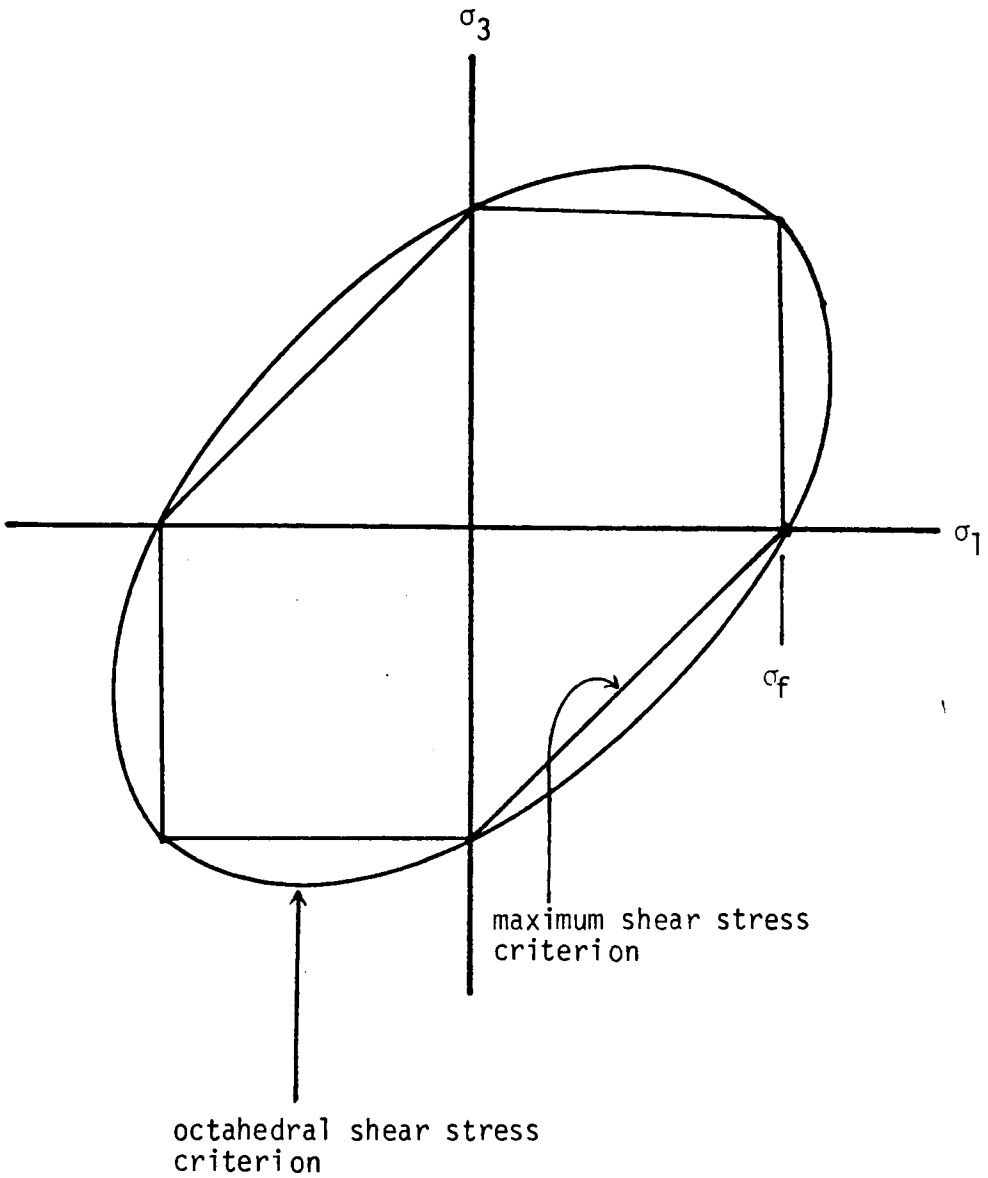

Figure 3. Failure envelopes in principal stress space.

only cause a uniform dilation or contraction. So, the portion of the strain energy that is considered is that portion which leads to a shape change of the element.

These derivations result in the equivalent statement for the octahedral shear stress, maximum distortion energy, and maximum shear strain energy criteria of:

$$\left\{ (\sigma_1 - \sigma_2)^2 + (\sigma_2 - \sigma_3)^2 + (\sigma_1 - \sigma_3)^2 \right\}^{1/2} < \text{(a constant)} \tag{12}$$

where the constant varies with the criterion used, or:

$$(\sigma_1 - \sigma_2)^2 + (\sigma_2 - \sigma_3)^2 + (\sigma_1 - \sigma_3)^2 < 2\sigma_f^2 \tag{13}$$

And for plane stress loading:

$$\sigma_1^2 - \sigma_3 \sigma_1 + \sigma_3^2 < \sigma_f^2 \tag{14}$$

where σ_1 and σ_3 are the non-zero principal stresses. This last expression is the equation of an ellipse as shown in Figure 3.

Gough and Pollard (35, 36) considered a modification of these empirical criteria in non-principal stress space. Using a second degree equation defining an ellipse, they defined a failure envelope using the absolute magnitude of the applied bending and torsion stresses and two experimentally determined constants for completely reversed loading:

$$\left(\frac{f}{f_o}\right)^2 + \left(\frac{q}{q_o}\right)^2 < 1 \tag{15}$$

f = applied bending stress

q = applied torsion stress

f_o = fatigue limit in bending

q_o = fatigue limit in torsion

The partial ellipse in the first quadrant is shown in Figure 4. This criterion was applied only to states of stress consisting of combined bending and torsion with zero mean stresses. The constants f_o and q_o are determined experimentally. If $f_o/q_o = 2$, then Gough's ellipse in the first quadrant is equivalent to the maximum shear stress criterion in the fourth quadrant of principal stress space. If $f_o/q_o = 1.73$, the first quadrant of Gough's ellipse is equivalent to the octahedral shear stress criterion in the fourth quadrant of principal stress space (33).

Gough and Pollard's (35, 36) experiments consisted of determining the fatigue limit at 10^7 cycles in combined bending and torsion. The bending and torsion stresses were in-phase and the machine used was of the constant load type. The tests were stopped when an increase in strain occurred in the specimen. The specimens did not fail by complete separation, but did contain a crack or cracks. Gough and Pollard tested five stress combinations of bending and torsion stresses. They used both solid and hollow specimens and a number of different steels. The results show that Gough's ellipse in its first quadrant is a good failure criteria for ductile metals. Both solid and hollow specimens were well represented in their biaxial fatigue behavior by the partial ellipse, although the magnitude of the fatigue limits changed. Pope (33) has reviewed Gough's data for eight different steels. The values of f_o/q_o reviewed by Pope range from 1.54 to 1.93 and average 1.68.

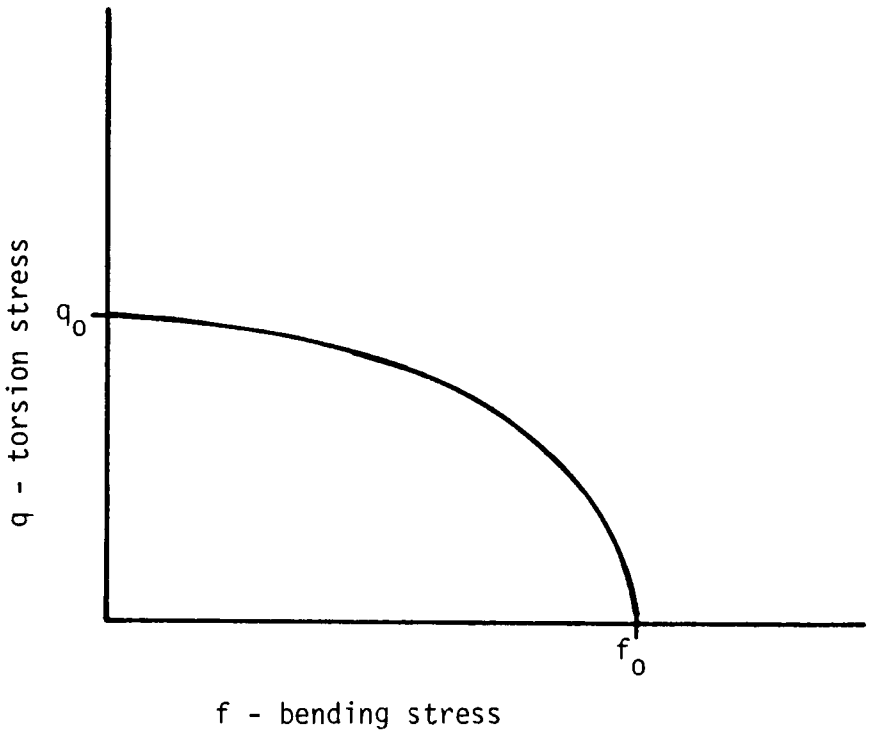

Figure 4. Schematic plot of Gough's ellipse in the first quadrant (35,36). q_o is the fatigue limit in torsion and f_o is the fatigue limit in bending.

This is in good agreement with the octahedral shear stress criterion for which $f_o/q_o = 1.73$. Frost, Marsh and Pook (37) have reviewed the fatigue data for a large number of ferrous and non-ferrous alloys for combined bending and torsion. The ratio f_o/q_o for the ductile alloys average 1.82. This average value is not far removed from that predicted by the octahedral shear stress criterion.

Sawert's data, as reviewed by Sines and Waisman (34), extends the available data to the first and fourth quadrants in principal stress space by using specimens of different shape. The data for steel agree "reasonably well" with the octahedral shear stress criterion (34).

Rotvel (39) ran a series of tests to determine the fatigue limit at 2.5×10^6 cycles using tubular specimens of low carbon steel. Completely reversed axial tension-compression cycling was combined with external and internal hydraulic pressure. The data obtained were used to compare to failure criteria in the first and fourth quadrants in principal stress space. The best fit of the data was to failure criteria containing two material constants, similar to Gough's ellipse (35, 36). The maximum shear stress and octahedral shear stress criteria were not in as good agreement with the data.

In 1977, Tanaka and Matsuoka (40) reported on combined stress fatigue tests on quenched and tempered steel using hollow and solid specimens and five combinations of axial and torsional loading. The machine used was electrohydraulic, and was operated at constant load with a mean stress equal to zero. The fatigue limit was determined at 2×10^6 cycles. In this study, the shape (hollow or solid) of the specimen did not influence the fatigue limit. The results indicate that the octahedral shear stress criterion gives the "better" agreement for this steel, compared to the maximum shear stress criterion (40).

In recent years, it has become common to report fatigue data on the basis of strain range instead of applied stress due to the availability of closed loop controlled tensile frames that can be operated under strain control. The values of total strain range ($\Delta\varepsilon$) are found from a cyclic stress-strain curve as illustrated in Figure 5 for a material loaded above the elastic limit. It has been found that the fatigue life data give excellent correlation with the total strain range when plotted on log-log coordinates. This method of analyzing fatigue life data has theoretical advantages because the short life fatigue data can be predicted using the plastic strain range ($\Delta\varepsilon_p$) and the long life data can be predicted using the elastic strain range ($\Delta\varepsilon_e$) (Figure 5).

Havard, Williams, and Topper (41) have compiled data on the biaxial fatigue of mild steels from nine investigators who used various test methods. These data were converted to a common form, either the total strain range, the plastic strain range, or the elastic strain range using available data for a cyclic stress-strain relation. The converted data were used in criteria of the form of Equations 10 and 12, except that strain values are substituted for stress. The resultant criteria are equivalent to Equations 10 and 12 for the elastic strain range (with zero mean strain) only. The criteria using total or plastic strain range are entirely empirical in nature.

At long life near the fatigue limit, the form which gave the "best agreement" was the elastic strain range (41). The fatigue data were compared using the maximum shear strain and octahedral strain criteria, and the latter gave the better correlation. At short life, plastic strain values were used to compare failure criteria. Neither the

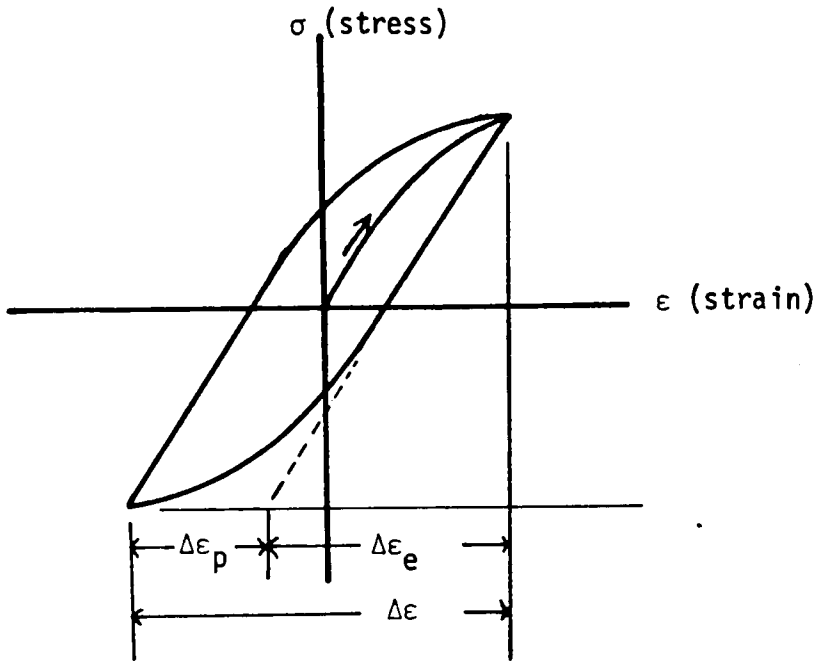

(a) Cyclic Stress-Strain Curve

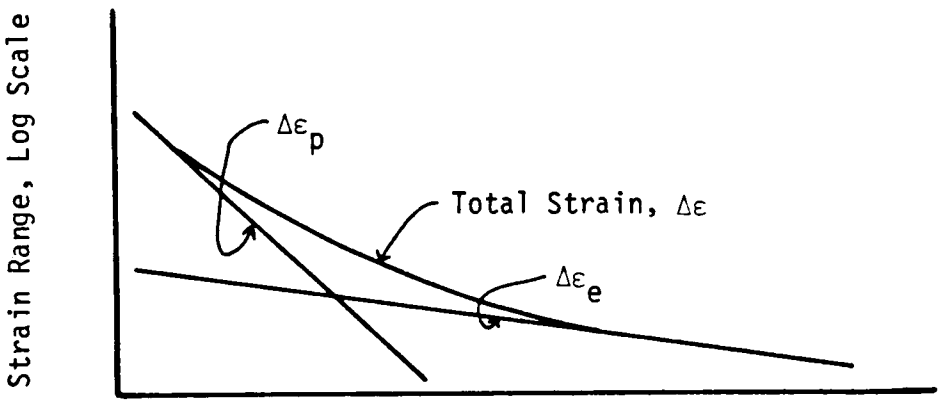

(b) Log Strain Range Versus Log Number of Cycles to Failure.

Figure 5. Parameters for fatigue analysis based on strain ranges. Adapted from Dieter (16).

maximum shear or octahedral shear strain criteria gave a better fit, but using the plastic strain values gave a better correlation than the total strain or elastic strain values.

In all of the biaxial fatigue experiments reviewed, only a few specimens were used to define the fatigue limits. The accuracy of finding the fatigue limits may not be great enough to distinguish between the failure criteria in a statistically significant manner. The maximum shear stress criterion is more conservative and the difference between the maximum shear stress criterion and the octahedral shear stress criterion for isotropic materials is not more than 15% (34).

Some investigators (38, 39, 40) define the fatigue limits at less than 10^7 cycles, and this may influence the magnitude of the fatigue limits found.

In general, the octahedral shear stress criteria is reported to give good correlation with the fatigue limit stress at 10^7 cycles in ductile materials (33, 37, 41). Criteria using both the bending fatigue limit and the torsion fatigue limit may give a better fit to the data (35, 36, 39), but require more testing. At stress levels above the yield point, criteria based on plastic strain range are reported to give better correlation (41) with experimental data than are criteria based on stress or elastic strain range.

CHAPTER II

EXPERIMENTAL PROCEDURE

Material

The material used for this research was purchased from a local supplier as Grade 1042, 1/2 inch (12.7 mm) cold drawn round bar stock. The nominal composition taken from the American Society for Testing and Materials (ASTM) standard A29-76 (42) is given in Table II.

Fatigue Specimen Preparation

The specimens were prepared as follows. First, they were normalized, machined in the gauge section, normalized again, machined on the grips, and finally polished. Normalizing consists of heating the steel into the austenite region, and then allowing it to cool in air. The decarburized fatigue specimens were allowed to remain in the furnace in an air atmosphere for a sufficiently long time to cause decarburization. The procedure is explained in detail below.

The barstock was initially cut into lengths slightly greater than 4 1/4 inch (108 mm). Eighty of these lengths were placed into a boat, covered with cast iron chips, granulated charcoal, and a lid. The boat was placed into the furnace for the first normalizing, a heat treatment of 870°C ± 14°C (1600± 25°F) for two hours. The boat was removed and it, with the samples, was allowed to air cool.

The first machining operation was to size the 1/2 inch (12.7 mm) round bar to 4 1/4 inch (108 mm) length and put centers in both ends. Then the hourglass-shaped gauge section was cut, using a rounded-tip

TABLE II

NOMINAL CHEMICAL COMPOSITION OF GRADE 1042 STEEL BAR

Carbon	Manganese	Phosphorus	Sulphur
0.40-0.47	0.60-0.90	0.040 max.	0.050 max.

(all values are weight percent)

cutting tool to avoid making grooves in the surface. The gauge section was circular in cross section with a minimum specimen radius of 0.255-0.257 inch (6.48-6.53 mm) for the non-decarburized specimens or 0.265-0.267 inch (6.73-6.78 mm) for the decarburized specimens as in Figure 6. The decarburized specimens became smaller because of oxidation during heat treatment.

The second heat treatment was of two types, one for the non-decarburized specimens (designated as the D1 heat treatment) and one for the decarburized specimens, (D8). For both heat treatments, the samples were degreased and then placed vertically in a piece of fire-brick with twenty holes spaced on 2 inch (51 mm) centers. For the D1 heat treatment, the samples were placed in a furnace stabilized at 843°C ± 14°C (1550 ± 25°F) for a period of one hour. For the D8 heat treatment, the samples were placed in a furnace stabilized at 843°C ± 14°C (1550 ± 25°F) for a period of eight hours. In both cases, the samples and the sample holder were removed from the furnace and allowed to air cool.

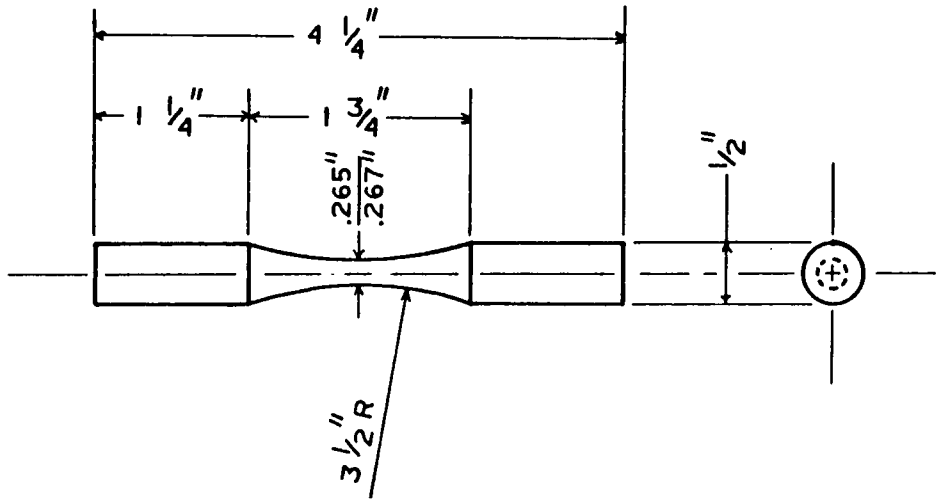

(a) For the Decarburized Specimens

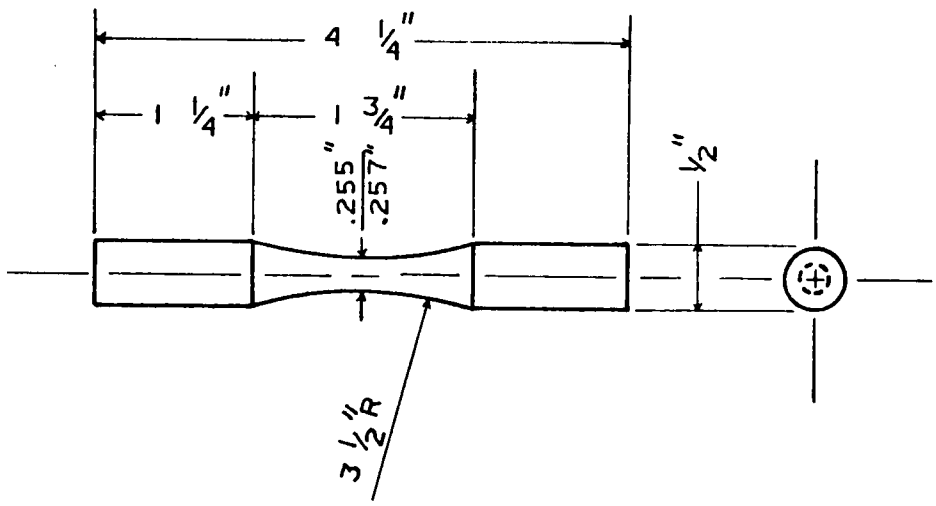

(b) For the Non-Decarburized Specimens

Figure 6. Specimen geometry before heat treatment.

The specimens were polished after the heat treatment to produce a surface of uniform roughness with a minimum of cold-work. It was necessary to produce specimens with minimum diameters which were ± .001 inch (0.025 mm) from a mean in order to assure an accurate fatigue machine calibration for all the specimens.

The heavy scale was removed by tapping the specimens with a length of 1/2 inch (12.7 mm) round bar. The remaining scale was removed with a wire brush. The thickness of the scale was about 0.007 inch (0.18 mm) for the D8 heat treatment and 0.001 inch (0.025 mm) for the D1 heat treatment.

The specimens were machined to a diameter of 0.347-0.348 inch (8.81-8.84 mm) in the sections that were to fit in the specimen holders on the fatigue machine.

The as-heat-treated specimens had a very rough surface. This was smoothed with 120 grit abrasive cloth. The polishing was done with the specimen mounted in the chuck of a drill press and rotated at a speed less than 500 rotations per minute (rpm). The speed was chosen to be slow enough so that the specimens did not heat up appreciably. After this and every other polishing step, the specimens were cleaned with solvent to remove the larger size grit. The specimens were next polished with grade 1 emery paper on the drill press at 1100 rpm. All the specimens had at least 0.001 inch (0.025 mm) removed from the surface. Polishing was stopped when visible pits were gone, visible grooves from 120 grit were gone, and the specimen was in an acceptable size range. The size was measured using a ball micrometer. Subsequent polishing did not remove more than 0.001 inch (0.025 mm) from the diameter. The measurement of the diameter was done at this stage of polishing because if done at a later state, it may leave a burnished or plastically deformed

surface. The final sizes were 0.253 ± 0.001 inch (6.43 ± 0.025 mm) for the decarburized specimens and 0.2485 ± 0.001 inch (6.31 ± 0.025 mm) for the non-decarburized specimens.

The samples were polished by hand in a longitudinal direction with grade 0 emery paper until scratches from grade 1 emery were gone. Then the samples with the 2/0 emery paper until grade 0 emery scratches were not visible. After cleaning, they were coated with oil and stored in a dessicator.

Just prior to use, the specimens were degreased and polished with 3/0 emery paper longitudinally by hand until no circumferential scratches were visible to the naked eye. The specimens were cleaned with solvent and coated with a very light coat of oil again. This last coat of oil was thin enough so that it did not seep into a crack when a crack formed. It was used to prevent rusting of the specimen surface during the test which could last from a half hour to days.

Operation of the Fatigue Machine

The fatigue machine used was a constant deflection type model VSP-150 fatigue testing machine with the combined stress attachment produced by Fatigue Dynamics, Incorporated. This machine consists of a flat test bed, variable speed electric motor, the motor speed control, counter, automatic motor cut-off, and a variable eccentric. On the flat test bed is an adjustable swivel vise in which the specimen is held in cantilever fashion. The other end of the specimen is held in the specimen clamp. This specimen clamp also swivels on the same axis as the vise. The specimen clamp is attached to the loading arm which is driven in an up-and-down motion by the crank. The crank is attached to the variable eccentric. The variable eccentric is marked off as to the range of

displacement of the crank in the vertical direction. The range of displacement is the maximum height of the crank minus the minimum height, and does not change during the fatigue test. The fatigue machine is illustrated in Figure 7.

The fatigue machine was calibrated by hanging weights from the end of the loading arm when it was detached from the crank. The deflection at the point of loading was measured with a dial gauge. Using the load at the end of the loading arm, the maximum stresses on the surface of the specimen at the minimum specimen cross section can be calculated. These stresses are then related to the deflection, which is used to set the range of displacement at the variable eccentric.

The stresses are calculated using the elastic bending formula and the elastic torsion formula:

$$\sigma_x = \frac{MC}{I} \tag{16}$$

$$\tau_{xy} = \frac{TC}{J} \tag{17}$$

σ_x = bending stress

τ_{xy} = torsion stress

C = critical dimension, the radius of specimen at the minimum cross section

M = bending moment

T = torque

I = area moment of inertia of the cross section area

J = polar moment of inertia of the cross section area

The critical dimension required to calculate the stresses on the specimen are defined in Figure 8. The view in Figure 8 represents the top view of the fatigue machine as seen in Figure 7. The stresses that are calculated for the calibration curve are:

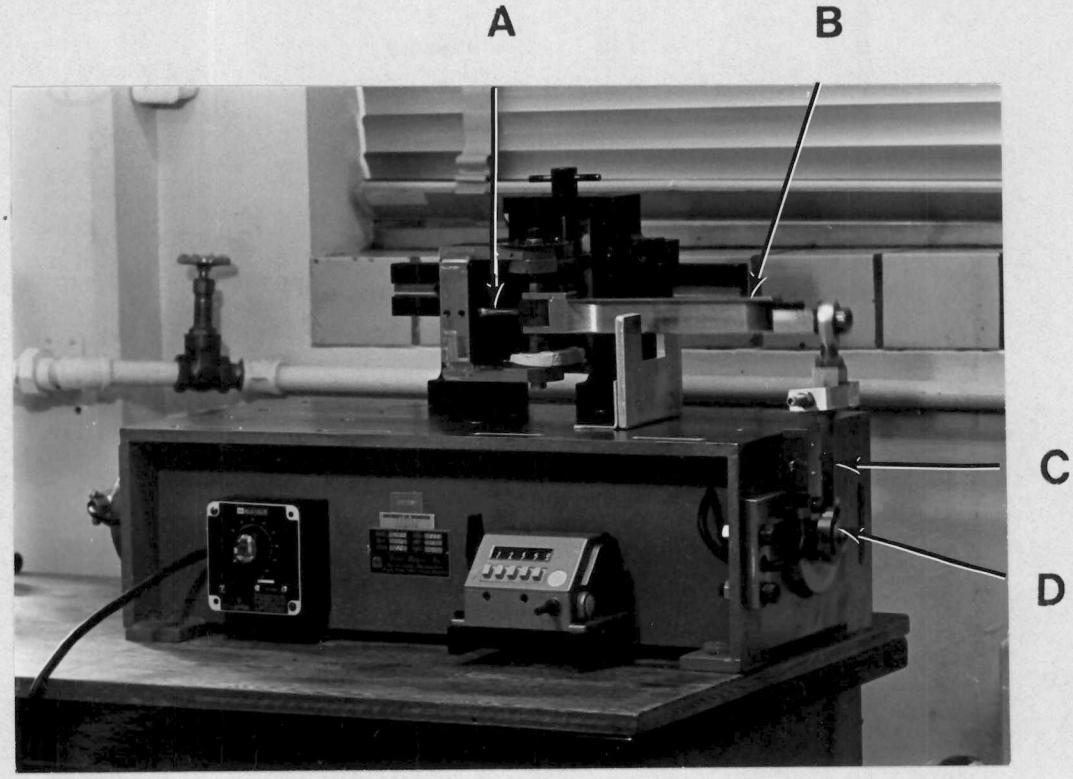

Figure 7. Fatigue machine. "A" is the specimen, "B" is the loading arm, "C" is the crank, and "D" is the variable eccentric.

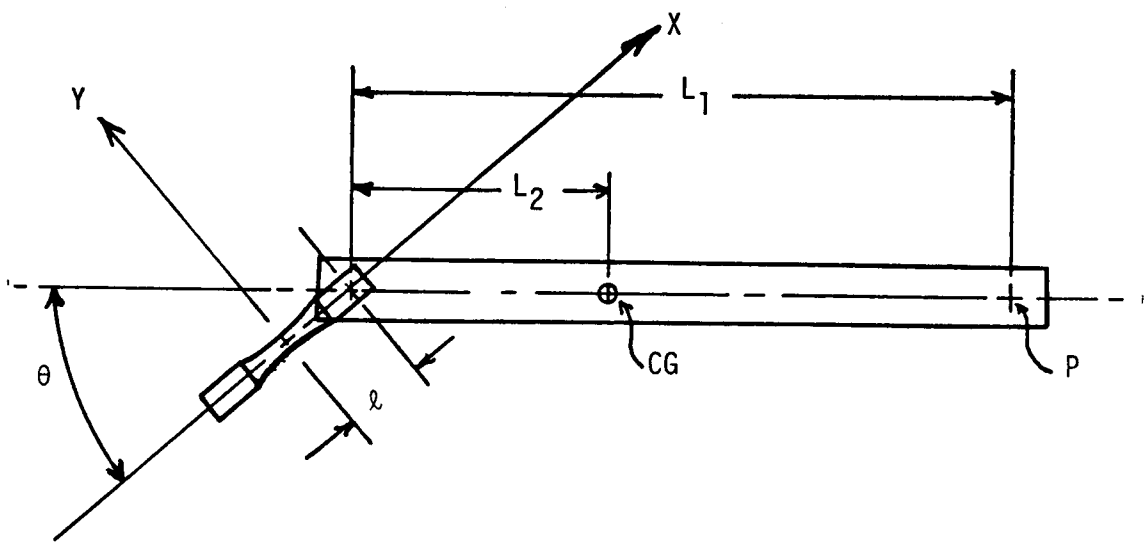

X = Axis parallel to specimen centerline.

Y = Axis perpendicular to specimen axis.

P = Applied load. The direction is perpendicular to the plane of the paper.

CG = Center of gravity of the loading arm.

L_1 = Distance from pivot point to the applied load.

L_2 = Distance from the pivot point to the center of gravity.

ℓ = Distance from the pivot point to the mid-section of the specimen.

θ = Angle between the specimen axis and the loading arm. This angle is variable.

Figure 8. Critical dimensions on the fatigue machine.

$$\sigma_x = \frac{M\,C}{I} = \frac{[\,P(L_1\cos\theta + \ell) + w_B(L_2\cos\theta + \ell)\,]\,r}{\frac{\pi r^4}{4}} \qquad (18)$$

$$\tau_{xy} = \frac{T\,C}{J} = \frac{(\,P\,L_1\sin\theta + w_B\,L_2\sin\theta)\,r}{\frac{\pi r^4}{2}} \qquad (19)$$

where

w_B = weight of the loading arm = 2.14 ± 0.02 lbs.
(9.52 ± 0.09 Newtons)

ℓ = 1.5 ± 0.1 inch (38 ± 2.5 mm)

L_1 = 11.81 ± 0.02 inch (300 ± 0.5 mm)

L_2 = 4.5 ± 0.025 inch (114 ± 1 mm)

θ = 0 or 98° ± 0.1° (bending or torsion)

r = specimen cross sectional radius at mid-section
= 0.12425 ± 0.0005 inch (3.156 ± 0.013 mm)
0.1265 ± 0.0005 inch (3.213 ± 0.013 mm)

The errors of the calibration are mostly due to specimen-to-specimen variations in the radius of the cross section, variations in machine alignment, and variations in specimen mounting. These errors are estimated to be ± 2.5 ksi (± 17.2 MPa) in bending and ± 1.0 ksi (± 6.9 MPa) in torsion.

It was assumed that the applied load was zero when the range of displacement on the fatigue machine was set to zero. With this assumption, the calibration curves giving σ_x or τ_{xy} as a function of the range of displacement at the variable eccentric were calculated.

The frequency of the fatigue test varied from 10-25 Hz. This was necessary because one must find a frequency, by trial and error, where the loading arm moves in a vertical direction. Otherwise, stress

components other than those accounted for may be created. The upper frequency is limited by the excessive vibration created in the machine. The waveform of the stress function is approximately sinusoidal.

To reiterate, the stress is calculated based on elastic theory, without considering plastic deformation, dynamic loads, or the presence of a notch. When a crack does form, the applied load is reduced due to loss of specimen stiffness. Failure was defined as complete separation of the test specimen.

Fatigue Data Presentation

The fatigue data are given in Appendix D. These data are presented in S-N diagrams, with normal or shear stress on the ordinate and the logarithm to the base ten of the number of cycles to failure on the absicca. A smooth curve is drawn through the data points of each set. This curve is fitted to the form

$$\sigma_x \text{ or } \tau_{xy} = Ax^3 + Bx^2 + Cx + D \qquad (20)$$

where A, B, C, D, are experimentally determined coefficients, $x = \log_{10} N_f$ and N_f = number of cycles to failure.

The coefficients are determined by applying a method of multiple regression analysis to determine which set of coefficients best fit the data. The method is to minimize the sum of the squares of the deviations between the actual and predicted values. The method is explained in detail in Snedecor (43). The method was implimented by using a statistical package program "STATPACK" (44), which is in storage at the University of Tennessee Computer Center at this time (1981). The fitted curve represents the median fatigue strength of the data points obtained.

All of the data points were used to determine the calculated curve. The specimens that did not fail were plotted at 10^7 cycles at the stress level at which they were tested. The fatigue strengths at any value $\log_{10} N_f$ are determined from the fitted equation. The fatigue limit is determined by calculating the value of the stress at 10^7 cycles using the fitted equation. The fatigue limit is thusly defined as the median fatigue strength at 10^7 cycles for the present study. The error of the fatigue limit determined by this method was established by calculating the upper and lower bounds for possible values of the median fatigue strength at 10^7 cycles. The upper bound is the stress level at which specimens failed and the lower bound is the stress level at which specimens did not fail in 10^7 cycles. This range of values was determined to be about $\pm$ 8% of the calculated fatigue limits. The error of the fatigue limit may then be taken as about $\pm$ 8%.

Surface Roughness Tests

Surface roughness tests were also made on one quarter of the specimens, after the specimens failed. This was done to document the specimen preparation procedure and to determine if there was a significant variance in the specimen preparation procedure. The value of surface roughness determined is the arithmetic average surface roughness value (AA). This is defined by American National Standards Institute standard B 46.1 - 1978 (45) as

$$AA = \frac{1}{L}\int_{x=0}^{x=L} |y|\, dx \qquad (21)$$

where

x = distance along the surface

y = height of the surface above or below the centerline

L = traversed length

The arithmetic average surface roughness is the average height of the surface profile above and below the centerline. The centerline is defined where the areas A + B + C + D = F + G + H + I in Figure 9.

The surface roughness tests were made using a Talysurf "4" surface roughness gauge made by Rand Precision Industries, Ltd. This device consists of a stylus which traverses over the surface, and a shoe which determines the average height of the surface. In this case, a shoe giving a curved traverse with radius 3 1/2 inch (89 mm) was used. This corresponds to the radius of the gauge section of the specimen. The stylus was moved in a direction parallel to the specimen axis.

The stylus is connected to an inductive transducer. This sends an electrical signal to a device which converts this to a surface roughness reading on the meter. The assigned value was taken as an average of three readings from each specimen.

Microhardness Tests

Microhardness tests to determine the depth of decarburization were performed using a Kentron microhardness tester manufactured by Riehle Testing Machines. A 200 gram load was used with the 136° diamond pyramid indentor. This gives hardness expressed in Vickers Hardness numbers (HV) or Diamond Pyramid Hardness Numbers (DPH). These numbers were converted to Rockwell B hardness using the conversion scale for steels in ASTM standard E 140-78 (46). The calibration of the hardness machine was verified to

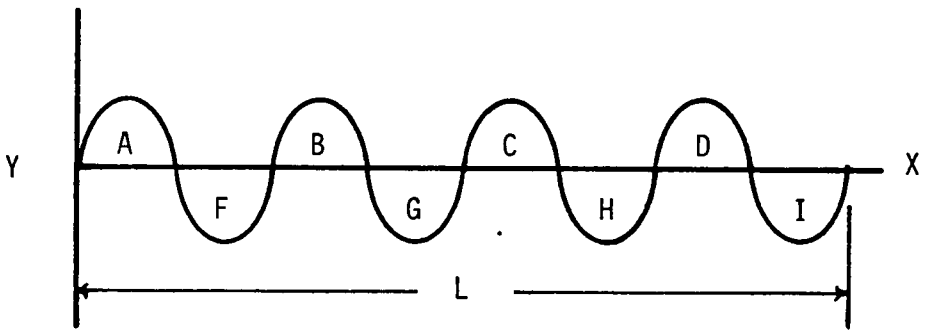

$$AA = \frac{1}{L} \int_{x=0}^{x=L} |y| \, dx$$

Figure 9. Surface roughness. The centerline is defined when the areas A + B + C + D = F + G + H + I. The arithmetic average surface roughness, AA, is the average height above and below the centerline.

give a hardness reading which was within ± 4% of the hardness of a test block. Hardness tests were done on polished unetched fatigue specimens which were sectioned on a transverse plane at the minimum diameter of the specimen. The individual indentations were spaced at intervals of 0.003 inch (0.09 mm) starting from 0.002 inches below the surface and progressing from the surface at intervals of 0.005 inch (0.13 mm) to the center of the specimen. Twelve specimens, or 15% of the total were used to determine hardness curves.

Curves were fitted to the data using the STATPACK program. The fitted curve was of the form

$$HV = C\,x + D \tag{21}$$

for the D1 heat treatment, the non-decarburized samples, and

$$HV = E\,x^4 + F\,x^3 + G\,x^2 + H\,x + I \tag{22}$$

for the D8 heat treatment, the decarburized samples. C, D, E, F, G, H, and I are fitted coefficients and x is the distance from the surface of the sample. The intersection of these two fitted curves is taken as the total depth of decarburization. The microhardness data is given in Appendix C.

The hardness of the non-decarburized specimens showed a definite hardness difference from surface to center, but the variation did not appear to be concentrated at the surface. Consequently, a linear variation was assumed. The hardness of the decarburized specimens was very low at the surface of the specimens and increased towards the center a higher order equation was necessary to minimize the standard deviation of regression.

Tensile Tests

Three tensile specimens of each heat treatment, D1 and D8, were prepared. The specimens were machined as in Figure 10 and heat treated with the same procedure as the fatigue specimens, except that the tensile specimens had to be placed horizontally in the furnace because they were too long to be placed vertically. The tensile specimens had a diameter of 0.35 inch (8.9 mm) and a gauge length of 1.4 inch (35.6 mm). This gives a gauge length to diameter ratio of four, as specified by ASTM standard E8-78 (47).

Scale removal and polishing steps were the same as for the fatigue specimens except that polishing stopped after grade 1 emery paper. Polishing was done so that the size of the specimen at the mid-point of the gauge length was a few thousands of an inch less than near the grip section.

Tensile tests were performed in compliance with ASTM standard E8-78 (47). A strip-chart record of the load and elongation was made.

Metallography and Fractography

Optical microscopy (OM) and scanning electron microscopy (SEM) were performed on metallographically prepared samples from the fatigue specimens. Fracture surfaces of the broken fatigue specimens were examined macroscopically and microscopically using the SEM. These samples were viewed to determine if any further contributions could be made to the understanding of fatigue processes in decarburized steels, and to identify any differences between bending and torsion specimens.

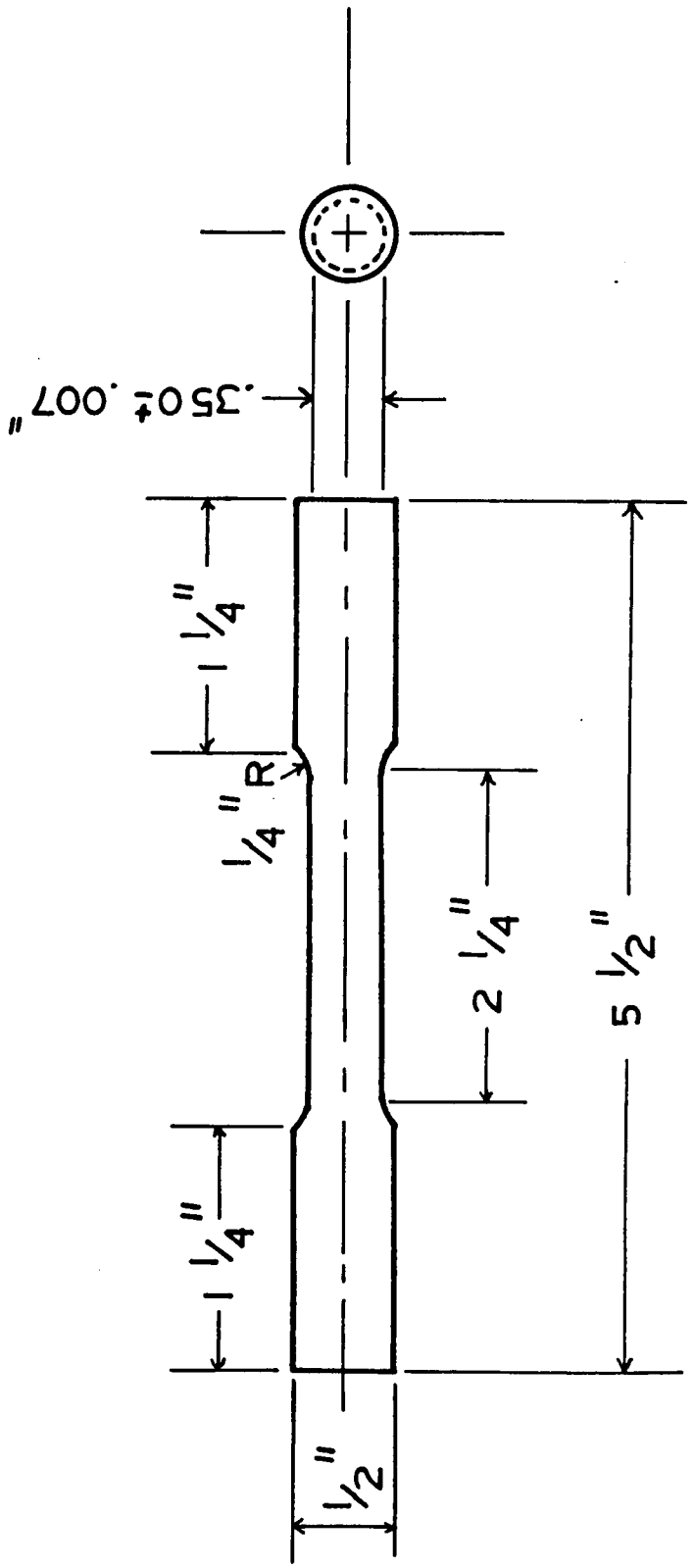

Figure 10. Tensile specimen before heat treatment.

Metallographic samples were prepared using standard laboratory procedures. The fatigue specimens were sectioned with an abrasive cut-off wheel in either the longitudinal or transverse planes. The samples were mounted in Lucite plastic. Grinding stages were: 120 grit used with water, and grades 1, 0, and 2/0 dry emory papers. The last grinding stage, 3/0 emerypaper, was used with kerosene. Polishing was done with 9-micron diamond paste on nylon cloth and 1-micron diamond paste on selvyt cloth. This was adequate for general observations. For samples which were observed at high magnifications and with a light etch, a final polish with 0.06 micron alumina on Microcloth was used. The etching reagent used was 2% by volume nitric acid in 98% methanol, which was swabbed on the specimen.

The grain size was determined using photomicrographs of the metallographically prepared specimens and the planimetric procedure outlined in ASTM E112-77 (48). The pearlite colonies which were completely surrounded by ferrite were counted as representing the prior austenite grains.

Metallographic samples for the SEM were prepared as above and then gold coated with a sputter coating device. The thickness of the gold coat was approximately 0.05μ.

Fractographic samples were sectioned from the fatigue specimens and mounted on stools. The samples were cleaned ultrasonically in methanol for five minutes and gold coated as above. In this case, the gold coating was used to improve resolution by providing a conductive surface over the sample, including any debris, rust, or film on the sample. Resolution on the fractographic samples is estimated to be not better than 0.1μ at 5000x. The scanning electron microscope used was the model 900 made by AMRAY, Inc.

With a resolution of 0.1μ, any features such as pearlite platelets or fatigue striations, which may have spacings less than 0.1μ, could not be distinguished.

CHAPTER III

RESULTS AND DISCUSSION

A series of tests were run on the decarburized and non-decarburized steels to characterize the material and specimen preparation procedures. The main objective here was to eliminate all variables between the two types of specimens except those that were due to the loss of carbon at the surface. Testing included tensile tests, surface roughness tests, an examination of the microstructure, determination of grain size, and a microhardness traverse through the layer depleted of carbon.

Results of the Characterization Tests

Surface roughness tests. The surface roughness measurements are given in Appendix A and summarized in Table III. The surface produced is shown in Figure 11. The arithmetic average values of the surface roughness are 3.0 and 3.9 μ-in. (0.076 and 0.99μ) for the non-decarburized and decarburized fatigue specimens, respectively. This slight difference is thought to be due to the fact that the decarburized steel is softer at the surface, so that the scratches produced are deeper.

There are little data available in the open literature to indicate quantitatively the amount of degradation in fatigue properties due to differences in surface roughness. The greatest effect occurs at stress levels near the fatigue limit.

There seems to be a critical roughness below which further polishing has no beneficial effect. This critical roughness value has been found (49) to decrease with increasing tensile strength. Siebel and Gaier (49) state that for annealed steels there is no difference (i.e., less than

TABLE III

PROPERTIES OF THE FATIGUE SPECIMENS

	Non-Decarburized	Decarburized
Surface Roughness, $\bar{x} \pm s$, μ-in.(μ)	3.0 ± 0.9 (0.076 ± 0.023)	3.9 ± 1.6 (0.099 ± 0.041)
Austenite Grain Size, ASTM Grain Size Number,	8	8
Mean Grain Diameter μ-in.(μ)	870(22)	870(22)

$\bar{x}$ = sample average
s = standard deviation of the estimate

Figure 11. Surface of a specimen which was produced by polishing longitudinally with grade 3/0 emery paper. SEM 180x.

10%) in the fatigue limit at 10^6 cycles for steels with a maximum depth of groove less than 160 to 240 μ-in. (4 to 6 μ). The maximum groove depth measured by Siebel and Gaier is equivalent to two to four times the arithmetic average surface roughness.

The tensile strength of the specimens used in the present study is in the range of values for annealed steel. Considering Siebel and Gaier's most conservative value, no difference in fatigue properties is expected for specimens with arithmetic average surface roughness values less than about 20 μ-in. (0.5 μ). All of the present values are in the range of 2 to 6 μ-in. (0.05 to 0.15 μ), so surface roughness is not expected to be a variable in the present study.

Microstructure. The microstructures of the decarburized and non-decarburized specimens at the core are presented in Figures 12 and 13. The prior austenite grain size is ASTM number 8 for both materials, which corresponds to a mean grain diameter of 870 μ-in. (22μ) (48). These data indicate that there is no significant grain growth in eight hours at 843°C (1550°F) and that the grain size of the core is not a variable in the present study. The structure is ferrite and pearlite with uniformly distributed pearlite colonies, and the prior austenite grains are equiaxed.

The relative amounts of ferrite and pearlite in the microstructures were determined by using a manual point count. A manual point count consists of counting the number of points contained in grains of ferrite or pearlite on the micrographs using a grid of lines superimposed on the micrograph. In this case, the number of points counted was 4000 using six micrographs each of the decarburized and non-decarburized steels. The manual point counts gave relative amounts of 33% ferrite and 66% pearlite.

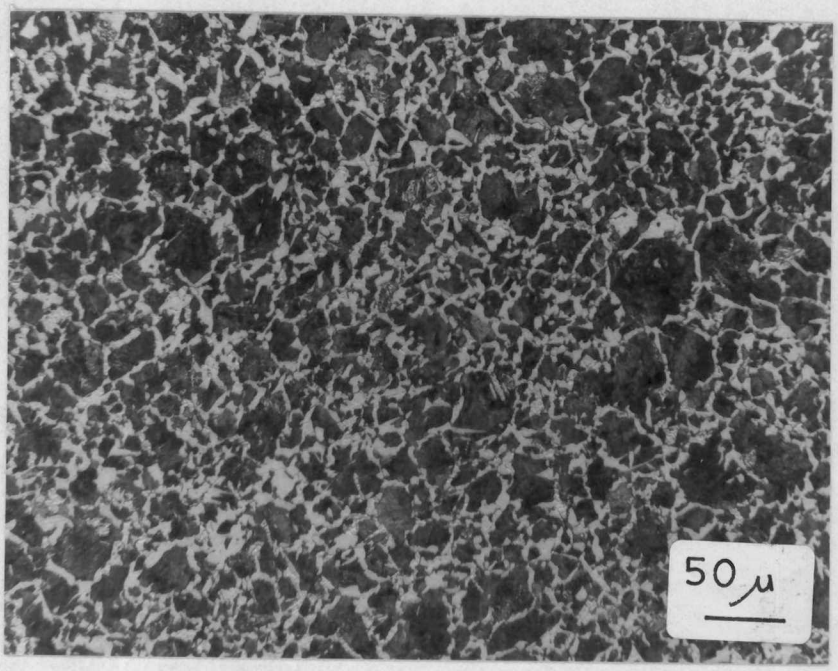

Figure 12. Core microstructure of decarburized specimens. OM 200x.

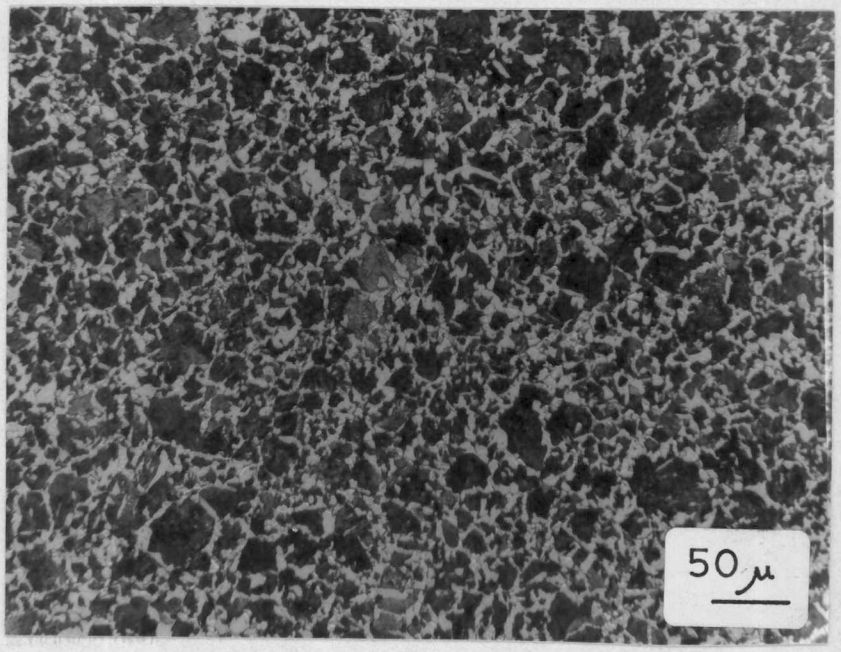

Figure 13. Core microstructure of non-decarburized specimens. OM 200x.

Decarburization lowers the amount of carbon in the steel and the primary effect of this is to reduce the amount of pearlite in the structure near the surface. This is shown in Figures 14 and 15, which are micrographs showing the structure of the decarburized and non-decarburized steels. Optical microscopy at 500x on the unetched metallographic specimens revealed no grain boundary oxides near the specimen surfaces. If these oxides were present, they were removed from the specimens by the polishing process.

The ferrite grains in Figure 14 appear larger than the ferrite grains in Figure 15, especially near the surface. A rough estimate of the ferrite grain size from a grain size determination and a manual point count (48) using 2000 points was made on the ferrite grains in the layer 0.005 inch (0.13 mm) from the specimen surface. The mean diameters of the ferrite grains was found to be 460 μ-in. (12μ) for the decarburized steel and 260 μ-in. (7μ) for the non-decarburized steel. Using Klesnil's (19) relation (Equation 4) to give an estimate of the effect of ferrite grain size on the fatigue limit, these grain sizes correspond to a 5-10% reduction in the fatigue limit for the decarburized steel.

Microhardness test. Another measure of the effect of decarburization on the properties of steel is the microhardness test. The results of the microhardness traverse are given in Appendix B and are summarized in Figure 16. The layer of steel near the surface depleted of carbon is softer than the same steel which is not decarburized. The equations of the fitted lines are:

$$HV = -0.1792 \times 10^{-9}(x)^4 + 0.6711 \times 10^{-6}(x)^3 - 0.8879 \times 10^{-3}(x)^2 + 0.4579(x) + 137.0 \quad (23)$$

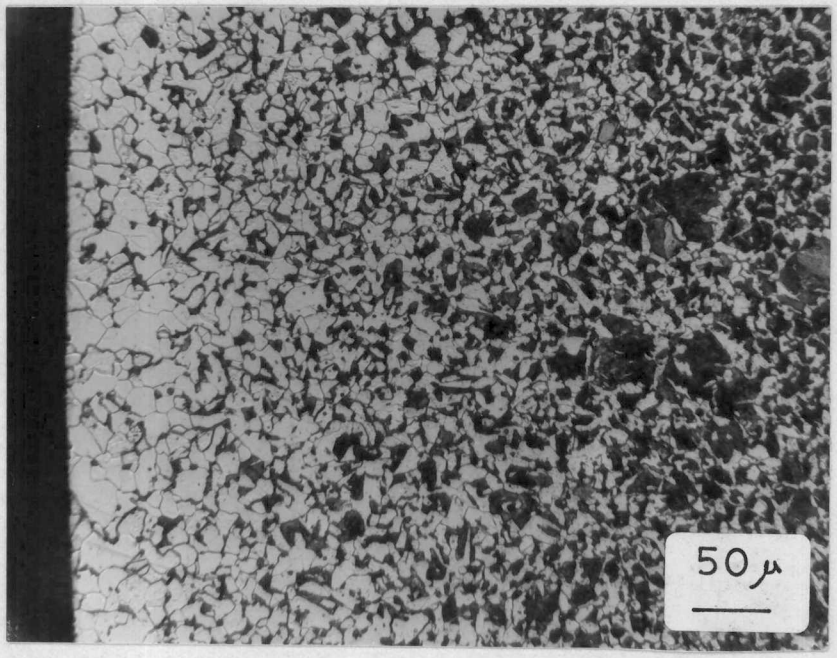

Figure 14. Surface microstructure of decarburized specimens. OM 200x.

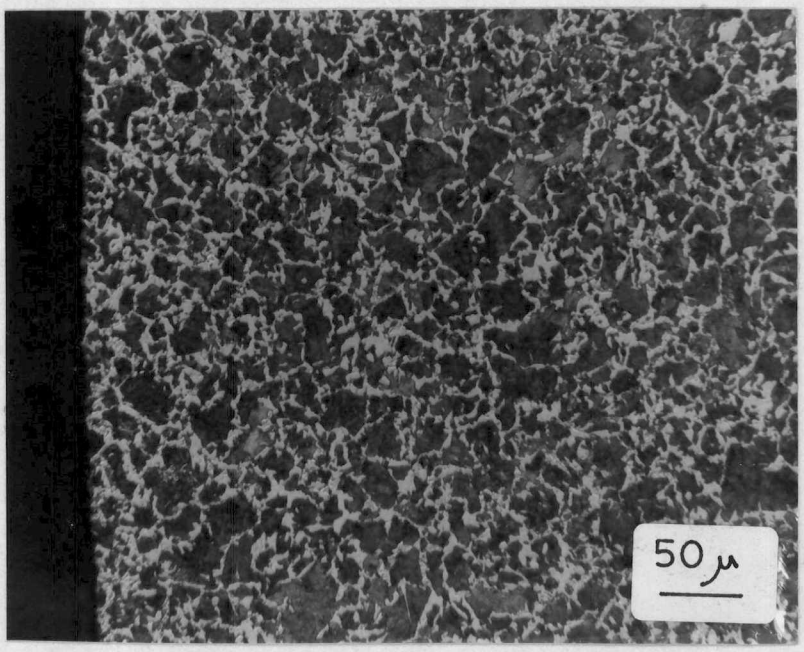

Figure 15. Surface microstructure of non-decarburized specimens. OM 200x.

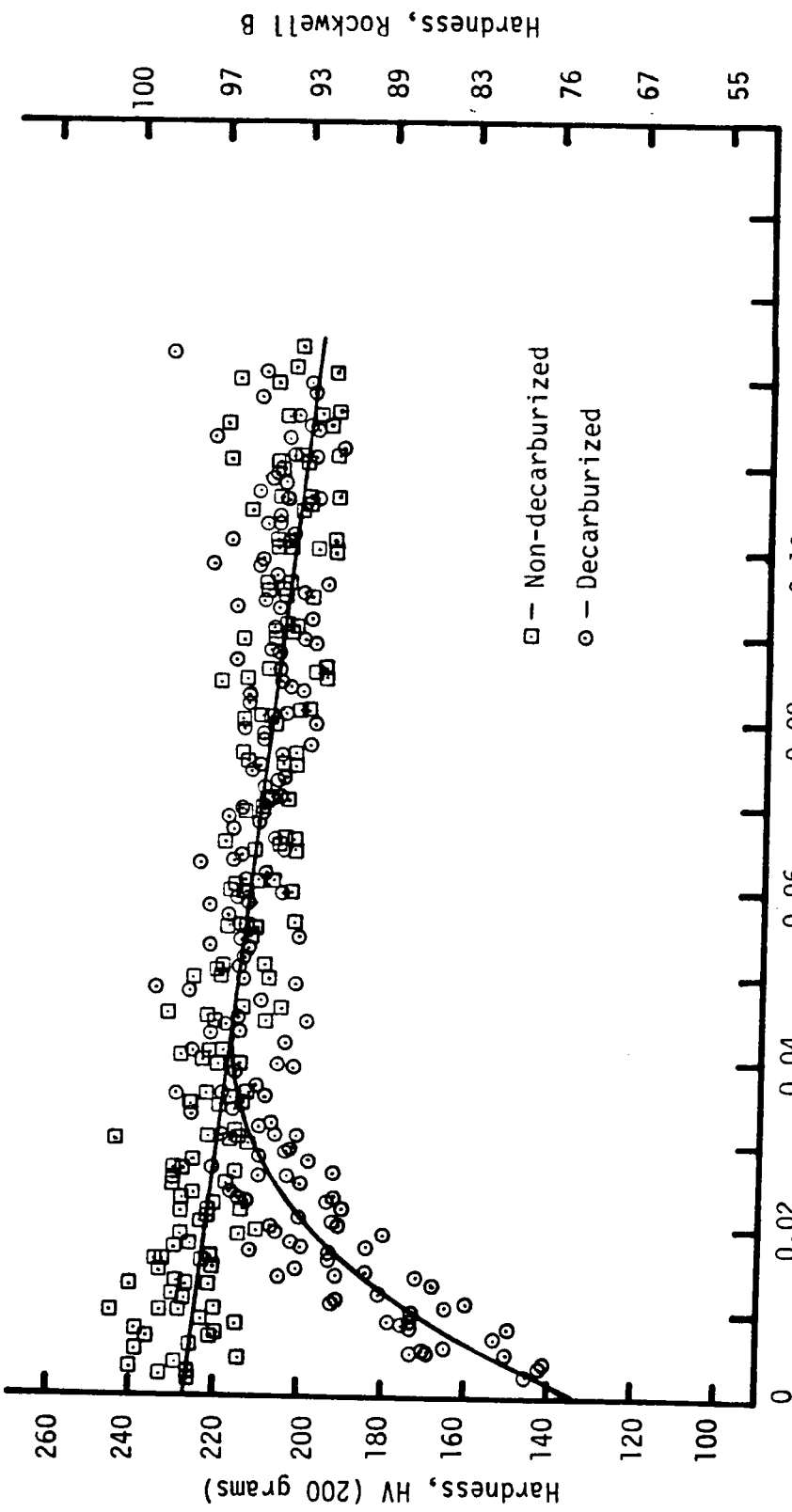

Figure 16. Depth of decarburization as determined by microhardness tests.

for the decarburized steel, and

$$HV = -0.2438(x) + 227.2 \qquad (24)$$

for the non-decarburized steel. Where HV is the Vicker's Hardness and x is the distance from the surface in inches times 10^4. The standard deviation of the regression for Equation 23 is 6.7 HV, and for Equation 24 it is 8.5 HV. The values of the standard deviation are about equal to the error in the actual microhardness tests. So, the uncertainty of the microhardness curves will be taken as $\pm$ 10 HV.

The depth of decarburization, taken as the point where these two fitted lines meet is 0.042 in. (1.07 mm). The severity, or difference between the surface hardness of the non-decarburized (227 HV or 97 HRB) and decarburized steels (137 HV, 76 HRB) is 90 HV or 21 HRB.

The higher order of Equation 23 was chosen in order to give a good fit (smallest standard deviation) to the data, especially in the region near the surface of the specimen where the hardness drops rapidly.

The hardness traverse for the non-decarburized material shows a slight decrease in hardness from surface to core. This is possibly due to a slightly lower cooling rate in the core which would result in a slightly smaller amount of pearlite in the core. The decrease in hardness is equal to 30 Vicker's hardness numbers, which is greater than the magnitude of the scatter of the data.

Tensile tests. The results of the tensile tests are summarized in Table IV. The data for the upper yield point (Y.P.), ultimate tensile strength (U.T.S.), and true stress of fracture are lower for the decarburized specimens. The tensile elongations of the decarburized specimens are not all greater than those for the non-decarburized specimens. Based on the average of three specimens, there appears to be a reduction in

TABLE IV

TENSILE TEST DATA FOR NORMALIZED 1042 STEEL

Specimen	Upper Yield Point, ksi (MPa)	Lower Yield Point, ksi (MPa)	Ultimate Tensile Strength, ksi (MPa)	Elongation Fracture, Percent	Reduction in Area at Fracture, Percent	True Strain at Fracture	True Stress at Fracture, ksi (MPa)
Decarburized							
T-002	62.3 (430)	59.4 (410)	98.4 (678)	23.9	34.4	0.421	171.8 (1185)
T-003	64.9 (447)	60.2 (416)	97.2 (670)	27.5	35.2	0.434	171.5 (1182
T-004	62.9 (434)	60.5 (417)	98.4 (678)	26.4	34.6	0.424	172.4 (1189)
Average, $\bar{x} \pm s$	63.4 ± 1.4 (437 ± 10)	60.0 ± 0.6 (414 ± 4)	98.0 ± 0.7 (676 ± 5)	25.9 ± 1.8	34.7 ± 0.4	0.426 ± 0.007	171.9 ± 0.5 (1185 ± 3)
Non-Decarburized							
T-005	67.9 (468)	60.8 (419)	98.8 (681)	20.7	34.1	0.417	179.8 (1240)
T-006	66.3 (457)	61.7 (425)	100.0 (690)	24.2	35.0	0.430	184.8 (1274)
T-007	68.6 (473)	62.0 (428)	102.0 (703)	26.4	34.4	0.421	184.5 (1272)
Average, $\bar{x} \pm s$	67.6 ± 1.2 (466 ± 8)	61.2 ± 1.1 (422 ± 7)	100.3 ± 1.6 (692 ± 11)	23.8 ± 2.9	34.5 ± 0.5	0.423 ± 0.007	183.0 ± 2.8 (1262 ± 19)

NOTES: $\bar{x}$ is the sample average and s is the standard deviation of the estimate. The elongation of fracture was measured with a gauge length of 1.4 inch (35.6 mm) to give a gauge length/diameter ratio of four.

strength and an increase in ductility in the decarburized specimens. But in most cases, the difference in Table IV between the decarburized and non-decarburized specimens is less than the sum of the standard deviations. This indicates that the differences are not statistically significant. The exceptions are the upper yield point and the true stress at fracture. Here the differences are statistically significant. In any case, these small differences do not have significance in an engineering sense because these differences would not cause concern in the routine testing of materials and components. As a result, the presence or absence of decarburization cannot generally be determined from tensile tests.

The tensile strength of the decarburized steel was expected to be lower (and the ductility higher) than the non-decarburized steel because the decarburized layer is softer than the core material. The tensile strength would be expected to decrease proportionally to the cross-sectional area of the decarburized layer up to the limiting case where the entire cross-section of the specimen is decarburized and the tensile strength is equal to the strength of the decarburized steel.

Although the decarburized layer is about 42% of the cross-sectional area, the reduction of the upper yield point and ultimate tensile strength are only 6% and 2%. This might initially appear to be too small a change in properties in terms of the decarburized cross-sectional area. However, it should be remembered that a carbon gradient exists in the decarburized layer. Additionally, the low yield strength decarburized layer is constrained by the higher strength core which increases the applied load at which the surface material yields. Once the

decarburized material does yield, work hardening will occur in that region to further decrease any difference in strength between the decarburized and non-decarburized specimens.

Results of the Fatigue Tests

Bending. The results of the fatigue tests in bending are given in Appendix C and presented as S-N curves in Figure 17. The fitted equation for the decarburized specimens is:

$$\sigma_x = - 3.616(\log_{10}N_f)^3 + 71.340(\log_{10}N_f)^2 - 474.600(\log_{10}N_f) + 1{,}102.900 \quad (25)$$

And, the fitted equation for the non-decarburized specimens is

$$\sigma_x = - 1.660(\log_{10}N_f)^3 + 37.130(\log_{10}N_f)^2 - 277.700(\log_{10}N_f) + 741.300 \quad (26)$$

Where σ_x is the reversed bending stress in thousands of pounds per square inch (ksi) and N_f is the number of cycles to failure.

When comparing the fatigue data, the fitted curves will be used. The standard deviation of the regression for Equation 25 is 7.4 ksi (51 MPa) and for Equation 26 it is 6.2 ksi (43 MPa). The uncertainty of the estimated values determined using the fitted equation will be taken as ± 3.7 ksi (26 MPa) for Equation 25 and ± 3.1 ksi (21 MPa) for Equation 26. These values are greater than the estimate of the error in calibration (± 2.5 ksi (18 MPa)). Differences in the fatigue strength greater than the sum of the uncertainties will be considered significant.

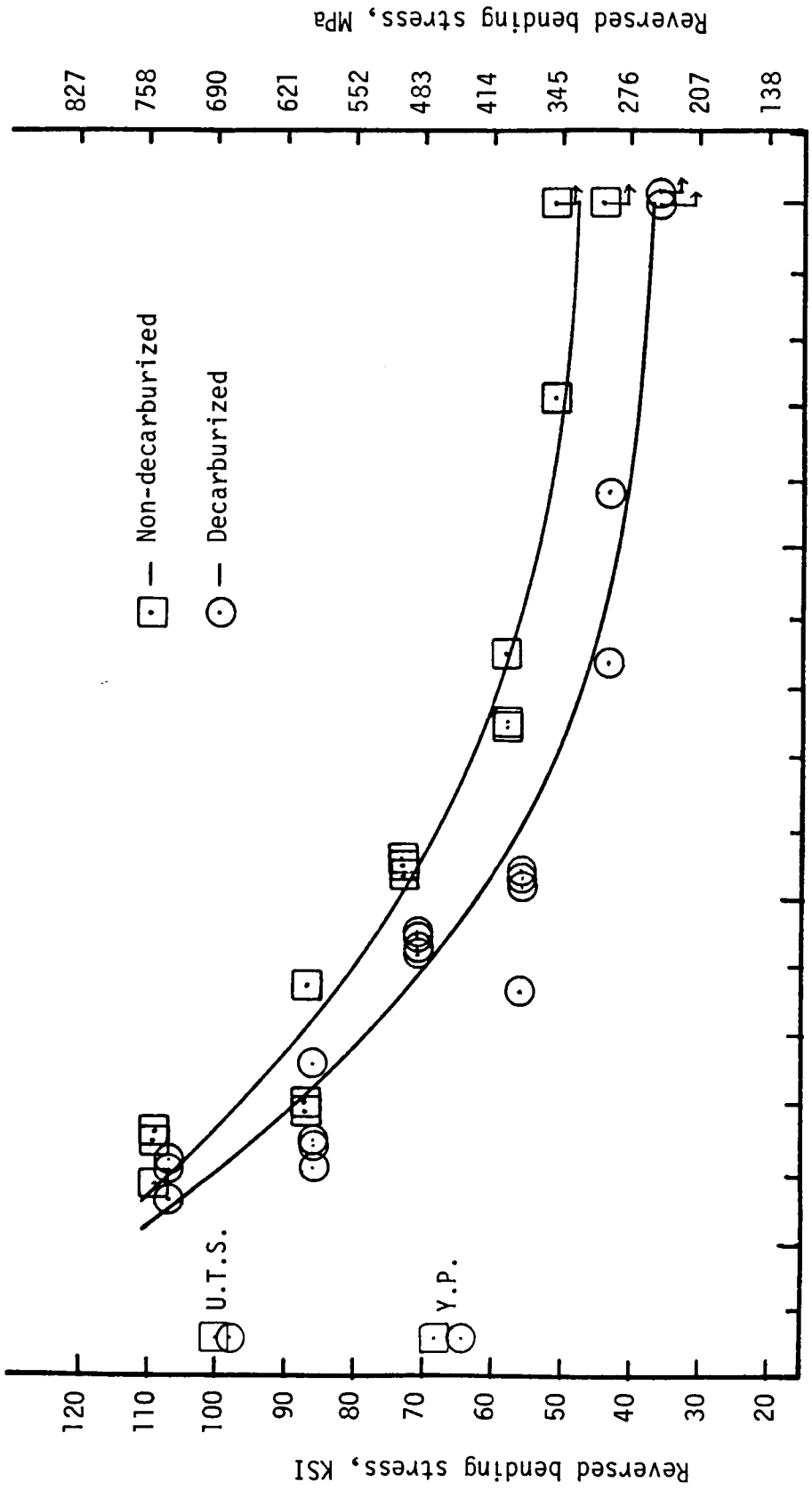

Figure 17. S-N curves for bending.

The fatigue limits are 47.4 ± 3.8 ksi (327 ± 26 MPa) for the non-decarburized steel and 35.7 ± 3.1 ksi (246 ± 21 MPa) for the decarburized steel. Here the ± 8% uncertainty of determing the fatigue limits (discussed in Chapter II, page 46) is greater than the uncertainty of the fitted equations. So, ± 8% is used as the uncertainty in the fatigue limits.

Although there is some scatter in the data, the S-N curve for the decarburized specimens is below the curve for the non-decarburized specimens at all points in Figure 17. At the highest stress levels tested, 107 ksi (748 MPa) and 109 ksi (761 MPa), the data for the two groups of specimens overlap. The difference here is not significant. For instance, at $10^{4.1}$ cycles (12590 cycles) the fatigue strength determined for the decarburized specimens is 107 ksi (748 ksi) and for the non-decarburized specimens the fatigue strength is 112 ksi (782 MPa). The difference is 5 ksi (35 MPa). At this point, the difference is less than 6.8 ksi (the sum of the uncertainties of the fitted equations) and is not significant.

At a greater number of cycles to failure, the differences in the fatigue strengths are greater (10 ksi (70 MPa) or more) and these differences are significant. At $N_f = 10^{4.2}$ cycles (15,850 cycles), the reduction in fatigue strength due to decarburization is 6.4%. at 10^5 and 10^6 cycles, the reduction due to decarburization is 17% and 21%. At the fatigue limit, the reduction due to decarburization is 25%. These are significant amounts of reduction in the fatigue strengths and the fatigue limit.

Torsion. The results of the fatigue tests in torsion for the decarburized and non-decarburized specimens is given in Appendix C. The S-N curves for this torsion data are presented in Figure 18. The fitted equation for the data for decarburized specimens is:

$$\tau_{xy} = -2.556(\log_{10}N_f)^3 + 50.970(\log_{10}N_f)^2 - 344.100(\log_{10}N_f) + 807.100 \quad (27)$$

And the fitted equation for the non-decarburized specimens is:

$$\tau_{xy} = -3.178(\log_{10}N_f)^3 + 61.870(\log_{10}N_f)^2 - 408.900(\log_{10}N_f) + 947.600 \quad (28)$$

where τ_{xy} is the reversed torsion stress in ksi.

Also plotted on Figure 18 is the ultimate tensile strength and yield points, determined from the uniaxial tensile tests and converted to an equivalent shear stress using Equation 10.

As before, the fitted curves will be used to compare the fatigue data. The standard deviation of the regression for Equation 27 is 3.6 ksi (24 MPa) and for Equation 28 it is 2.4 ksi (16 MPa). The uncertainty of the estimated values determined using the fitted equation will be taken as $\pm$ 1.8 ksi (12 MPa) for Equation 27 and $\pm$ 1.2 ksi (8 MPa) for Equation 28. These values are greater than the estimate of the error in calibration for torsion ($\pm$ 1.0 ksi (7 MPa)) and will be used when comparing the data.

The fatigue limits in torsion are 26.6 $\pm$ 2.1 ksi (183 $\pm$ 15 MPa) for the non-decarburized and 18.7 $\pm$ 1.5 ksi (129 $\pm$ 10 MPa) for the decarburized steel. Here the $\pm$ 8% uncertainty in determining the fatigue limits (discussed in Chapter II, page 46) is greater than the uncertainty

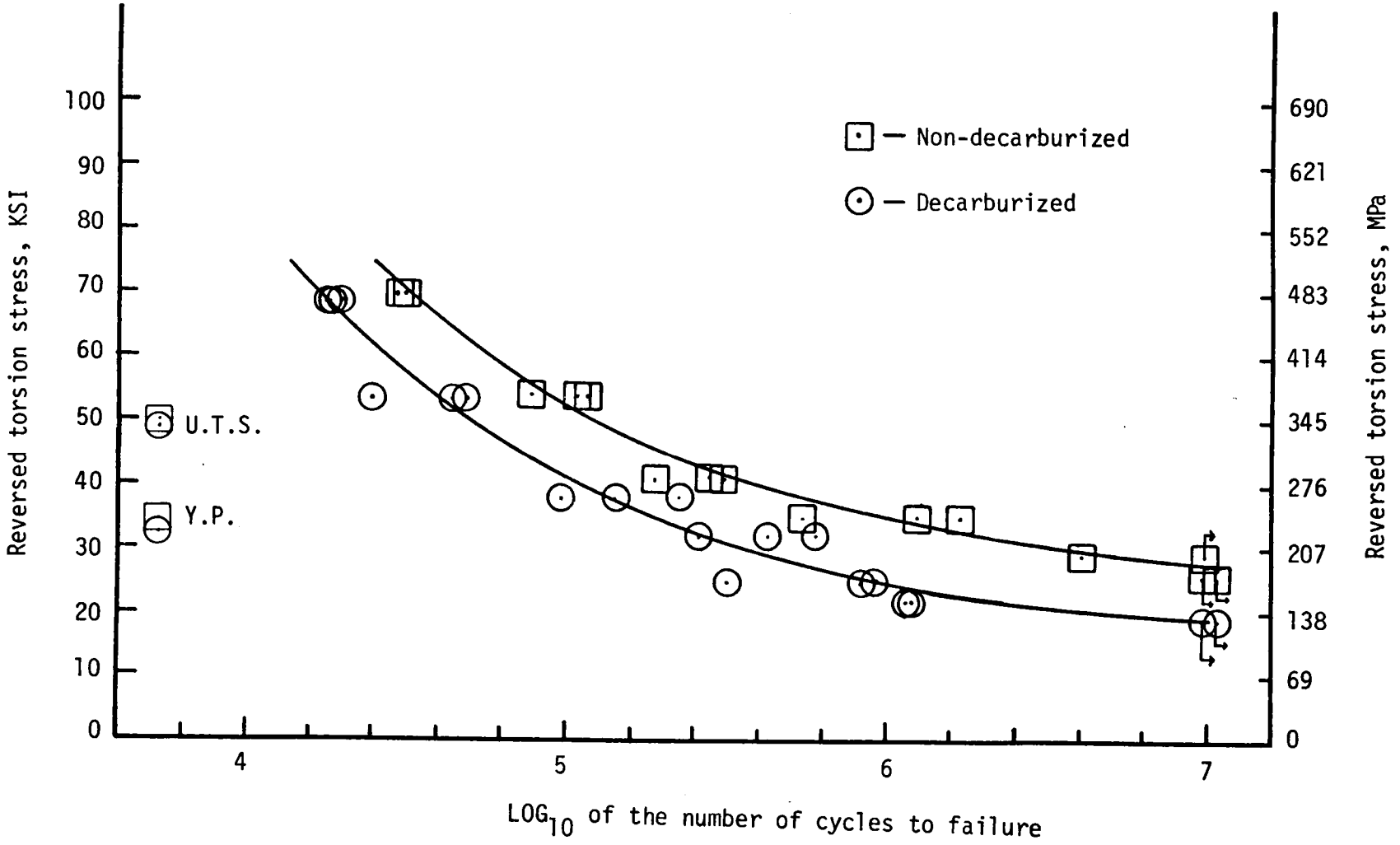

Figure 18. S-N curves for torsion.

of the fitted equations and ± 8% is used as the uncertainty of the fatigue limits at 10^7 cycles.

The fatigue strengths and the fatigue limit for the decarburized steel are less than those for the non-decarburized steel as illustrated in Figure 18. The results are similar to the S-N curves in bending, except that the difference in fatigue life is greater for the group of specimens at the highest stress levels tested, 69.5 ksi (486 MPa) and 70.1 ksi (490 MPa) for the decarburized and non-decarburized steels.

The differences in fatigue strength in the range of the data obtained are about 10 ksi (70 MPa). These differences are greater than the sum of the uncertainties of the fitted equations, 3.1 ksi, and are significant. The percent reduction in fatigue strength due to decarburization at $N_f = 10^{4.5}$ cycles (31,620 cycles) is 18%. At 10^5 and 10^6 cycles the reduction is 22% and 28%. At the fatigue limit at 10^7 cycles, the reduction due to decarburization is 30%. These are significant amounts of reduction in the fatigue strengths and the fatigue limit. The data indicate a slightly higher degradation of the fatigue limit in torsion (30%) as compared to bending (25%).

Comparison to Previous Results

It is of interest to compare the present results to Bales' (1) results in bending for the same material, 1042 steel. This comparison is done in Figure 19 where Bales' fitted curves are replotted on the same scale with the present fitted curves. The specimen preparation procedures were nearly identical except that the resultant surface roughness measured by Bales was 20 μ-in. (0.5μ) versus 3-4 μ-in. (0.07-0.10μ). A significant difference in the testing was that Bales used a rotating-bending fatigue machine (constant load) where the present data were obtained on a plane-bending machine (constant displacement).

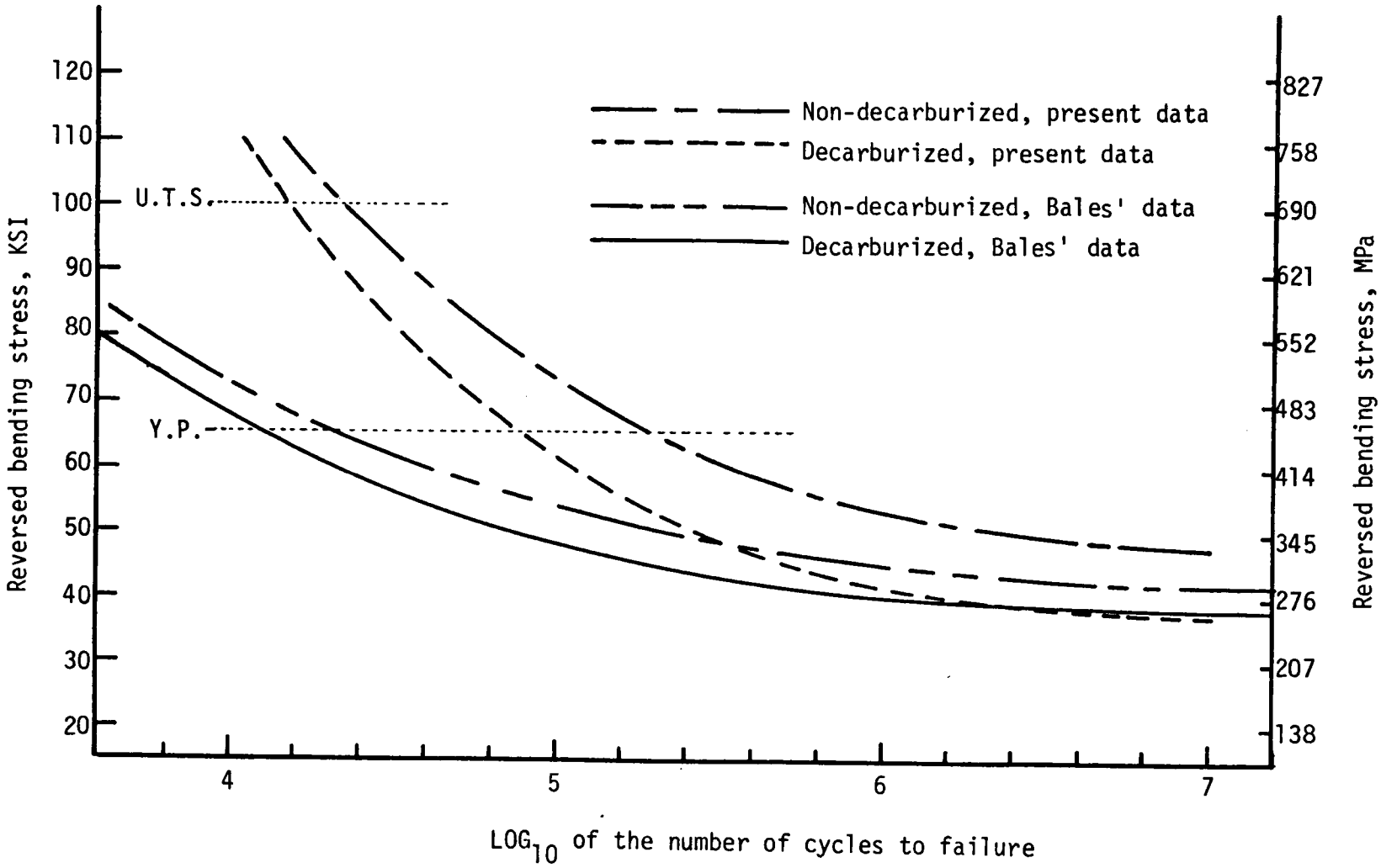

Figure 19. S-N curves for bending; comparison of present data to Bales (1). The ultimate tensile strength and yield point strength here represent average values from both sets of data. See the text for the explanation of the data above the ultimate tensile strength.

At 10^7 cycles, the present data show a greater fatigue limit than Bales' data for the non-decarburized steels by 13%. For the decarburized steels, the fatigue limit for the present data is less than that for Bales data by 8%. The significance of these differences cannot be determined because Bales did not report the uncertainty of his data. At any rate, the differences are fairly small. One may expect a reduction of the fatigue limit with an increased surface roughness (5, 8, 33, 34, 37). This was not observed for the decarburized specimens. Apparently the effect of increasing the surface roughness on the fatigue limits is too small to be detected with the experimental methods used in this study and in Bales' study.

A difference between rotating-bending and plane bending is that in rotating-bending more prospective initiation sites are subjected to the maximum stress in the cycle. This situation could cause a lower fatigue limit in rotating-bending because there is a greater probability that a crack may initiate at a notch or metallurgical discontinuity in rotating-bending. This effect was not verified in the present study.

At higher stresses, the two sets of data diverge greatly. At 10^5 cycles to failure, for instance, the present data for fatigue strength are 27% and 36% greater than Bales' data for decarburized and non-decarburized steels. This is consistent with the fact that for the constant load machine (Bales) most of the fatigue life, or number of cycles to failure, is in the crack initiation stages while for the constant displacement machine, most of the fatigue life is in crack propagation stage. The fatigue life is much greater if the specimen does not break immediately after crack initiation.

The fatigue life for Bales' data for the non-decarburized steel is only 10% of the present data in the range of 50-90 ksi (350-620 MPa) bending stress. And, the fatigue life for Bales' data for the decarburized steel is about 17% of the present data in the range of 50-90 ksi (350-620 MPa) bending stress. The applied stress level at the beginning of the fatigue tests are the same for both types of loading, constant load or constant displacement. There is no crack present to change the applied load with these two loading systems, and the stresses are calculated using the same elastic bending formula (Equation 16).

If one assumes that the number of cycles in the crack initiation stage is the same for both types of loading, and for finite life specimens under constant load, the fatigue life is all in the crack initiation stage; then one can conclude that for the present data in bending, the number of cycles in the crack propagation stages is at least 80% of the fatigue life. This conclusion is significant in that it has bearing on the interpretation of the fatigue data and the analysis of the results.

It is worth noting the values of the yield stress and ultimate tensile strength in relation to the S-N curves. The yield point is about 65 ksi (454 MPa) and the ultimate tensile strength, about 100 ksi (690 MPa) for both the decarburized and non-decarburized steel. The present data diverge from Bales' data at stress levels above the fatigue limit. The fatigue limit for the decarburized steel is below the yield point at 35.7 ksi (246 MPa) which is 56% of the yield point strength and 36% of the ultimate tensile strength. Similarly, the fatigue limit for the non-decarburized steel is 47.4 ksi (327 MPa) which is 70% of the yield point strength and 47% of the ultimate tensile strength.

At a stress level equal to the ultimate tensile strength, one would expect failure on the first application of the tensile stress in the fatigue cycle, that is in one-quarter cycle. The present data show fatigue lives at the ultimate tensile strength on the order of 10^4 cycles. This can be explained by noting two points. First, the calibration used was based on the elastic bending formula (as was Bales' (1)). This formula gives increasing errors at higher stress levels due to the increasing amount of plastic deformation in be specimen. Although the actual applied stress is lower than that calculated using an elastic formula, the fatigue data obtained are still useful for comparative purposes. Second, as noted previously, the applied stress level decreases in a constant displacement machine as soon as a crack appears. So, even if a crack formed on the first quarter-cycle, the specimen would not fracture completely. The large number of cycles to cause failure in fatigue at the ultimate tensile strength consists mostly of cycles spent in the crack propagation stages.

Comparison to Failure Criteria

One may compare the results of fatigue tests to the failure criteria for biaxial loading in a number of ways. One may compare f_o/q_o ratios (35, 36) that is, the ratio of the fatigue limit in bending to the fatigue limit in bending to the fatigue limit in torsion, replot the S-N curves in terms of maximum shear stress or octahedral shear stress, or plot failure envelopes in principal stress space.

Tables V and VI summarize the comparison of the fatigue data to the maximum shear stress and the octahedral shear stress criteria. In these tables, the symbols f_s and q_s are used to represent the fatigue

TABLE V

COMPARISON OF THE FATIGUE STRENGTHS IN BENDING AND TORSION FOR DECARBURIZED STEEL

Number of Cycles to Failure	Fatigue Strength, [b,c] ksi	Equivalent Strength Based on Maximum Shear Stress, ksi	Difference, percent[a]	Significant?	Equivalent Strength Based on Octahedral Shear Stress, ksi	Difference, percent[a]	Significant?	$\frac{f_s}{q_s}$ or $\frac{f_o}{q_o}$
maximum shear stress criterion	f_s q_s	1/2 f_s q_s	0					2.00
octahedral shear stress criterion	f_s q_s				$\sqrt{2}/3\ f_s$ $\sqrt{6}/3\ q_s$	0		1.73
$10^{7.0}$	$f_o = 35.7$ $q_o = 18.7$	17.8 18.7	4.8	no	16.8 15.3	-10	no	1.90
$10^{6.5}$	$f_s = 38.7$ $q_s = 21.6$	19.4 21.6	10	no	18.3 17.6	3.7	no	1.80
$10^{6.0}$	$f_s = 42.2$ $q_s = 24.9$	21.1 24.9	15	no	19.9 20.4	2.4	no	1.69
$10^{5.5}$	$f_s = 48.7$ $q_s = 30.8$	24.4 30.8	21	yes	23.0 25.2	8.7	no	1.58
$10^{5.0}$	$f_s = 61.1$ q_s 41.0	30.6 41.1	26	yes	28.8 33.5	14	yes	1.49
$10^{4.5}$	$f_s = 82.1$ $q_s = 57.6$	41.1 57.6	29	yes	38.7 47.0	18	yes	1.42
Bending Torsion (Uncertainty)*	± 3.7 ± 1.8	± 1.9 ± 1.8			± 1.8 ± 1.5			

[a] Percent difference = $100 \times \frac{\text{equivalent strength in torsion - equivalent strength in bending}}{\text{equivalent strength in torsion}}$

[b] f_s = fatigue strength in bending

[c] q_s = fatigue strength in torsion

*Uncertainty at the fatigue limits is ± 8%

TABLE VI

COMPARISON OF THE FATIGUE STRENGTHS IN BENDING AND TORSION FOR NON-DECARBURIZED STEEL

Number of Cycles to Failure	Fatigue Strength, [b,c] ksi	Equivalent Strength Based on Maximum Shear Stress, ksi	Difference, percent [a]	Significant?	Equivalent Strength Based on Octahedral Shear Stress, ksi	Difference, percent [a]	Significant?	$\frac{f_s}{q_s}$ or $\frac{f_o}{q_o}$
[maximum shear stress criterion]	f_s q_s	$1/2\ f_s$ q_s	0					2.00
[octahedral shear stress criterion]	f_s q_s				$\sqrt{2}/3\ f_s$ $\sqrt{3}/3\ q_s$	0		1.73
$10^{7.0}$	$f_o = 47.4$ $q_o = 26.6$	23.7 26.6	11	no	22.3 21.7	-3.0	no	1.78
$10^{6.5}$	$f_s = 49.1$ $q_s = 30.7$	24.6 30.7	20	yes	23.2 25.1	7.7	no	1.60
$10^{6.0}$	$f_s = 53.2$ $q_s = 34.8$	26.6 34.8	24	yes	25.1 28.4	12	yes	1.53
$10^{5.5}$	$f_s = 60.9$ $q_s = 41.3$	30.5 41.3	26	yes	28.7 33.7	15	yes	1.48
$10^{5.0}$	$f_s = 73.5$ $q_s = 52.4$	36.8 52.4	30	yes	34.7 42.8	19	yes	1.40
$10^{4.5}$	$f_s = 92.2$ $q_s = 70.6$	46.1 70.6	35	yes	43.5 57.7	25	yes	1.31
[Bending Torsion (Uncertainty)*]	± 3.1 ± 1.2	± 1.6 ± 1.2			± 1.5 ± 1.0			

[a] Percent difference = $100 \times \frac{\text{equivalent strength in torsion} - \text{equivalent strength in bending}}{\text{equivalent strength in torsion}}$

[b] f_s = fatigue strength in bending

[c] q_s = fatigue strength in torsion

*Uncertainty at the fatigue limits is ± 8%

strength in bending and in torsion, similar to the f_o and q_o which were introduced in the literature review to represent the fatigue limits at 10^7 cycles in bending and in torsion.

As stated in the literature review, if $f_o/q_o = 2$, the maximum shear stress criterion is verified and if $f_o/q_o = 1.73$, the octahedral shear stress criterion is verified. At 10^7 cycles, the present data gives $f_o/q_o = 1.91$ for the decarburized and $f_o/q_o = 1.78$ for the non-decarburized steel for the fatigue limits. This ratio allows comparison to large body of data reviewed by Pope (33) for which the average $f_o/q_o = 1.68$ and by Frost, Marsh, and Pook (37) for which the average $f_o/q_o = 1.82$, all using the fatigue limits at 10^7 cycles.

Both fatigue limit ratios for the decarburized and non-decarburized specimens fall between that predicted for the maximum shear stress criterion and octahedral shear stress criterion. The data for the decarburized steel are closer to the maximum shear stress criterion, while the non-decarburized steel and the averages of the literature data are closer to the octahedral shear stress criterion.

Comparing ratios of f_s/q_s, the fatigue strength in bending and torsion, one does not get a very good correlation at a lower number of cycles to failure. The f_s/q_s ratio decreases with a decreasing number of cycles to failure as shown in Tables V and VI.

For the decarburized steel, the ratio decreases from 1.91 to 1.42 at the highest stress level tested, and for the non-decarburized steel it changes from 1.78 to 1.31. The maximum stress level tested corresponds to a fatigue life of about 3×10^4 cycles.

One may also plot S-N curves in terms of the equivalent stresses, the maximum shear stress, τ_{max},

$$\tau_{max} = \frac{\sigma_1 - \sigma_3}{2} \tag{29}$$

or the octahedral shear stress, τ_{oct},

$$\tau_{oct} = 1/3 \left[(\sigma_1 - \sigma_2)^2 + (\sigma_2 - \sigma_3)^2 + (\sigma_1 - \sigma_3)^2 \right]^{1/2} \tag{30}$$

where σ_1, σ_2, and σ_3 are the principal stresses. The reversed bending stress or reversed torsion stress may be converted to an equivalent maximum shear stress or octahedral shear stress using these formulae. Calculated values of the equivalent fatigue strengths are tabulated in Tables V and VI. The percentage differences are also tabulated. If the difference between the equivalent fatigue strength (or fatigue limit) in bending and torsion is zero, then the failure criterion is verified. This is illustrated in the first two entries in Tables V and VI. Similarly, if the S-N curves based on an equivalent stress (Equations 29 and 30) and using data for bending, torsion, or any other biaxial state of stress are superimposed, then the failure criteria are verified. This allows evaluation of a criterion at various fatigue lives, but it is convenient to look at only one criterion at a time.

Figure 20 shows the S-N curves replotted on the basis of maximum shear stress. The two curves in torsion, for the decarburized and non-decarburized specimens, are everywhere above the converted curves for

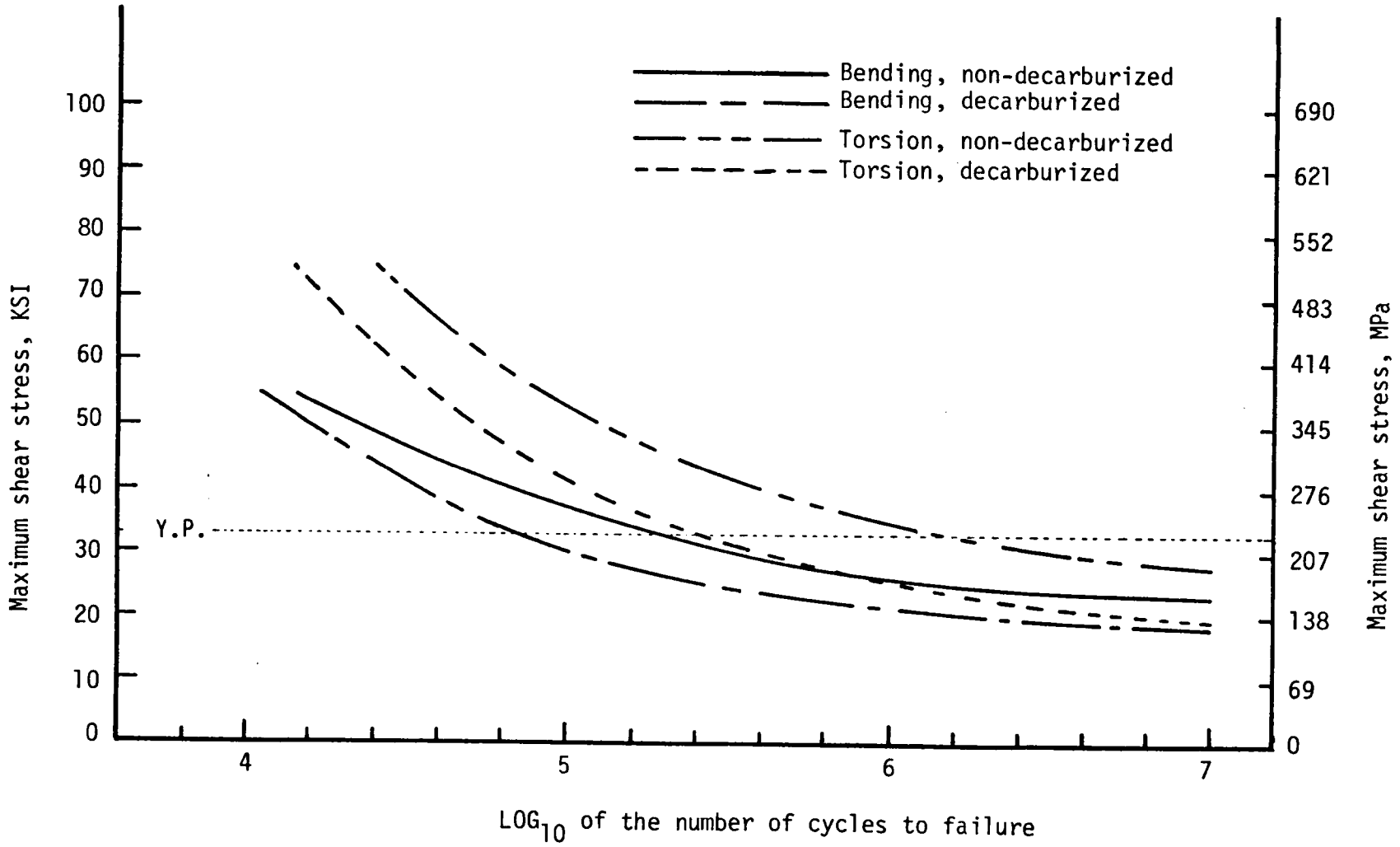

Figure 20. Comparison of the S-N curves for bending and torsion on the basis of maximum shear stress.

bending. At the fatigue limit, the curves are closest together. At the fatigue limit at 10^7 cycles, the converted bending curves are 4.8% and 10.8% less than the curves for torsion for the decarburized and non-decarburized specimens respectively. At 10^5 cycles, the converted fatigue strengths in bending are 25.5% and 27.8% less than the fatigue strengths for torsion.

Figure 21 shows the S-N curves replotted on the basis of octahedral shear stress. At lower number of cycles, the S-N curves for converted torsion are above the converted curves for bending. At 10^5 cycles to failure, the converted curves for bending are 14.0% and 19.0% below the curves for converted torsion for the decarburized and non-decarburized specimens, respectively. At some point the converted curves for torsion and bending cross, so that at 10^7 cycles to failure the converted curves for torsion are below the converted curves for bending. At the fatigue limit (10^7 cycles to failure) the converted curves for bending are 10.0% and 3.0% greater than the converted curves for torsion for the decarburized and non-decarburized specimens.

As stated previously (page 46), the uncertainty in determining the fatigue limits is ± 8%. With this in mind, none of the percentage differences at 10^7 cycles in Tables V and VI are significant. The uncertainty for fatigue strengths is also given in Tables V and VI in terms of equivalent stresses. Using these values, the differences in equivalent fatigue strength become significant at about 10^6 cycles and less.

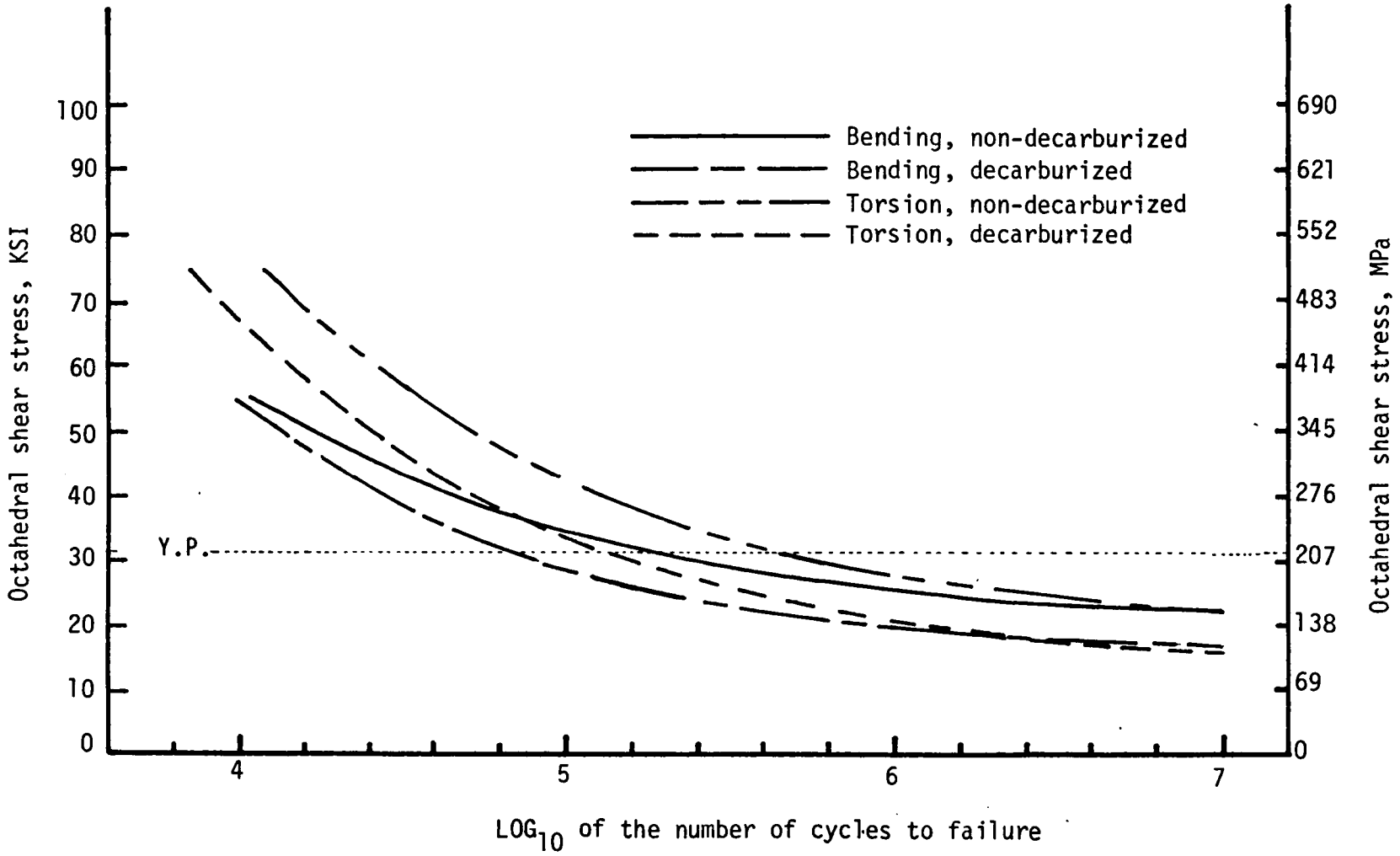

Figure 21. Comparison of S-N curves for bending and torsion on the basis of octahedral shear stress.

Again, the failure criteria are satisfied fairly well at the fatigue limit, but not at higher stresses or shorter fatigue lives.

The failure criteria can also be plotted in principal stress space. Here, the fatigue strength at a certain number of cycles to failure are plotted using the two principal stresses as axes. The loci of equivalent stresses are plotted, based either on maximum shear stress, or octahedral shear stress, with the critical stress for failure defined by the fatigue strength in bending. This plot is shown for the present data in Figure 22 for $N_f = 10^7$, 10^6, 10^5, and $10^{4.5}$ cycles to failure. The uncertainty of each datum point is marked on the figure. Note that the position of curves for the failure criteria are fixed by, and have the same uncertainty, as the fatigue strength in bending.

The percentage differences between the fatigue strength (or fatigue limits) in torsion and the failure criteria are the same percentage differences quoted in Tables V and VI for the differences between the equivalent fatigue strengths in bending and in torsion. Here, the percentage differences are based on radial differences from the origin in principal stress space.

At 10^7 cycles to failure, the failure criteria are able to predict the fatigue behavior of both decarburized and non-decarburized specimens fairly well. At 10^6 cycles to failure, the octahedral shear stress criterion appears to fit the data more closely. As seen in Figure 22, at 10^5 and $10^{4.5}$ cycles to failure, the values predicted by the failure criteria are significantly less than the actual fatigue strengths in

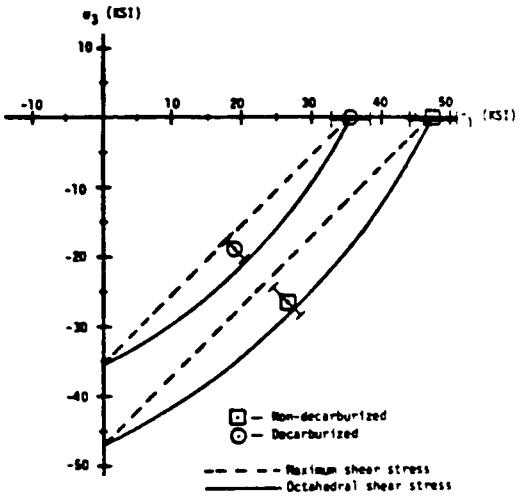

(a) $N_f = 10^7$ cycles

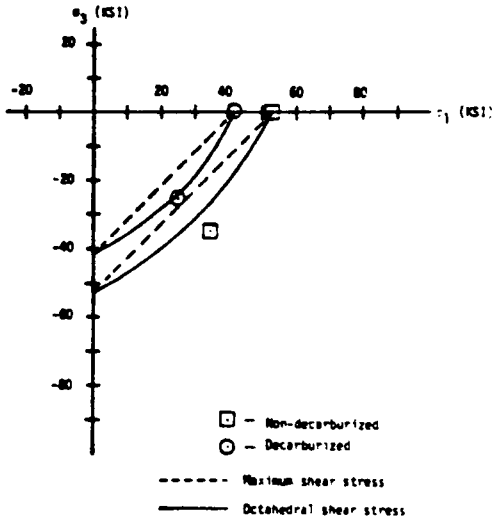

(b) $N_f = 10^6$ cycles

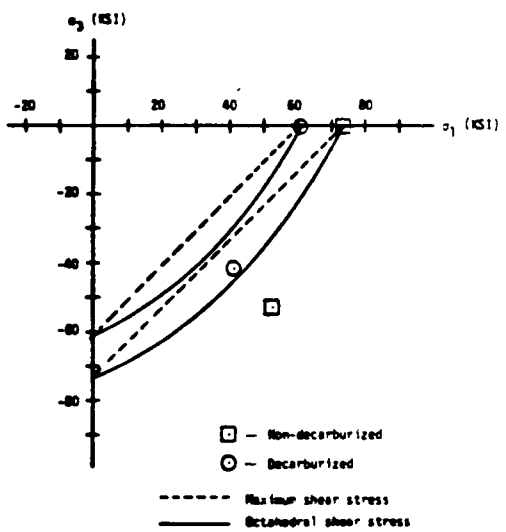

(c) $N_f = 10^5$ cycles

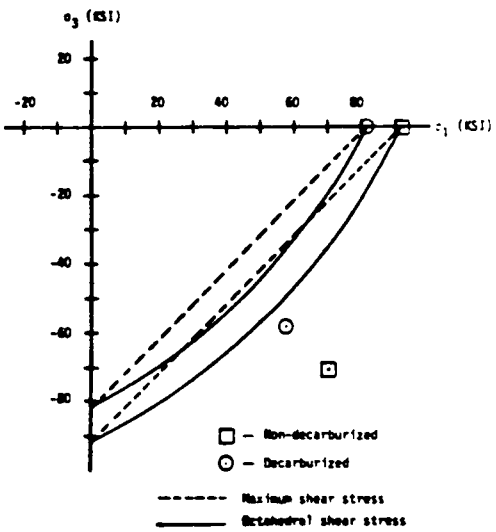

(d) $N_f = 10^{4.5}$ cycles

Figure 22. Comparison of the fatigue limits and fatigue strengths in bending and torsion to the maximum shear stress and the octahedral shear stress criteria. The uncertainty bands are indicated on (a). The uncertainty bands for (b), (c), and (d) are approximately the same size as the data points. The fatigue strengths were obtained from Equations 25 to 28. N_f is the number of cycles to failure.

torsion. The large deviations from the failure criteria occur at fatigue strengths above the yield point stress (about 65 ksi in tension).

Apparently, both criteria are able to predict long life behavior fairly well, but cannot predict behavior for loading above the yield strength.

Macroscopic Fractography

The fractured specimens were examined macroscopically (up to 30 times magnification) in order to characterize any differences between the decarburized and non-decarburized specimens, and between specimens loaded in bending and torsion.

The typical appearance of the fracture surfaces for specimens tested in bending are illustrated in Figures 23 to 28, for the non-decarburized and decarburized specimens tested at various stress levels. The appearance of these surfaces is similar in most respects. In bending, all of the cracks initiated on the top or bottom of the specimen as mounted in the fatigue machine. These locations undergo the same maximum stress in a cycle but 180 degrees out of phase. This is illustrated in Figure 23 where the top of the macrograph corresponds to the "up" direction of the specimen, as mounted horizontally in the fatigue machine. Two major crack fronts propagated by fatigue on a plane normal to the specimen axis. At a central line on the fracture surface (Figures 23, 24, 26) final failure occurred. At a stress level just above the fatigue limit, one of the crack fronts was usually dominant, so that this one crack extended over a larger portion of the fracture surface (Figures 25 and 28). Since the test is conducted at constant deflection, the tensile overload area is very small.

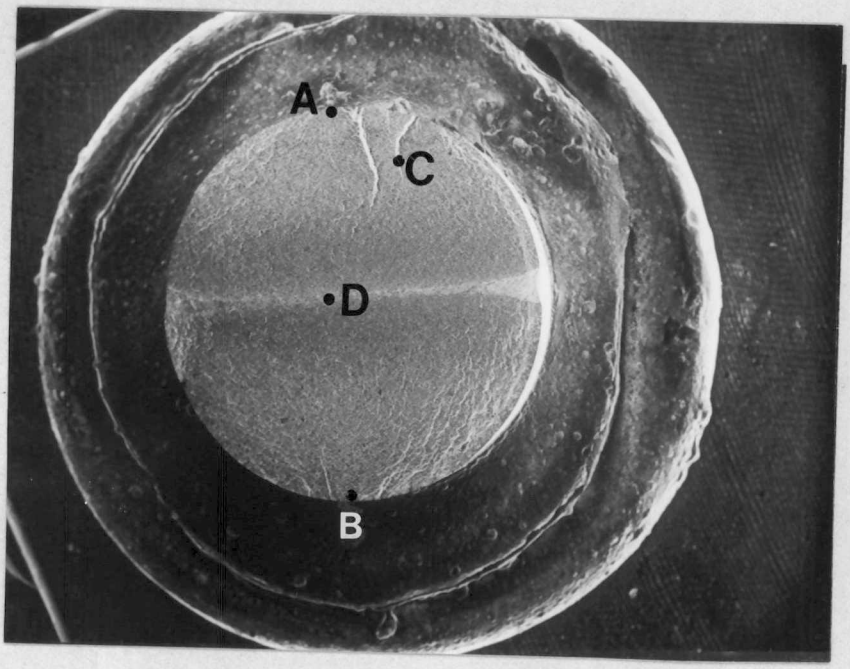

Figure 23. Macroscopic appearance of a non-decarburized fatigue specimen, tested at 108.9 ksi (750 MPa) (161% of the Y.P. and 109% of the U.T.S.) in bending. The specimen failed after 1.98×10^4 cycles. Points A and B are crack initiation sites on the top and bottom of the specimen as mounted in the fatigue machine. Point C is a ratchet mark. Point D is on the central line where final fracture occurred. SEM 10x.

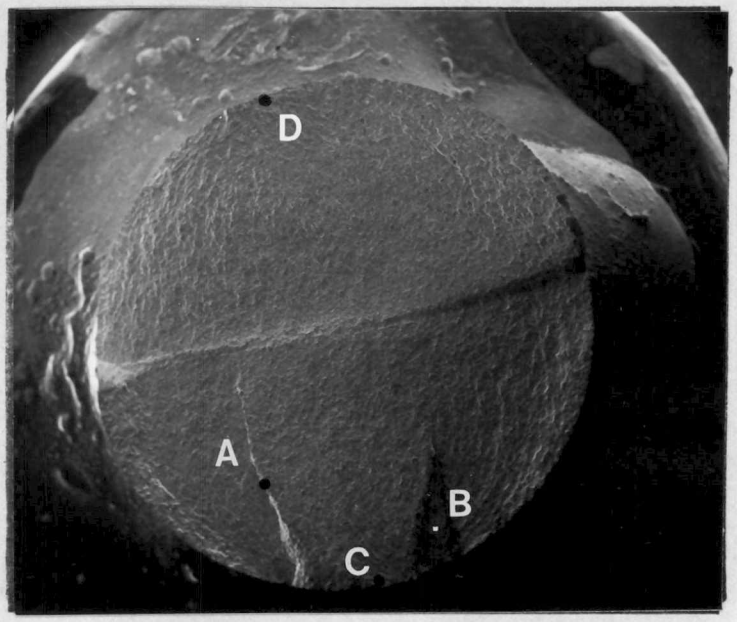

Figure 24. Macroscopic appearance of a non-decarburized fatigue specimen tested at 87.1 ksi (600 MPa) (129% of the Y.P. and 87% of the U.T.S.) in bending. The specimen failed after 5.53×10^4 cycles. Points A and B are ratchet marks and point C and D are crack initiation sites. SEM 12x.

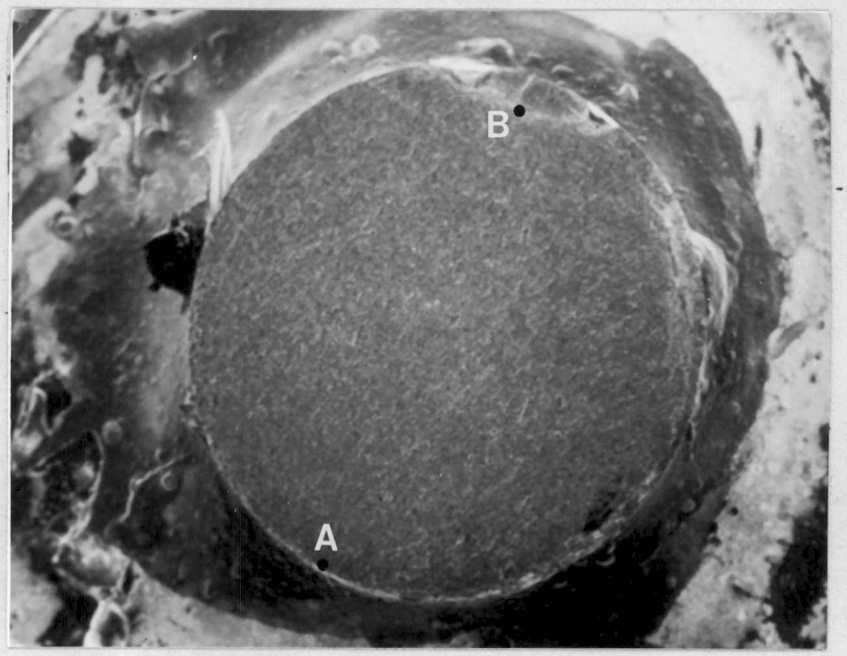

Figure 25. Macroscopic appearance of a non-decarburized fatigue specimen, tested at 58.1 ksi (400 MPa) (86% of the Y.P. and 58% of the U.T.S.) in bending. The specimen failed after 4.921×10^5 cycles. A crack initiating at point A propagated over most of the specimen and terminated at point B. No ratchet marks are seen in this macrograph. SEM 12x.

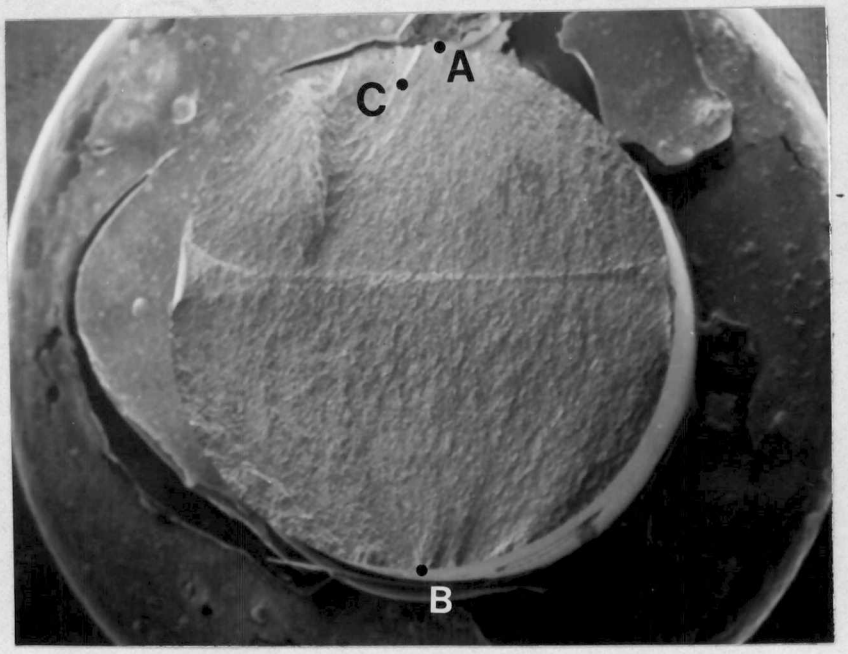

Figure 26. Macroscopic appearance of decarburized fatigue specimen, tested at 107.1 ksi (738 MPa) (169% of the Y.P. and 109% of the U.T.S.) in bending. The specimen failed after 1.76×10^4 cycles. Points A and B are crack initiation sites and point C is a ratchet mark. SEM 12x.

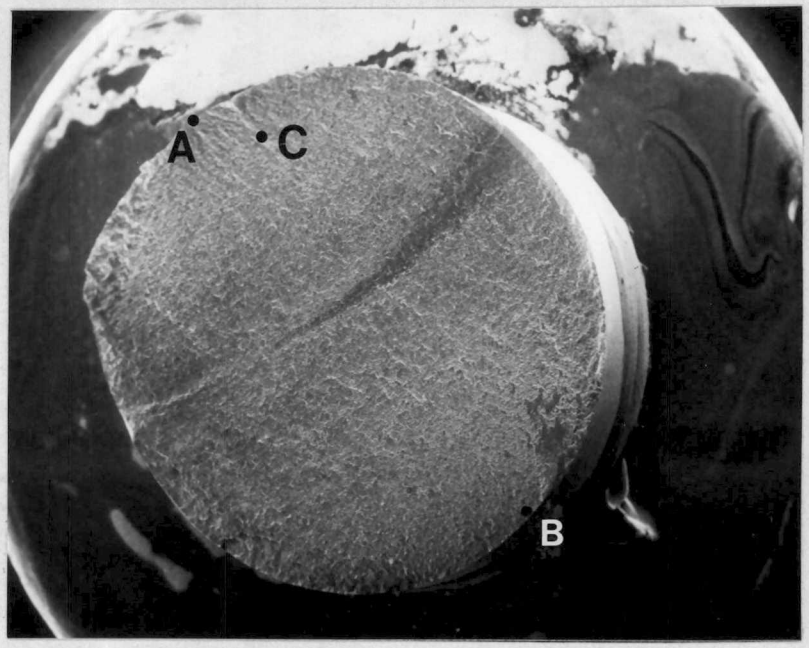

Figure 27. Macroscopic appearance of a decarburized fatigue specimen, tested at 85.7 ksi (591 MPa) (135% of the Y.P. and 87% of the U.T.S.) in bending. The specimen failed after 1.96×10^4 cycles. Points A and B are crack initiation sites, and point C is a ratchet mark. SEM 12x.

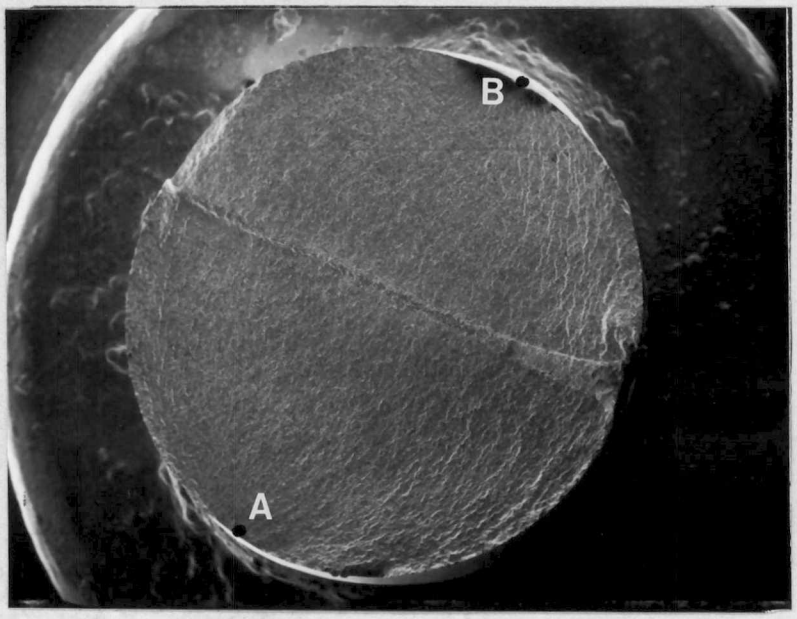

Figure 28. Macroscopic appearance of a decarburized fatigue specimen, tested at 57.1 ksi (394 MPa) (90% of the Y.P. and 58% of the U.T.S.) in bending. The specimen failed after 1.082×10^5 cycles. Points A and B are crack initiation sites and there are no ratchet marks visible. SEM 12x.

Ratchet marks (steps on the fracture surface where cracks on different planes join) were observed at most stress levels at 30x with an optical microscope. Typical ratchet marks are indicated in Figures 23, 24, 26, 27. A few more ratchet marks were observed on the specimens tested at higher stress levels while at low stress levels (just above the fatigue limit) only one, or possibly no ratchet marks could be seen (Figures 25 and 28).

One may expect more ratchet marks on the decarburized specimens if the critical stress for crack initiation is lower than for the non-decarburized specimens. If the critical stress is lower, more cracks will initiate over a larger area of the decarburized specimen surface, at the same applied stress as the non-decarburized specimens. There were slightly more ratchet marks, in total, on the decarburized specimens than on the non-decarburized specimens, although no quantitative trend could be established because of the small number of specimens tested.

The appearance of the fractured specimens in torsional loading was quite different from that observed for bending loading. Fracture surfaces of the non-decarburized and decarburized fatigue specimens are illustrated in Figures 29 to 35. The most notable feature of the fatigue fracture surfaces in torsion was cracking on planes near 45^{o} to the specimen axis and on planes parallel to the specimen axis. This is in contrast to specimens tested in bending which failed along planes normal to the specimen axis. Fatigue cracks on planes at 45^{o} to the specimen axis would be consistent with the observation that fatigue cracks propagate in Stage II on planes of maximum normal stress (16).

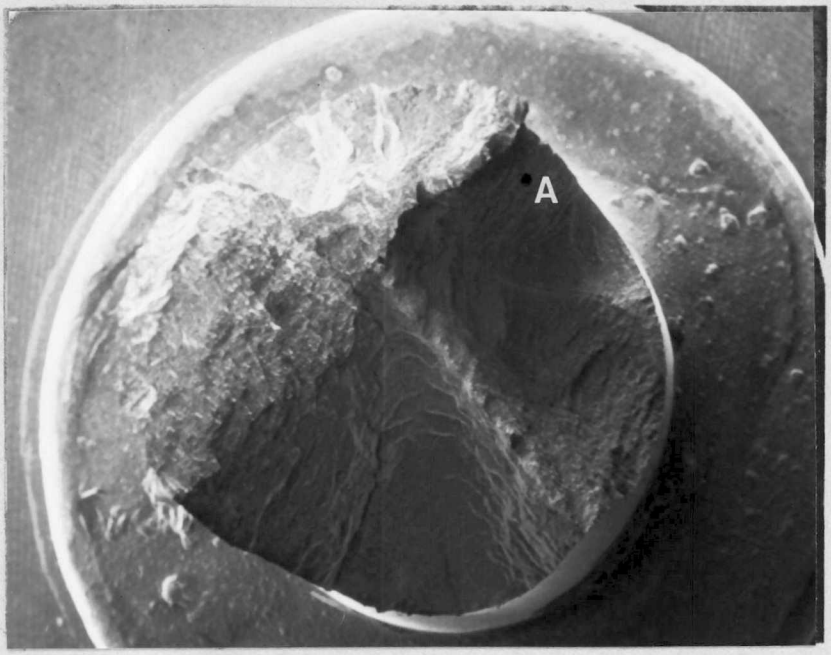

(a) Untilted

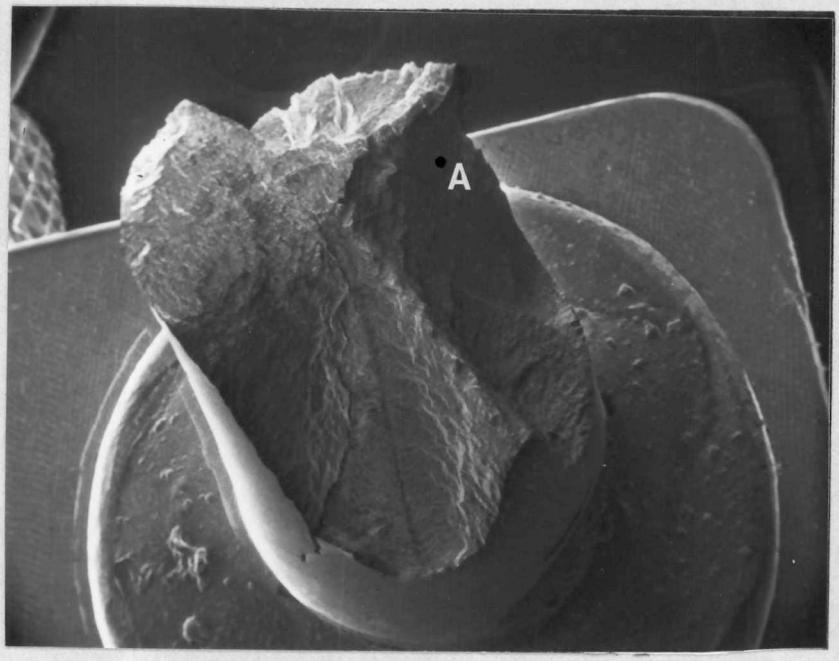

(b) Tilted

Figure 29. Macroscopic appearance of a non-decarburized fatigue specimen, tested at 70.1 ksi (483 MPa) (207% of the Y.P. and 140% of the U.T.S.) in torsion. The specimen failed after 3.15×10^4 cycles. Point A is on a plane approximately longitudinal to the specimen axis. SEM 10x.

(c) Longitudinal Cracks

Figure 29. (continued)

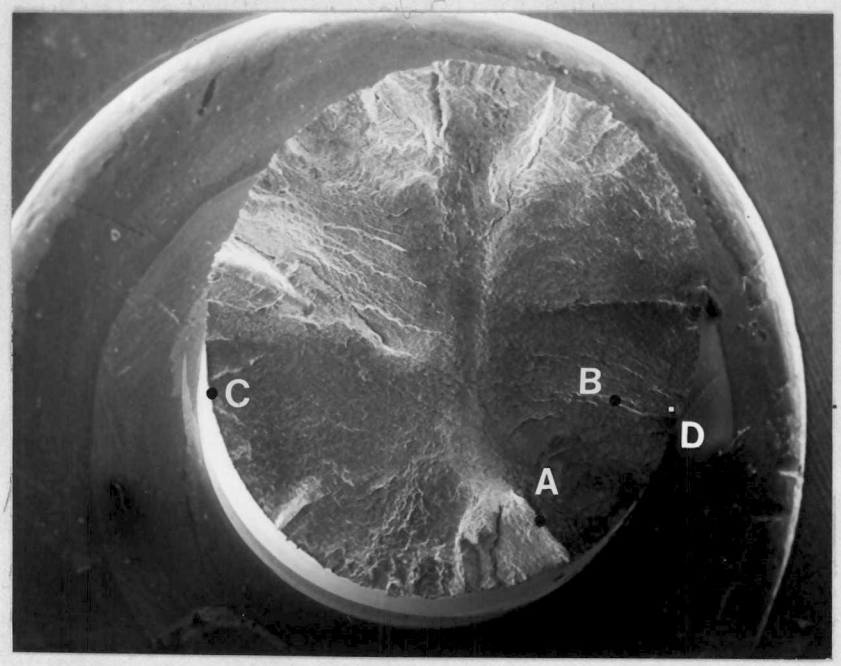

(a) Untilted

(b) Tilted

Figure 30. Macroscopic appearance of a non-decarburized fatigue specimen, tested at 54.2 ksi (374 MPa) (160% of the Y.P. and 108% of the U.T.S.) in torsion. The specimen failed after 1.154×10^5 cycles. Point A is on a longitudinal plane. Point B is a ratchet mark. Points C and D are crack initiation sites. SEM 12x.

(a) Untilted

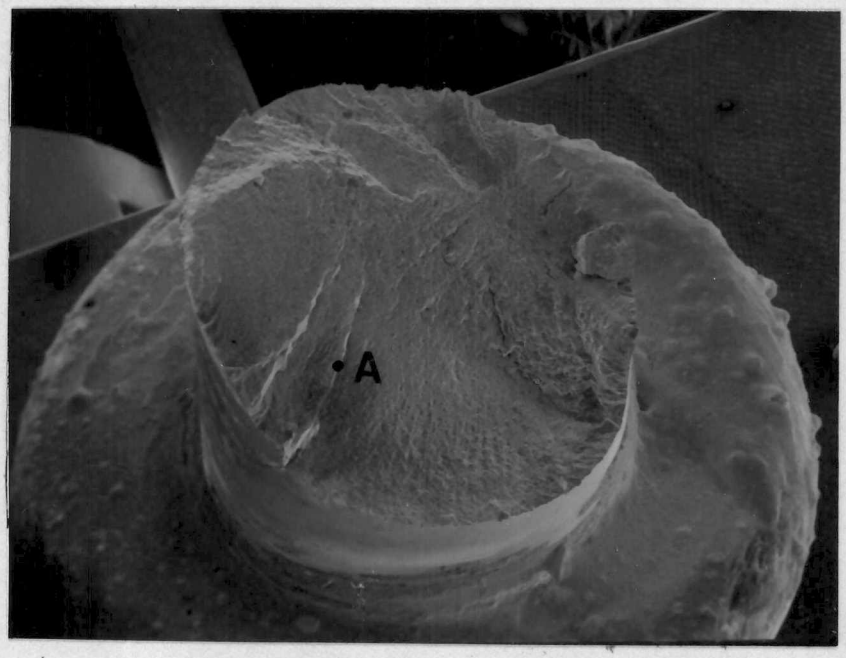

(b) Tilted

Figure 31. Macroscopic appearance of a non-decarburized fatigue specimen, tested at 41.4 ksi (285 MPa) (122% of the Y.P. and 83% of the U.T.S.) in torsion. The specimen failed after 3.131×10^5 cycles. Point A is a ratchet mark. SEM 12x.

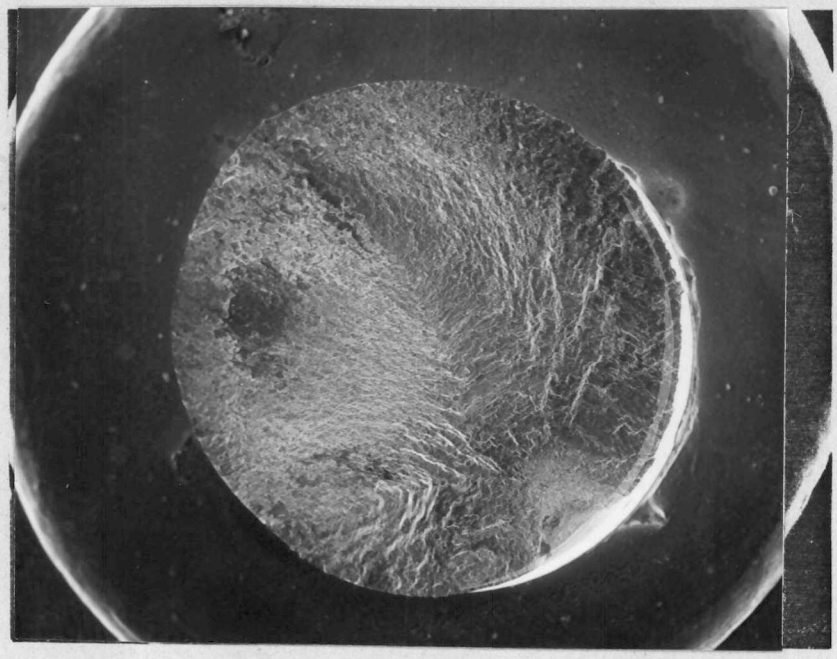

(a) Untilted

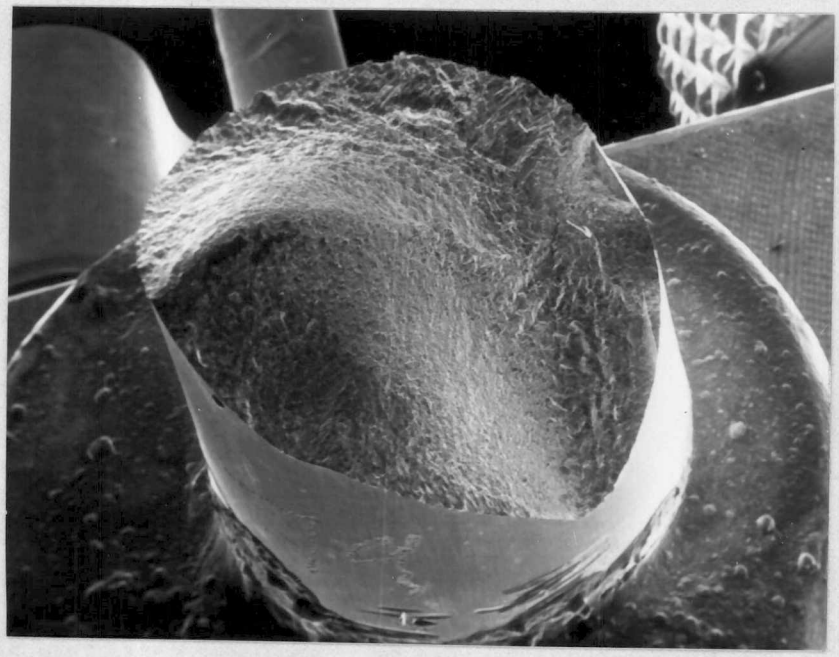

(b) Tilted

Figure 32. Macroscopic appearance of a non-decarburized fatigue specimen, tested at 28.7 ksi (198 MPa) (85% of the Y.P. and 57% of the U.T.S.) in torsion. The specimen failed after 4.1197×10^6 cycles. SEM 12x.

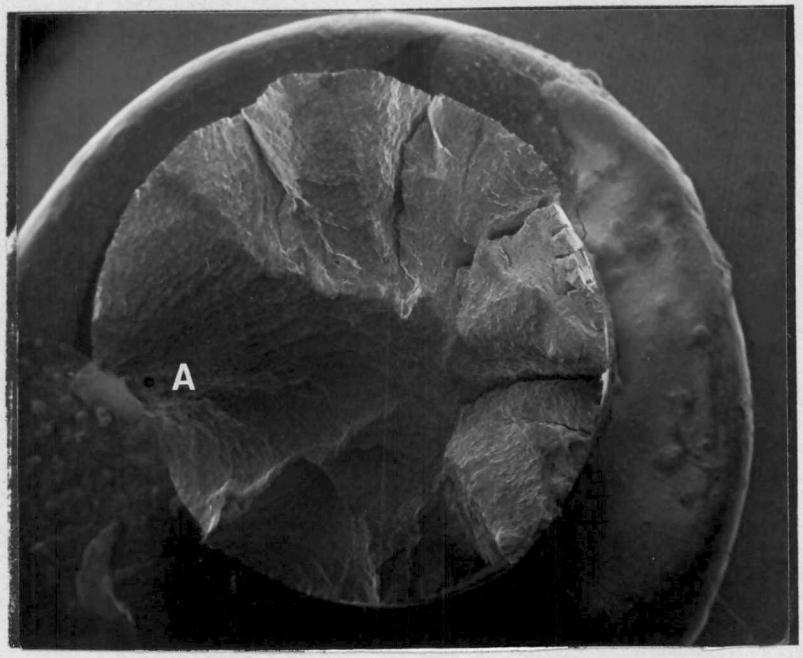

(a) Untilted

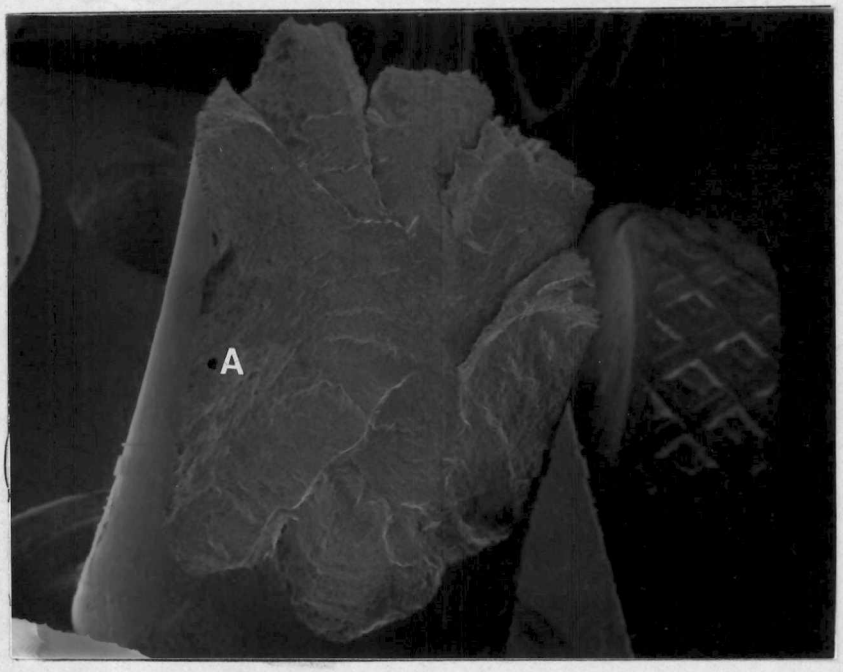

(b) Tilted

Figure 33. Macroscopic appearance of a decarburized fatigue specimen, tested at 53.7 ksi (370 MPa) (169% of the Y.P. and 110% of the U.T.S.) in torsion. The specimen failed after 4.54×10^4 cycles. Point A is on a longitudinal plane. SEM 10x.

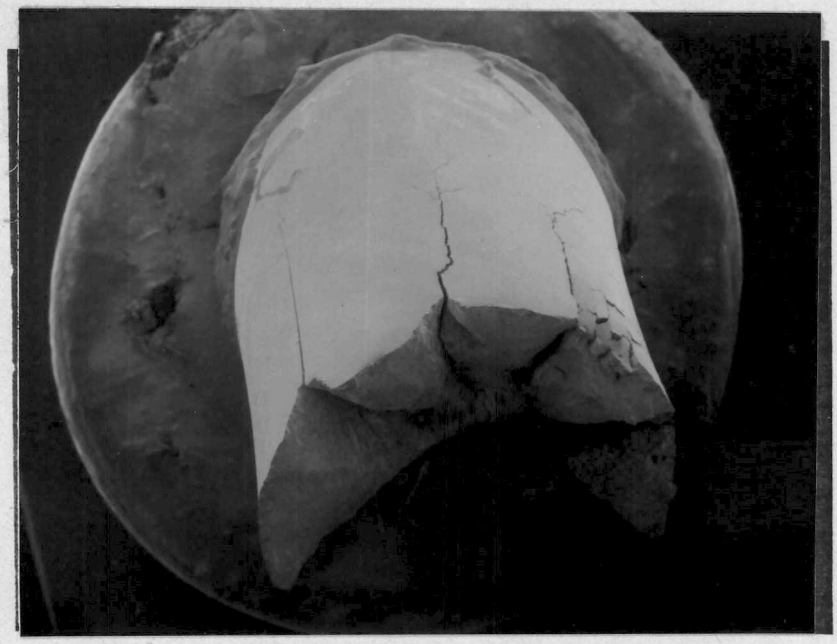

(c) Longitudinal Cracks

Figure 33. (continued)

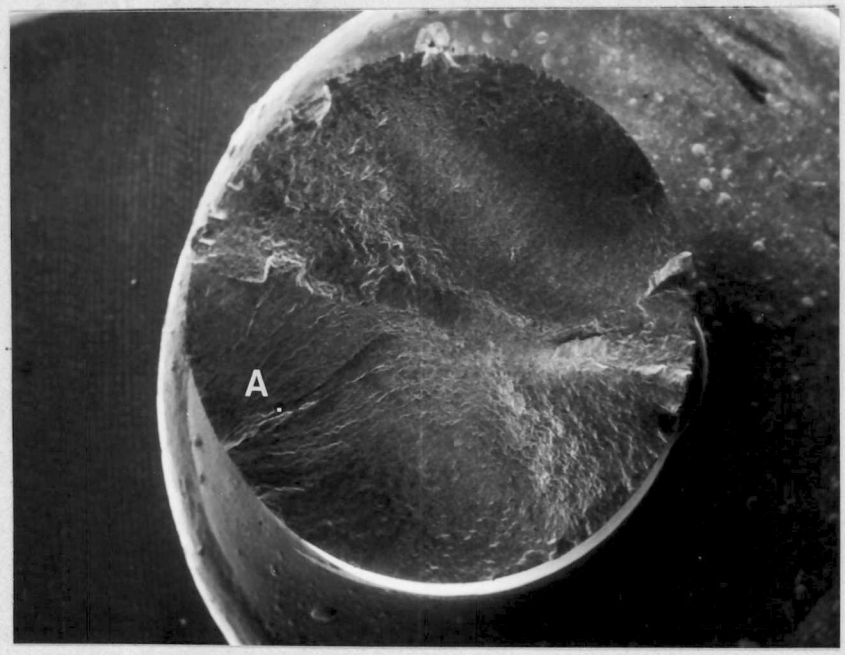

(a) Untilted

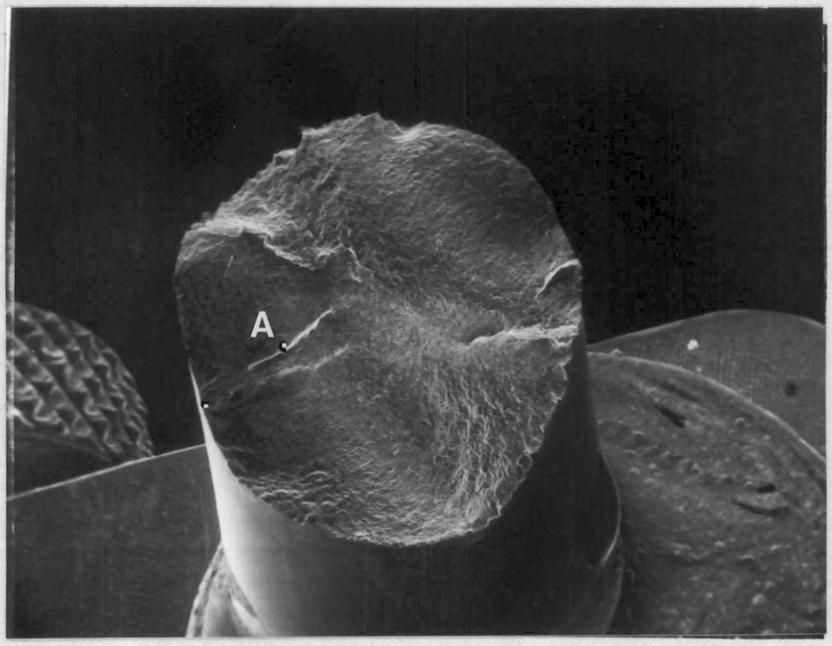

(b) Tilted

Figure 34. Macroscopic appearance of a decarburized fatigue specimen, tested at 31.6 ksi (218 MPa) (100% of the Y.P. and 64% of the U.T.S.) in torsion. The specimen failed after 6.256×10^5 cycles. Point A is a ratchet mark. SEM 10x.

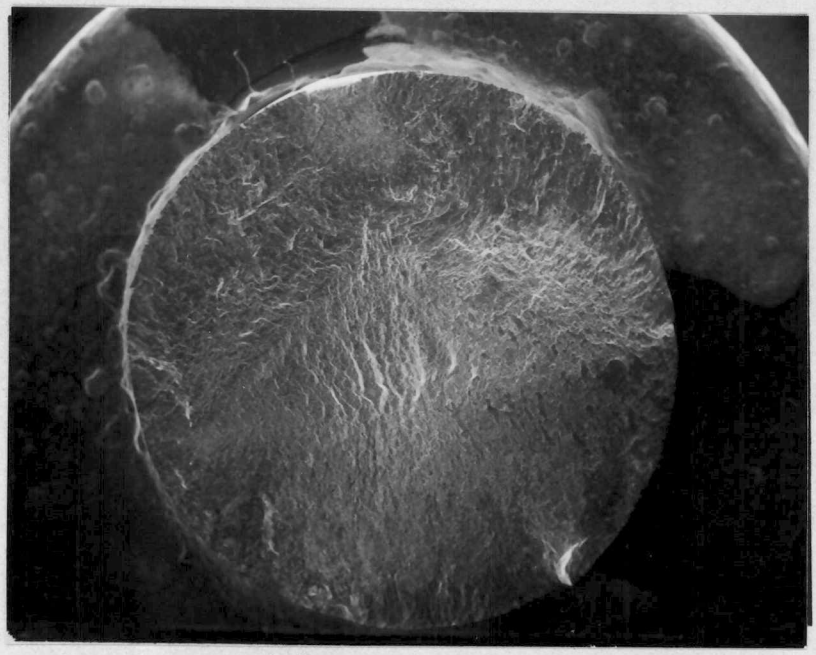

(a) Untilted

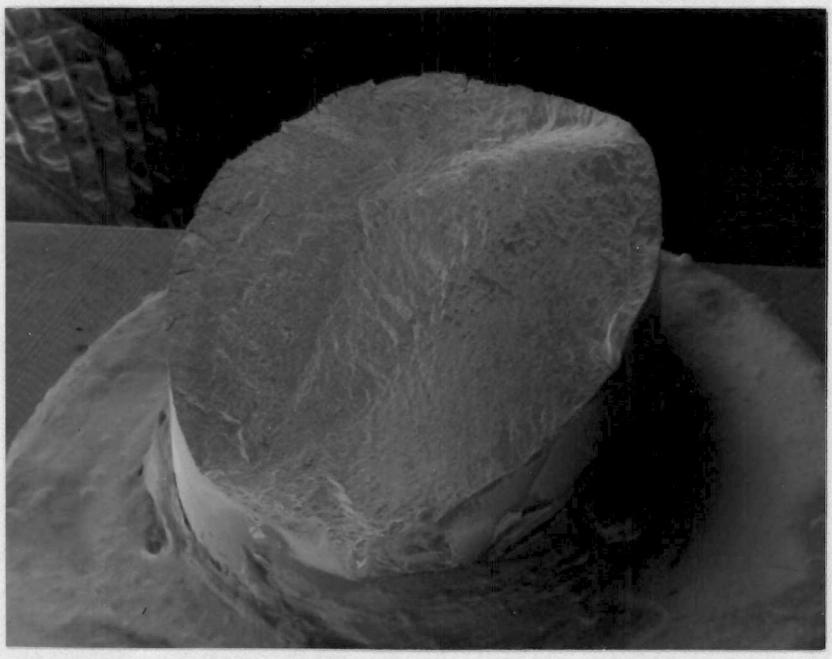

(b) Tilted

Figure 35. Macroscopic appearance of a decarburized fatigue specimen, tested at 25.3 ksi (174 MPa) (80% of the Y.P. and 52% of the U.T.S.) in torsion. The specimen failed after 8.62×10^5 cycles. SEM 12x.

At high stresses (generally above a reversed torsion stress of 50 ksi (345 MPa) which is about 150% of the equivalent upper yield point and 100% of the equivalent ultimate tensile strength based on Equation 10), there was additional cracking on planes parallel to the specimen axis. This is shown in Figures 29 and 33. In Figure 30 there is longitudinal cracking, but the predominant fracture plane is at 45^{o} to the specimen axis. Figure 33 illustrates the change in fracture appearance observed as the initial stress is increased to very high values. Fracture occurs on many planes, and the incidence of cracking on longitudinal planes becomes a major feature of the fracture surface.

In torsion the same stress cycle is experienced by the specimen at all points on a circumference at the minimum cross-section. It was observed that when testing a specimen in torsion, the first cracks visible were always oriented at about 45^{o} to the specimen axis. At high stress levels multiple cracks are initiated, and then are joined by other cracks propagating in a shear mode on longitudinal planes. It may be that the critical stress intensity factor for crack propagation in both the shear mode and the crack-opening mode is exceeded at the higher stress levels tested.

At torsional stress levels below 50 ksi (345 MPa), the dominant macroscopic fracture planes were roughly 45^{o} to the specimen axis (Figures 31, 32, 34, and 35).

At intermediate stress levels, best illustrated by Figures 30 and 34, there were two propagating crack fronts, initiated on opposite sides of the specimen. The specimens tested at intermediate stress levels also exhibited ratchet marks (Figures 30, 31, and 34), although

no difference could be discerned between the decarburized and non-decarburized specimens.

At stress levels just above the fatigue limit (Figures 32 and 35) the fracture surface contained no ratchet marks, and usually only one dominant crack front propagated across the specimen.

The acute angle between the specimen axis and the primary macroscopic fracture plane varied randomly from 30^{o} to 70^{o} on the specimens which contained no longitudinal fracture surface planes. Also on Figure 32, the propagating crack front appears to have changed planes after propagating half-way through the specimen. It is believed that both of the phenomena are related to the inability of the present fatigue machine to maintain the pure torsional stress after specimen stiffness is lost; that is, once a crack or cracks have propagated across more than half the specimen cross-section. When specimen stiffness is lost, the loading arm may wobble in an erratic fashion rather than move in an up-and-down motion which produces the torsional stress. When this happens, the specimen is near the end of its fatigue life.

In summary, the appearance of fracture surfaces produced by bending and torsion is different. The dominant propagating crack fronts appear to be on planes of maximum normal stress, which is normal to the specimen axis in bending, and 45^{o} to the specimen axis in torsion. There was evidence (ratchet marks and longitudinal cracks) of more propagating cracks at high stress levels than at low stress levels for both bending and torsion. There were few differences in appearance between decarburized and non-decarburized steels, although there is some evidence to indicate that there may be a few more propagating cracks in the decarburized specimens.

Microscopic Fractography

Crack path. The fatigue specimens were examined to determine the crack path through the constituents of the material. Metallographic specimens were prepared from the fatigue specimens by taking longitudinal sections of the fatigue specimens tested in bending and both longitudinal and transverse sections of the specimens tested in torsion. At least one specimen at each stress level was sectioned. The specimens were sectioned so that both the mid-point of the specimen and the crack initiation site were close to the metallographically prepared surface. These specimens were then examined at magnifications to 500X. Typical part-through cracks are illustrated in Figure 36.

In general, there were more part-through cracks observed at high stress levels than at low stress levels. At a reversed torsion stress greater than 65 ksi, or a reversed bending stress greater than 100 ksi, that is at stress levels approaching the static ultimate strength, there were a large number (greater than five) of part-through cracks along with roughening of the specimen surface due to plastic deformation (Figure 37). At lower stress levels and above the fatigue limits, a few (one to three) part-through cracks were observed in most specimens examined.

All of the part-through cracks observed were transgranular. That is, they extended through both ferrite grains and pearlite colonies. This is illustrated in the scanning electron micrograph shown in Figure 38. Because all of the observed part-through cracks were transgranular, one would expect pearlite to have an important influence on the fatigue

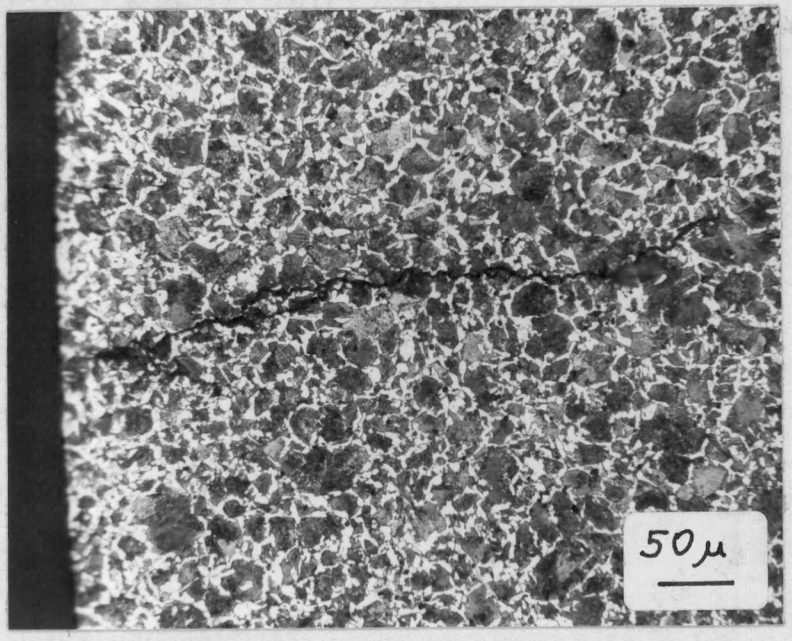

(a) Transverse Section

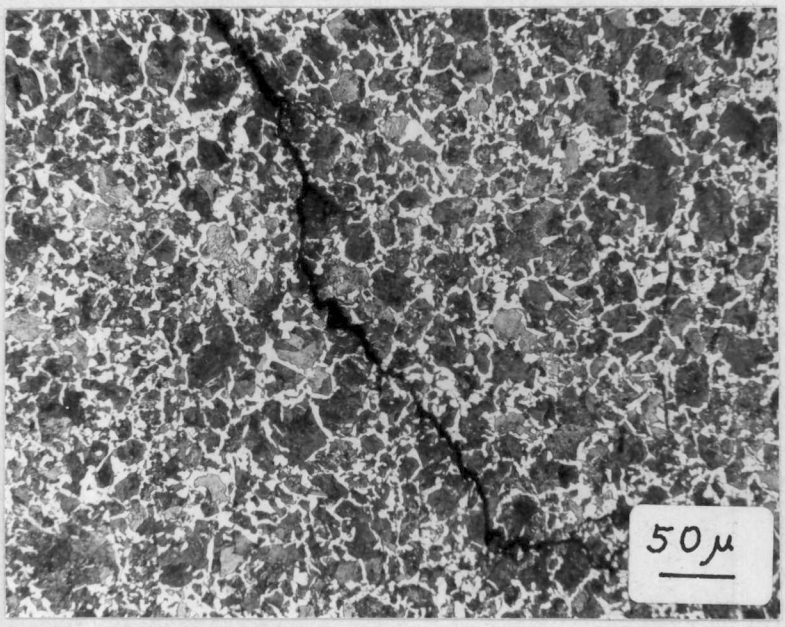

(b) Longitudinal Section

Figure 36. Typical part-through cracks. The specimen was non-decarburized and was tested in torsion at 54.2 ksi (374 MPa) (160% of the Y.P. and 108% of the U.T.S.). The specimen failed after 1.145×10^5 cycles. OM 200x.

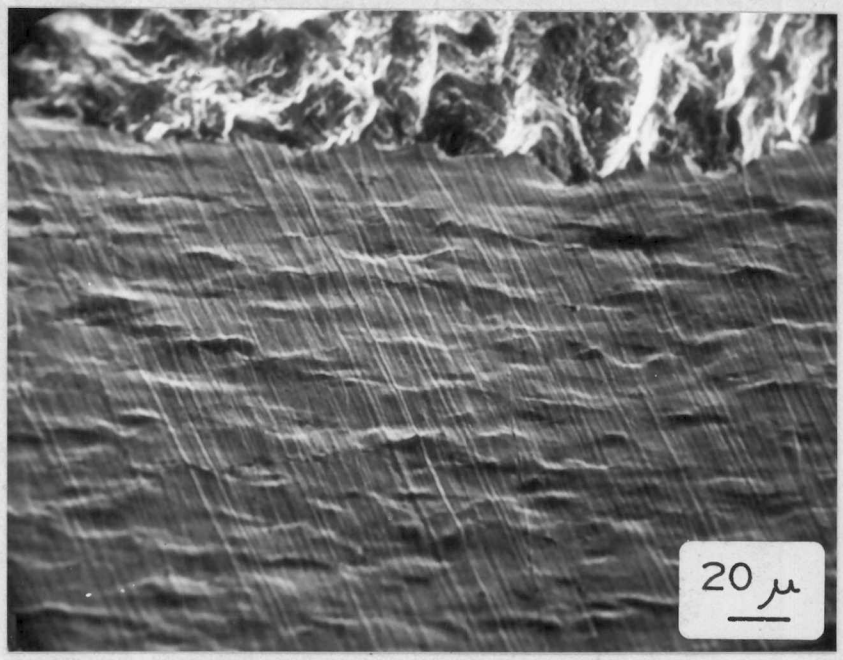

Figure 37. Roughening of the specimen surface due to plastic deformation. This specimen was decarburized and was tested at 107.2 ksi (739 MPa) (169% of the Y.P. and 109% of the U.T.S.). The specimen failed after 1.76 x 10^4 cycles. SEM 375x.

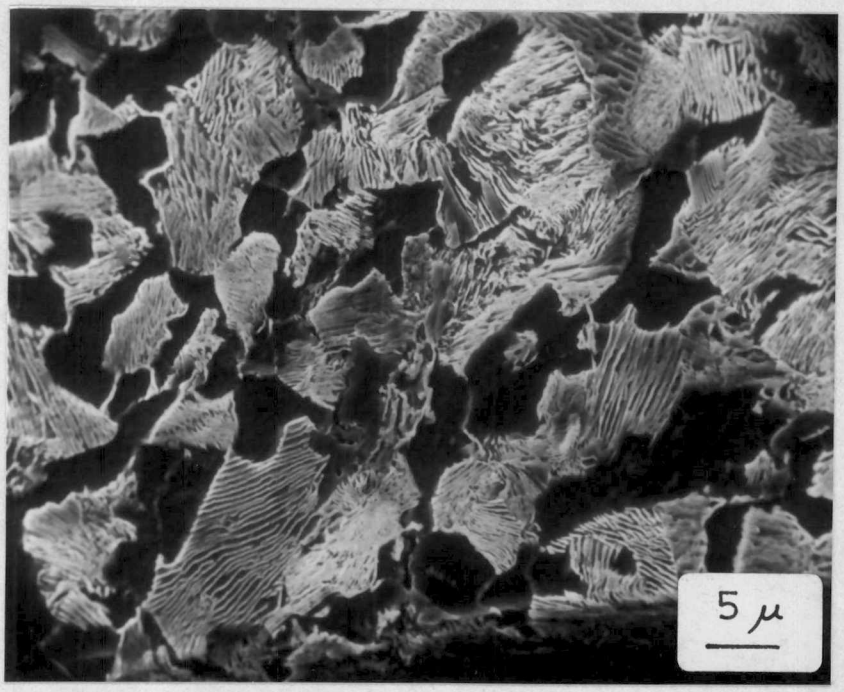

Figure 38. Typical crack path. This specimen was non-decarburized and was tested in bending at 108.9 ksi (751 MPa) (161% of the Y.P. and 109% of the U.T.S.). The specimen failed after 2.13 x 10^4 cycles. SEM 1800x.

properties of the specimens and on the microscopic appearance of the fatigue fracture surfaces.

Microfractography. Identification of microscopic features of fatigue failure (e.g., striations) is not a simple task in the material used in this study. (It should be pointed out that discussions of the appearance of fatigue striations commonly utilize photographs retrieved from such materials as low volume fraction second phase aluminum alloys where the striations are well developed and where there are no similarly appearing features not due to fatigue on the fracture surface). Fatigue striations bear a strong resemblance to pearlite on the fracture surface, and the extent to which branching occurs is one of the few methods available to distinguish the two sets of ridges. Calculations indicate that in this work, the fatigue striation spacing is on the same order of magnitude as the pearlite colony spacing. Metallographic observations indicate a microstructure that is 66% pearlite and 33% ferrite. If striations are present on the fracture surface, they will be present in the ferrite which normally comprises only one third of the fracture surface and which is embedded in two-thirds of the area containing similar appearing pearlite colonies. Branching of striations is minimal, while pearlite can be more extensively branched. The presence of one or two branched ridges in a small area of the specimen is neither conclusive evidence for the presence of pearlite or striations. Presumably, identification of striations should be easier near the surface of the decarburized specimens where the fraction of pearlite is minimized. Unfortunately, these are the most extensively rubbed areas. To further complicate matters, small unopened longitudinal cracks (secondary cracks)

are sometimes difficult to distinguish from striations and pearlite. Nevertheless, Figures 39 to 45 are included to show the typical appearance of fracture surfaces. It was concluded, based on examination, that striations were present in specimens loaded in both bending and in torsion. Additionally, there was more microscopic size transverse cracking at higher stress levels for both states of stress.

Discussion

Differences in fatigue behavior of the decarburized steel and non-decarburized steel, and the differences in bending and torsional loading may be discussed in terms of fatigue processes. (The effects of variables other than decarburization and increase in ferrite grain size are considered negligible.) It is useful to divide this discussion into a discussion of the fatigue strength and the fatigue limit. At the fatigue limit, either a crack does not initiate, or the specimen is loaded below some critical stress or stress intensity factor for crack propagation.

Fatigue limit. The reduction of the fatigue limit for the decarburized specimens was significant (25% and 30%) in bending and torsional loading. The microstructural differences between decarburized and non-decarburized specimens are the lack of pearlite and the increase in the ferrite grain size near the decarburized surface.

The fatigue limit will depend on whether there is some critical stress level available which allows the crack to initiate. It has been shown (17, 18, 19) that in hypoeutectoid steels, fatigue cracks initiate in ferrite grains. The strength of ferrite near the fatigue

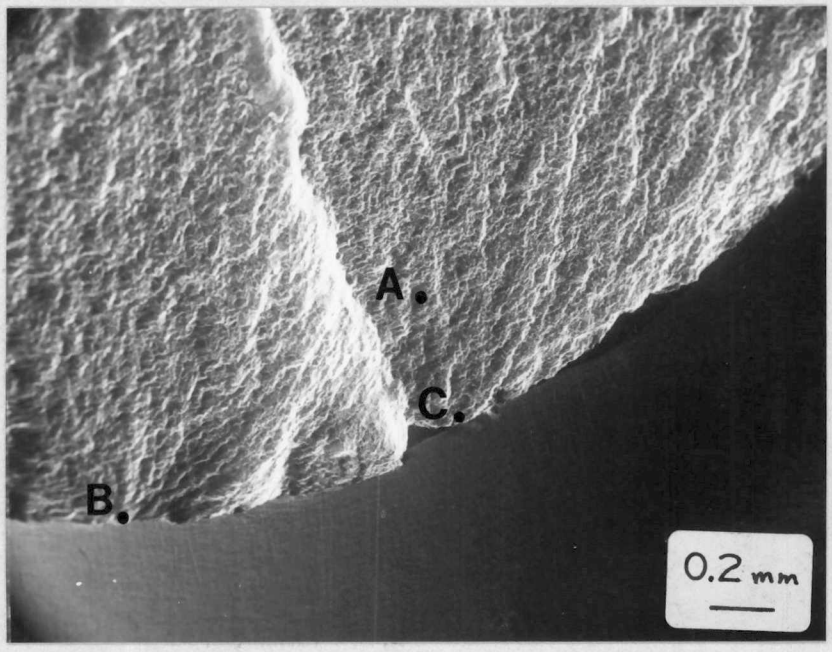

Figure 39. Fracture surface at low magnification. The specimen is decarburized and was tested in bending at 57.1 ksi (394 MPa) (90% of the Y.P. and 58% of the U.T.S.). The specimen failed after 1.161×10^5 cycles. Points B and C are crack initiation sites. Point A is 0.016 inch (0.4 mm) from the specimen surface. SEM 40x.

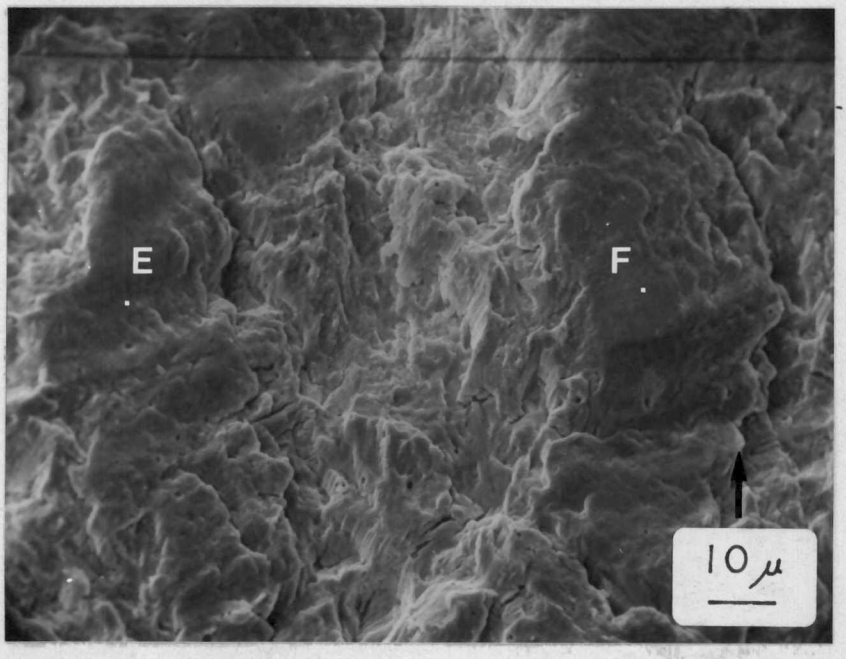

Figure 40. Fracture surface at point A of Figure 39. Points E and F are in rubbed areas. SEM 850x.

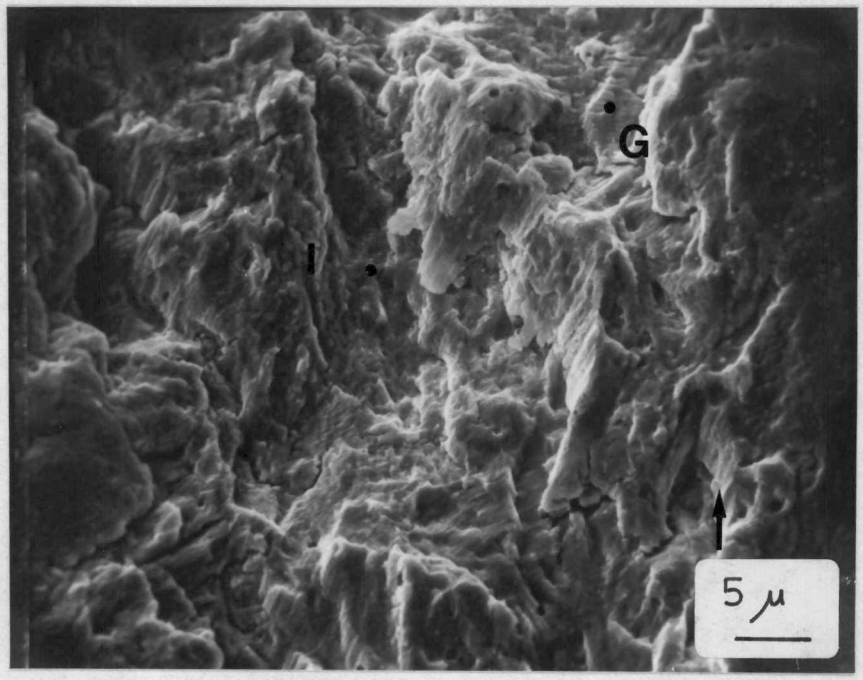

(a) 1800x.

Figure 41. Fracture surface at high magnification at Point A in Figure 39. Areas G and I show ridge lines. There is more branching in G than in I, implying that G is more likely to be a pearlite colony while I is more likely to be a region of striations. SEM.

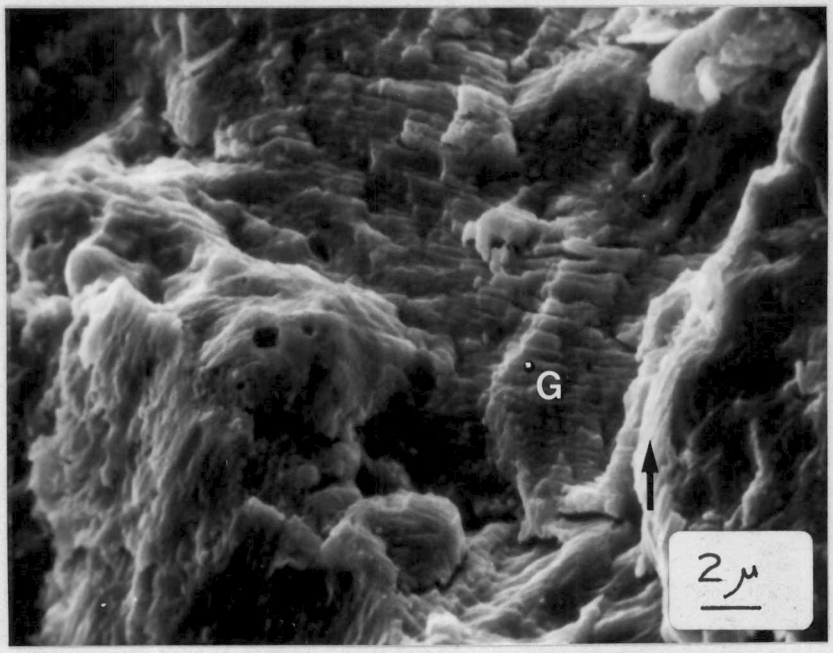

(b) Enlargement of Point G. 4250x.

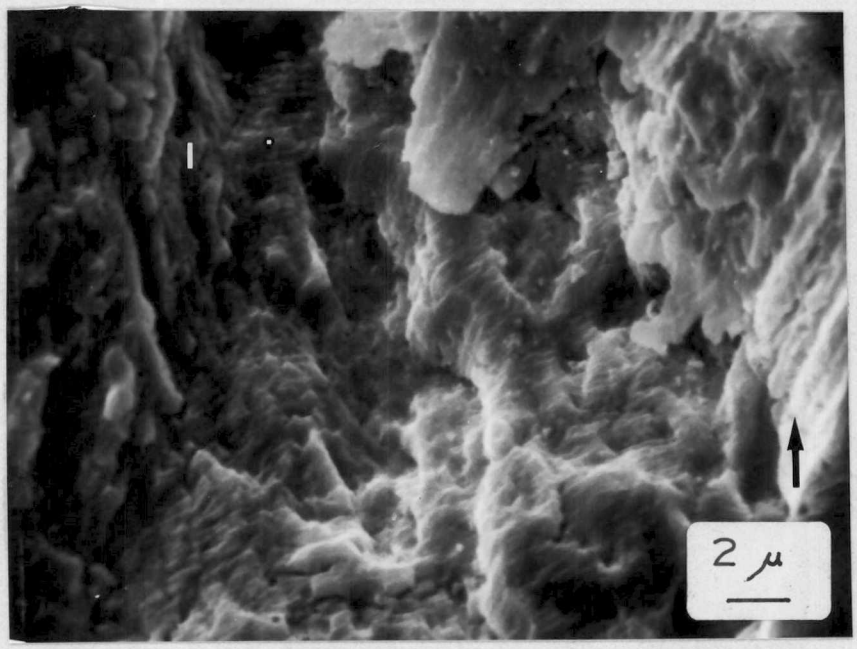

(c) Enlargement of Point I. 4250x.

Figure 41. (continued)

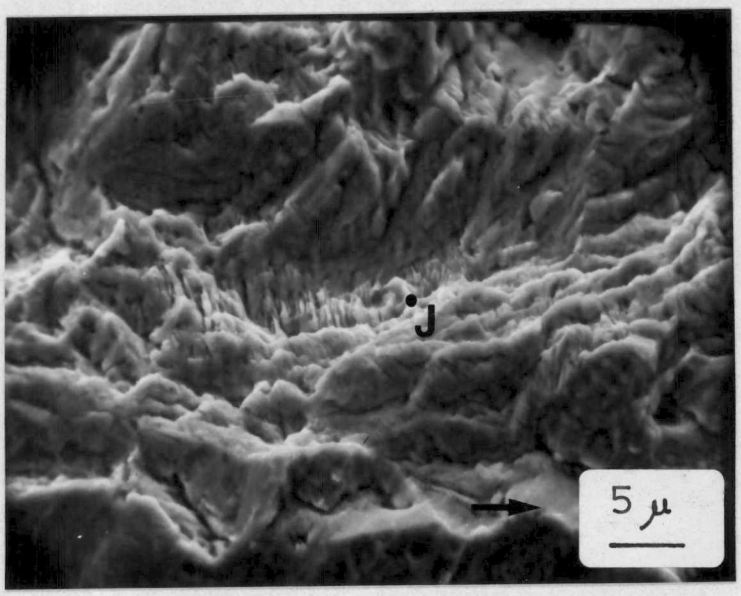

Figure 42. Fracture surface of a point 0.04 inch (1 mm) from the specimen surface. The specimen was decarburized and was tested in bending at 42.9 ksi (296 MPa) (68% of the Y.P. and 44% of the U.T.S.). The specimen failed after 4.865×10^5 cycles. Point J is probably pearlite. No fatigue striations were resolved. SEM 1800x.

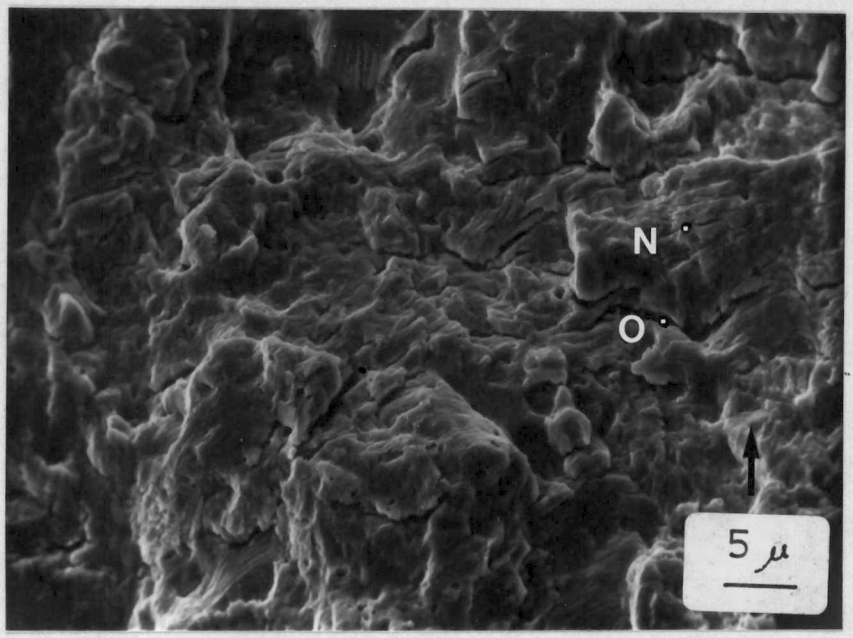

(a) 1800x.

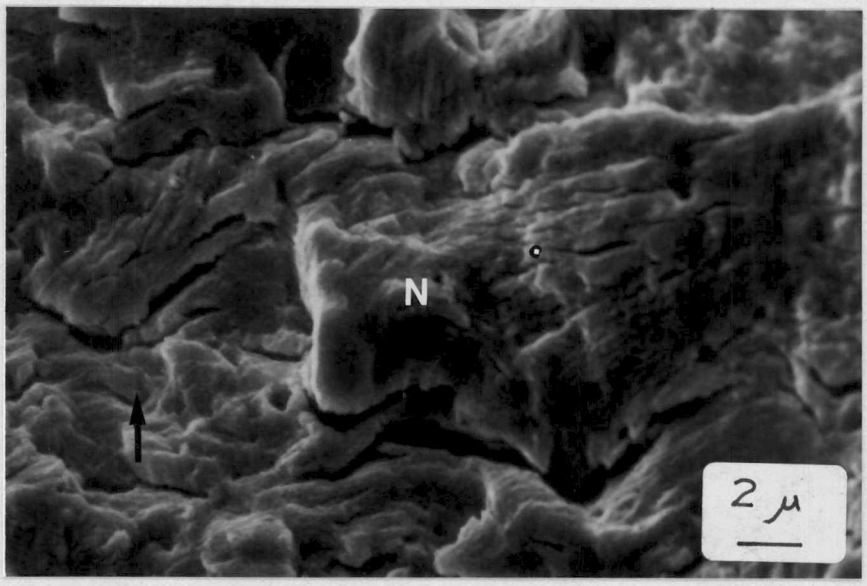

(b) Enlargement of Point N. 3600x.

Figure 43. Fracture surface at 0.07 inch (1.8 mm) from the specimen surface. The specimen is the same as in Figure 39. Region N shows small secondary cracking while Region O shows a larger secondary crack. SEM.

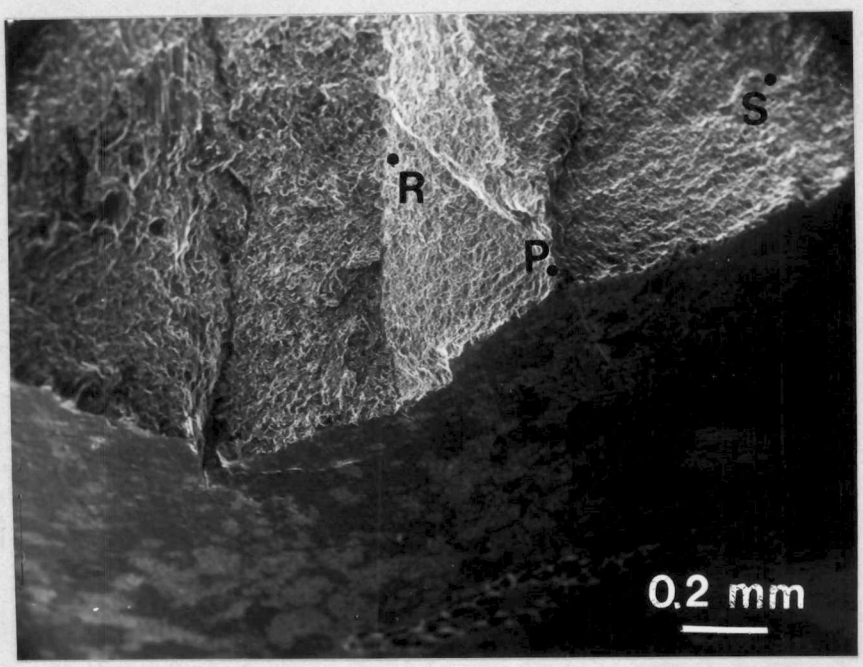

Figure 44. Fracture surface of a decarburized fatigue specimen tested in torsion at 37.9 ksi (261 MPa) (120% of the Y.P. and 77% of the U.T.S.) for 1.218×10^5 cycles. Points P to R and points P to S delineate the area of fatigue crack propagation. SEM 45x.

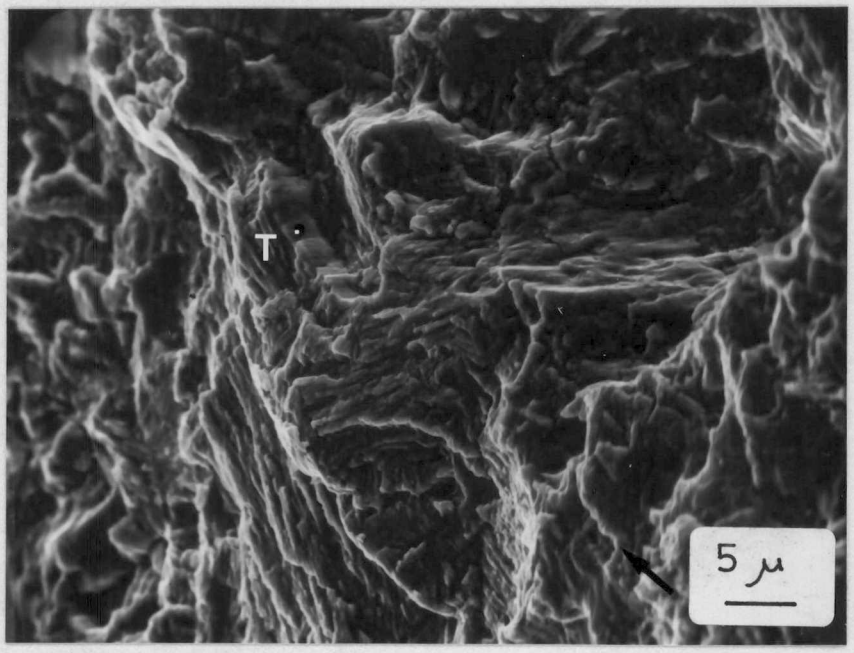

(a) 1800x.

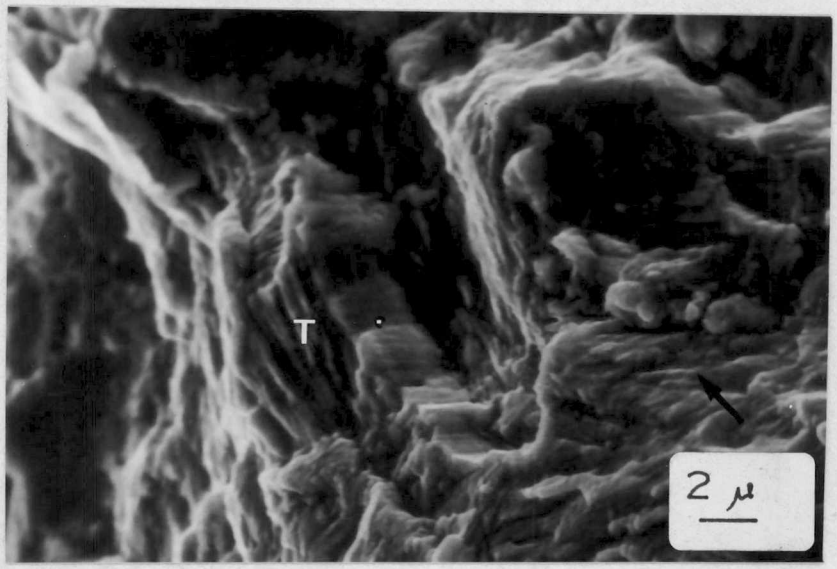

(b) Enlargement of Point T. 3600x.

Figure 45. Fracture surface at point R in Figure 44, which is 0.02 inch (0.5 mm) from the specimen surface. There is a small patch of striations at point T. SEM.

limit depends on a critical stress to move dislocations and form persistent slip bands. The ferrite may have a slightly different composition in the decarburized layer due to the different heat treatment and the diffusion of other solute elements besides carbon into, or out of, the steel. This change in composition could raise, or lower, the fatigue limit of the decarburized steel depending on whether the ferrite became harder or softer. The grain size of the ferrite is larger in the decarburized layer and this effect by itself would be expected to cause the decarburized steel to have a lower fatigue limit (by 5-10%, as discussed on page 59) than the non-decarburized steel. The effect of the larger ferrite grain size does not account for the total decrease in the fatigue limits. Another effect involved is the constraining effect of the adjoining hard constituent (pearlite) in the non-decarburized specimens, which would tend to raise the strength of the ferrite.

One other possible cause for the difference in the fatigue limit between the decarburized and non-decarburized specimens is that the stress or stress intensity factor below the fatigue limit is too low for Stage I or Stage II crack propagation. A second possible cause of the difference is that the pearlite constituent in the non-decarburized specimens may block the advance of a microcrack and cause a higher fatigue limit in the non-decarburized steel. These two cases are less probable because they call for the existence of macroscopic part-through cracks in the specimens tested below the fatigue limit. This condition was not found in the fatigue specimens on metallographic examination.

All these explanations for the differences in the fatigue limit in the decarburized and non-decarburized steels are possible and would be consistent with the equivalent stress failure criteria.

The fatigue limit is predicted fairly well by a failure criterion based on an equivalent stress (either maximum shear stress or octahedral shear stress), for both the decarburized and non-decarburized steels.

Crack nucleus size. It is possible using Rahka's equation (20) (Equation 5), which relates crack nucleus size to the tensile stress range, to roughly estimate the size of the region in which Stage I crack propagation occurred in the specimens tested in the present study. The size of the crack nucleus at 50 ksi (345 MPa) is predicted to be 0.0027 inch (0.069 mm) and at 75 ksi (524 MPa) it is 0.0004 inch (0.011 mm). If this approximation is too small by a factor of 2, then the nucleus size would be 0.005 inch (0.13 mm). This nucleus size, 0.005 inch (0.13 mm), is one-eighth the total depth of decarburization, 0.042 inch (1.07 mm). This estimated crack nucleus size is also on the same order of magnitude as the mean grain diameter, about 0.01 inch (0.022 mm) reported in Table III, page 55.

In the present study, Stage II propagation is the dominant stage (greater than 80% of the fatigue life, discussed on page 73) of the fatigue life of the specimens. It is therefore appropriate to consider the effects of decarburization of the fatigue properties in terms of Stage II crack propagation of stress levels above the fatigue limit.

Fatigue strength. There is a difference in fatigue strength between the decarburized and non-decarburized specimens. The non-decarburized steel has a higher fatigue strength in both bending and torsion. The number of cycles for crack initiation may be less for the decarburized specimens because the ferrite layer has a lower strength as discussed previously. But, a more significant effect may be that the crack propagation rate in Stage II is greater in the decarburized layer because of the lowered pearlite content (as found by Aita and Weertman (15)). Both of these effects tend to lower the fatigue strength for the decarburized steel.

There are also differences between bending and torsion which do not allow the fatigue strength in combined stress to be predicted by a failure criterion based on equivalent stress. This is due to the differences in the macroscopic cracking process in the bending mode versus the torsion mode. In the torsion specimens, the fracture surface is at 45^{o} to the specimen axis and there may be longitudinal cracks present. In these cases the total area of the fracture surface is greater than in the bending specimens. Any cracks would have to propagate a longer distance to cause failure and this would tend to cause longer fatigue lives for the torsion specimens. This was observed. Also, for the torsion specimens, there is the possibility of many cracks initiating around the circumference of the specimen instead of just two major cracks as in the bending specimens. At the same stress level, the stress intensity factor will be less for the case with adjacent cracks versus the case with only one crack present. If the stress intensity factor is lower, the fatigue life will be

longer (or the fatigue strength higher), in the torsion specimens which contain multiple cracks. Another factor which would effect the fatigue strength is the stiffness to crack length relation which determines the actual applied load in a specimen with a part-through crack. This stiffness to crack length relation is most probably different in the torsion specimens and may tend to produce longer fatigue lives in torsion.

Summary

In summary, an equivalent stress concept may be used to compare bending loading to torsion loading at the fatigue limit for both decarburized and non-decarburized steels. Both the maximum shear stress and octahedral shear stress criteria predict the allowable stress reasonably well. Experimental data points lie between the lower value predicted by the maximum shear stress and the higher octahedral shear stress.

The use of an equivalent stress concept to predict allowable torsion stresses based on bending data, or vice-versa, becomes increasingly inaccurate as the failure stress increases above the fatigue limit. Observed failure stresses lie above predicted stresses by significant amounts for both decarburized and non-decarburized material.

Use of an equivalent stress concept is based on the assumption that fatigue cracks are initiated by slip events whose onset can be predicted by an equivalent (shear) stress. At the fatigue limit no crack can form unless the stress is high enough to initiate persistent slip so a reasonable correlation between predicted and observed fatigue stresses is expected, and was observed.

Above the fatigue limit two factors must be considered. The equivalent stress concept does not consider crack propagation, and yet crack propagation is a dominant fraction of the total life. This might imply that as the applied stress was increased, so that the fraction of life due to crack propagation was decreased, the equivalent stress used to predict the initiation event would better predict the allowable stress. However, if loading is above the yield stress, plastic deformation occurs during the loading cycle. Yet the stress plotted on the ordinate of the experimental S-N curves is calculated on the assumption that loading is elastic. These stresses are therefore too high.

To determine whether an equivalent stress concept which predicts stresses required for an initiation event can be used to predict allowable loads when the life is controlled largely by crack propagation, it is necessary to examine differences in the observed and predicted fatigue strengths below the stress for yield. In this study, the observed yield strength was about 65 ksi which should be the same as the yield strength in bending the equivalent yield in torsion should then be about 32.5 ksi. The observed endurance limits were about 47 and 36 ksi in bending and 27 and 19 ksi in torsion. Consequently the data do not permit the evaluation of the prediction capability of the equivalent stress crack initiation model above the fatigue limit but below the yield stress since the S-N curves are relatively flat in this region. To test the validity, the material would have to have a sufficiently high yield stress that the S-N curve still showed a significant decrease in stress with an increase in life between yield stress loading and fatigue limit loading.

CHAPTER IV

CONCLUSIONS AND FUTURE WORK

Conclusions

1. Tensile tests revealed a slight decrease (6%) in the upper yield point and no significant difference in ultimate tensile strength or elongation at fracture for decarburized specimens.

2. The fatigue strengths and the fatigue limit are generally lower for decarburized steel compared to non-decarburized steel used in the present study. The fatigue limits were reduced by 25% and 30% in bending and torsion. The fatigue strengths were reduced by lesser amounts at a lower number of cycles to failure. In bending, the difference in fatigue strength was not significant below 13,000 cycles to failure where the difference is only 6%.

3. The fatigue strength (or fatigue life) above the fatigue limit depends in part on crack initiation and in part on crack propagation. The number of cycles in crack propagation was estimated to be 80% of the fatigue life of the specimens in the present study.

4. The fatigue limits at 10^7 cycles of both decarburized and non-decarburized steels under biaxial loading can be estimated by the maximum shear stress criterion or the octahedral shear stress criterion. This is true because crack initiation and/or Stage I crack propagation determine the fatigue limit, and these processes are near-surface events dependent on a critical shear stress value.

5. The fatigue strengths at lower than 10^6 cycles can not be described by a maximum shear stress or octahedral shear stress criterion.

Here the fatigue life is dominated by Stage II crack propagation which is not simply related to the initial applied stress.

6. Macroscopic fractography revealed significant differences between bending and torsion. In bending, macroscopic cracking occurred only on planes normal to the specimen axis. In torsion, fracture planes were observed at both 45^{o} to the axis and parallel to the axis. At high stress levels (i.e., approximately the U.T.S.), the incidence of cracking parallel to the axis increased.

7. There was macroscopic evidence (i.e., ratchet marks, longitudinal cracks) of there being more propagating cracks present in specimens tested at higher stress levels.

8. Microscopic fractography showed striations in bending and torsion. However, identification of characteristic features associated with fatigue failure was complicated by the large volume fraction of the similarly appearing pearlite microstructural constituent.

Future Work

1. Decarburization should be done in a non-scaling atmosphere, such as wet hydrogen, to eliminate steps in the present specimen preparation procedure and to obtain free ferrite if desired.

2. It may be proper to use biaxial failure criteria based on plastic strain range instead of stress at low cycles. A study investigating this model would be most appropriate.

3. The fatigue processes in decarburized steels may be better characterized by using cyclic stress ratios greater than zero. By eliminating rubbing of the fracture surface, fractographic examination

is made much easier. The region and extent of Stage I microcrack propagation may be determined, and pearlite and fatigue striation morphology in the decarburized zone may be studied.

LIST OF REFERENCES

LIST OF REFERENCES

1. Bales, D.A., "A Study of Decarburization in SAE 1042 Steel: Its Effect on Fatigue Life, Tensile Properties, and Fatigue Fractography." Master's Thesis, The University of Tennessee, Knoxville, 1977.

2. Fine, M.E., "Fatigue Resistance of Metals," Metallurgical Transactions A, Vol. 11A, 1980, pp. 365-379.

3. ASTM, "Standard Definitions of Terms Relating to Fatigue Testing and the Statistical Analysis of Fatigue Data (E206-72)," Annual Book of ASTM Standards, pt. 10, American Society for Testing and Materials, Philadelphia, 1978, p. 359.

4. Andrew, J.H., and Richardson G.T., "An Investigation of Spring Steels," J. Iron and Steel Institute, Vol. 131, 1935, pp. 129-149.

5. Hankins, G.A., and Becker, M.L., "The Effect of Surface Conditions Produced by Heat Treatment on the Fatigue Resistance of Spring Steels," J. Iron and Steel Institute, Vol. 124, 1931, pp. 387-429.

6. Gill, E.T. and Goodacre, R., "Some Aspects of the Fatigue Properties of Patented Steel Wire," J. Iron and Steel Institute, Vol. 130, 1934, pp. 293-317.

7. Garwood, M.F., Zurburg, H.H., and Erikson, M.A., "Correlation of Laboratory Tests and Service Performance," Interpretation of Tests and Correlation with Service, American Society for Metals, Cleveland, 1951, pp. 19-22, 70-75.

8. Simkovich, E.A., and Loria, E.A., "Effect of Decarburization and Grinding Conditions on Fatigue Strength of 5% Cr-Mo-V Sheet Steel," Transactions of the ASM, Vol. 53, 1961, pp. 109-122.

9. Shah, J.B., "Failure Analyses of Aircraft Accidents - Part II" Metals Engineering Quarterly, Vol. 14, no. 4, 1974, pp. 23-29.

10. Gassner, R.H., "Decarburization and Its Evaluation by the Chord Method," Metal Progress, Vol. 113, no. 3, 1978, pp. 59-63.

11. Nauman, F.K., and Spies, F., "Decarburization," Case Histories in Failure Analysis, American Society for Metals, Metals Park, Ohio, 1979, pp. 247-254.

12. Riddihough, M., and DeBelin, G.A., Correspondence. J. Iron and Steel Institute, Vol. 124, 1931, pp. 445-449.

13. Swanson, S.R., Editor, Handbook of Fatigue Testing, ASTM STP 566, American Society for Testing and Materials, Philadelphia, 1974, pp. 44-45.

14. Rozorsky, E., Weiss, B. Z., and Niedzwiedz, S., "Fatigue Crack Propagation in a Si-Mn Steel Under Constant Deflection," Transaction of the ASM, Vol. 60, 1967, pp. 187-193.

15. Aita, C.R., and Weertman, J., "Effect of Microstructure on Fatigue Crack Propagation in Iron-Carbon Alloys," Metallurgical Transactions A, Vol. 10A, 1979, pp.535-544.

16. Dieter, G.E., Mechanical Metallurgy, 2nd edition, McGraw-Hill, New York, 1976, P. 414.

17. Kocanda, S., Fatigue Failure of Metals, Sijthoff and Noordhoff, Alphen ann deu Riju, the Netherlands, 1978, p. 85.

18. Luther, R.G., and Williams, T.R.G. "Fatigue Crack Initiation Processes in Mild Steel," Metal Science, Vol. 11, 1977, pp. 332-339.

19. Klesnil, M., Holzman, M., Lukas, P., and Rys, P., "Some Aspects of the Fatigue Process in Low-Carbon Steel," J. Iron and Steel Institute, Vol. 203, 1965, pp. 47-53.

20. Rahka, K., "On the Transition from Initiation to Propagation of Fatigue Cracks in Plain Steel Specimens," Fracture 1977, Vol. 2, Fourth International Conference on Fracture, Waterloo, Canada, June 19-24, 1977, Pergamon Press, New York, 1977, p.1,345-1,351.

21. Masada, C., Ohta, A., Nishijima, S., and Sasaki, E., "Fatigue Striation in a Wide Range of Crack Propagation Rates up to 70 μm/cycle in a Ductile Structural Steel," J. of Materials Science, Vol. 15, 1980, pp. 1663-1670.

22. Koterazawa, R., Mori, M., Matsui, T. and Shimo, D., "Fractographic Study of Fatigue Crack Propagation," J. of Engineering Materials and Technology, Vol. 95, no. 4, 1973, pp. 202-212.

23. Austin, C.R., "Effect of Surface Decarburization on Fatigue Properties of Steel," Metals and Alloys, Vol. 2, 1931, pp.117-119.

24. Burns, G., "The Properties of Some Silico-Manganese Steels," J. Iron and Steel Institute, Vol. 125, 1932, pp.363-384.

25. Hankins, G.A., Becker, M.L., and Mills H.R., "Further Experiments on the Effect of Surface Conditions on the Fatigue Resistance of Steels," J. Iron and Steel Institute, Vol. 133, 1936, pp. 339p - 425p.

26. Jackson, L.R., and Pochapsky, T.E., "The Effect of Composition on the Fatigue Strength of Decarburized Steel," Transactions of the ASM, Vol. 39, 1947, pp. 45-59.

27. Lipsitt, H.A., and Horne, G.T., "The Fatigue Behavior of Decarburized Steel," American Society for Testing Materials, Proceedings, Vol. 57, 1957, pp. 587-599.

28. Robinson, G.H., "The Effect of Surface Condition on the Fatigue Resistance of Hardened Steel," Fatigue Durability of Carburized Steel, American Society for Metals, Cleveland, 1957, pp. 11-22.

29. Speigler, B., Weiss, B.Z., and Taub, A., "Influence of Decarburization on the Fatigue Properties and the Propagation of Cracks in Silicon Steels," J. Iron and Steel Institute, Vol. 202, 1964, pp. 509-517.

30. Bron, D.I., Levites, I.I., and Pustovalov, V.I., "Effect of Tempering and Surface Condition on the Fatigue Strength of Steel 5552," Metal Science and Heat Treatment, no. 10, 1968 , pp. 834-835.

31. Funke, P., "Influence of Different Decarburization on the Fatigue Strength of Spring Steels," Stahl und Eisen, Vol.96, 1976, pp. 28-32.

32. Higdon, A., Ohlson, E.H., Stiles, W.B., Weese, J.A., and Riley, W.F., Mechanics of Materials, 3rd ed., John Wiley and Sons, New York, 1977, pp. 483-491.

33. Pope, J.A., Metal Fatigue, Chapman and Hall, London, 1959, pp. 24-54.

34. Sines, G., and Waisman, J.L., Metal Fatigue, McGraw-Hill, New York, 1959, pp. 145-169.

35. Gough, H.J., and Pollard, H.V., "The Strength of Metals under Combined Alternating Stresses," The Institute of Mechanical Engineers, Proceedings, Vol. 131, 1935, pp. 1-53.

36. Gough, H.J., and Pollard,H.V., "The Effect of Specimen Form on the Resistance of Metals to Combined Alternating Stresses," The Institute of Mechanical Engineers, Proceedings, Vol. 132, 1936, pp. 549-573.

37. Frost, N.E., Marsh, K.J., and Pock, L.P., Metal Fatigue, Clarendon Press, 1974, pp. 48-51, 76-80.

38. Morikawa, G.K., and Griffis, L., "The Biaxial Fatigue Strength of Low-Carbon Steels," The Welding Journal, Vol. 24, 1945, pp. 1,675-1,745.

39. Rotvel, F., "Biaxial Fatigue Tests with Zero Mean Stresses using Tubular Specimens," International Journal of Mechanical Science, Vol. 12, 1970, pp. 597-613.

40. Tanaka, K. and Matsuoka, S., "The Strength of JIS SNCM8 Steel Under Combined Alternating Stresses," Fracture 1977, Vol. 2., Fourth International Conference on Fracture, Waterloo, Canada, June 19-24, 1977, Pergamon Press, New York, 1977, pp. 1,161-1,168.

41. Havard, D.G., Williams, D.P., and Topper, T.H. "Biaxial Fatigue of Mild Steel: Data Compilation and Analysis," Third International Conference on Structural Mechanics in Reactor Technology, 1975, Vol. 5, no. L 6/2, 1975.

42. ASTM, "Standard Specification for Steel Bars, Carbon and Alloy, Hot-Rolled and Cold-Finished, General Requirements for (A29-76)," Annual Book of ASTM Standards, Pt. 5, American Society for testing and Materials, Philadelphia, 1978, pp. 1-10.

43. Snedecor, G.W., and Cochran, W.G., Statistical Methods, 6th ed., The Iowa State University Press, Ames, Iowa, 1967, pp. 381-418.

44. Houchard, R., STATPACK - Statistical Package, Western Michigan University Computer Center, 1974.

45. ASME, Surface Texture, (B46.1-1978), The American Society of Mechanical Engineers, New York, 1978.

46. ASTM, "Standard Hardness Conversion Tables for Metals (E140-78)," Annual Book of ASTM Standards, Pt. 10, American Society for Testing and Materials, Philadelphia, 1978, pp. 307-321.

47. ASTM, "Standard Methods of Tension Testing of Metallic Materials (E8-78)," Annual Book of ASTM Standards, pt. 10, American Society for Testing and Materials, Philadelphia, 1978, pp. 160-174.

48. ASTM, "Standard Methods for Estimating the Average Grain Size of Metals (E112-77)," Annual Book of ASTM Standards, Pt. 11, American Society for Testing and Materials, Philadelphia, 1978, pp.205-221.

49. Siebel, E., and Gaier, M. "Untersuchen über den Einfluß der Oberflächen-beschaffenheit auf die Dauerschwingfestigkeit metallisher Bauteile (The Influence of Surface Roughness on the Fatigue Strength of Steels and Nonferrous Alloys)," V.D.I. Zeitschrift, Vol. 98, 1956, pp. 1,715-1,723. Or, Metal Progress, Vol. 73, 1958, p. 174.

50. Fellows, J.A., editor, Metals Handbook, 8th Ed., Vol. 9, American Society for Metals, Metals Park, Ohio, 1974.

APPENDIXES

APPENDIX A

SURFACE ROUGHNESS DATA

Decarburized Specimens

Specimen	Surface Roughness, u-inches
F-020	4
F-039	3
F-048	4
F-012	6
F-014	5
F-045	3
F-034	2
F-042	2
F-043	2
F-050	6

Non-Decarburized Specimens

Specimen	Surface Roughness, u-inches
F-070	4
F-061	3
F-085	3
F-062	2
F-068	5
F-074	3
F-066	3
F-052	3
F-057	2
F-067	2

APPENDIX B

MICROHARDNESS DATA

Specimen F-044, Decarburized

Distance from Surface, Inches	Hardness, HV
0.002	162
0.005	169
0.008	177
0.011	191
0.014	191
0.017	200
0.019	206
0.023	215
0.028	210
0.033	226
0.038	218
0.043	215
0.048	235
0.053	222
0.058	213
0.063	217
0.068	218
0.073	205
0.078	210
0.083	201
0.088	209
0.093	217
0.098	223
0.103	207
0.108	209
0.113	223
0.118	199
0.123	210

Specimen F-018, Decarburized

Distance from Surface, inches	Hardness, HV
0.001	155
0.005	173
0.008	173
0.011	192
0.014	205
0.017	212
0.020	207
0.023	213
0.026	210
0.031	219
0.036	230
0.043	222
0.048	227
0.053	213
0.058	223
0.063	225
0.068	211
0.073	206
0.078	210
0.083	214
0.088	207
0.093	207
0.098	202
0.103	200
0.108	206
0.113	205
0.118	212
0.123	231

Specimen F-019, Decarburized

Distance from Surface, Inches	Hardness, HV
0.003	145
0.006	170
0.009	173
0.012	165
0.015	184
0.018	184
0.021	192
0.024	192
0.027	192
0.030	202
0.033	207
0.036	209
0.040	206
0.045	199
0.050	214
0.055	201
0.060	205
0.065	205
0.070	215
0.075	211
0.080	198
0.085	206
0.090	201
0.096	201
0.101	205
0.106	198
0.111	204
0.115	200
0.120	200

Specimen F-017, Decarburized

Distance from Surface, Inches	Hardness, HV
0.003	142
0.006	165
0.009	179
0.012	181
0.015	201
0.018	202
0.021	200
0.024	217
0.027	221
0.031	206
0.036	219
0.041	226
0.046	215
0.051	215
0.056	215
0.061	214
0.066	207
0.071	206
0.076	206
0.081	205
0.086	207
0.091	208
0.096	195
0.101	219
0.111	199
0.116	203
0.121	211

Specimen F-030, Decarburized

Distance from Surface, Inches	Hardness, HV
0.002	127
0.005	150
0.008	150
0.011	160
0.014	172
0.017	193
0.020	191
0.023	193
0.026	203
0.029	203
0.032	210
0.037	211
0.042	204
0.047	210
0.052	214
0.057	218
0.062	209
0.067	217
0.072	210
0.077	199
0.082	214
0.087	217
0.092	199
0.097	208
0.102	204
0.107	212
0.112	192

Specimen F-011, Decarburized

Distance from Surface, Inches	Hardness, HV
0.004	141
0.007	153
0.010	173
0.013	168
0.016	193
0.019	180
0.022	190
0.025	200
0.028	198
0.031	201
0.034	216
0.039	202
0.044	218
0.049	201
0.054	215
0.059	206
0.064	215
0.069	210
0.074	211
0.079	215
0.084	204
0.089	198
0.094	211
0.099	211
0.104	207
0.109	208
0.114	199

Specimen F-056, Non-decarburized

Distance from Surface, Inches	Hardness, HV
0.002	205
0.005	214
0.008	219
0.011	220
0.014	229
0.017	221
0.020	210
0.023	220
0.032	215
0.035	226
0.040	217
0.045	220
0.050	225
0.055	212
0.060	203
0.065	211
0.070	209
0.075	201
0.080	206
0.085	219
0.090	214
0.095	198
0.100	192
0.105	212
0.115	193
0.120	206
0.125	200

Specimen F-083, Non-decarburized

Distance from Surface, Inches	Hardness, HV
0.002	222
0.005	210
0.008	220
0.011	228
0.014	221
0.017	222
0.020	214
0.023	213
0.026	217
0.029	225
0.032	217
0.037	222
0.042	221
0.047	204
0.052	208
0.057	201
0.062	210
0.067	203
0.072	205
0.077	214
0.082	200
0.087	207
0.092	211
0.097	203
0.102	206
0.107	191
0.112	191
0.117	191

Specimen F-062, Non-decarburized

Distance from Surface, Inches	Hardness, HV
0.005	229
0.008	244
0.011	245
0.014	240
0.017	234
0.020	228
0.023	228
0.027	230
0.032	218
0.037	212
0.042	218
0.047	213
0.052	218
0.057	216
0.062	206
0.067	202
0.072	206
0.077	201
0.082	198
0.087	194
0.092	203
0.097	208
0.102	192
0.107	198
0.112	200
0.117	201
0.122	192

Specimen F-078, Non-decarburized

Distance from Surface, Inches	Hardness, HV
0.002	221
0.005	233
0.008	236
0.011	233
0.014	227
0.017	233
0.020	228
0.023	221
0.026	230
0.031	216
0.036	216
0.041	219
0.046	208
0.051	207
0.056	210
0.061	215
0.066	204
0.071	203
0.076	211
0.081	207
0.086	194
0.091	202
0.096	208
0.101	203
0.106	204
0.111	199
0.116	195
0.121	202

Specimen F-070, Non-decarburized

Distance from Surface, Inches	Hardness, HV
0.003	226
0.006	239
0.009	239
0.012	227
0.015	233
0.018	230
0.021	223
0.024	228
0.027	230
0.031	244
0.036	218
0.041	228
0.046	231
0.051	220
0.055	212
0.061	215
0.066	218
0.071	208
0.076	212
0.081	209
0.086	195
0.091	206
0.096	204
0.101	206
0.106	198
0.111	217
0.116	202
0.121	215
0.126	206

Specimen F-051, Non-decarburized

Distance from Surface, Inches	Hardness, HV
0.003	226
0.006	225
0.009	223
0.012	230
0.015	220
0.018	226
0.021	222
0.024	225
0.027	228
0.030	212
0.035	213
0.040	223
0.045	222
0.050	219
0.055	213
0.060	213
0.065	201
0.070	213
0.075	204
0.080	214
0.085	213
0.090	206
0.095	204
0.100	196
0.105	199
0.110	205
0.115	218

APPENDIX C

FATIGUE DATA

Fatigue Data for the Decarburized Specimens Tested in Bending

Specimen	Bending Stress, σ_x, ksi	Number of Cycles to Failure, N_f
F-027	107.1	1.62×10^4
F-048	107.1	1.46×10^4
F-049	107.1	1.76×10^4
F-011	85.7	1.68×10^4
F-019	85.7	1.96×10^4
F-038	85.7	2.03×10^4
F-032	85.7	3.36×10^4
F-014	71.4	6.99×10^4
F-022	71.4	7.46×10^4
F-034	71.4	7.09×10^4
F-029	71.4	7.68×10^4
F-030	57.1	5.43×10^4
F-035	57.1	1.082×10^5
F-036	57.1	1.161×10^5
F-045	57.1	1.175×10^5
F-012	42.9	4.865×10^5
F-046	42.9	1.4959×10^6
F-028	35.7	Runout
F-047	35.7	Runout

Fatigue Data for the Non-Decarburized Specimens Tested in Bending

Specimen	Bending Stress, σ_x, ksi	Number of Cycles To Failure, N_f
F-052	108.9	$1.48X10^4$
F-086	108.9	$1.98X10^4$
F-071	108.9	$2.13X10^4$
F-089	87.1	$2.41X10^4$
F-066	87.1	$2.41X10^4$
F-080	87.1	$5.53X10^4$
F-088	72.6	$1.197X10^5$
F-054	72.6	$1.191X10^5$
F-067	72.6	$1.229X10^5$
F-074	58.1	$3.209X10^5$
F-051	58.1	$4.921X10^5$
F-057	58.1	$3.133X10^5$
F-056	50.8	Runout
F-081	50.8	$2.7726X10^6$
F-058	43.5	Runout

Fatigue Data for the Decarburized Specimens Tested in Torsion

Specimen	Torsion Stress, τ_{xy}, ksi	Number of Cycles to Failure, N_f
F-024	69.5	$1.80X10^4$
F-040	69.5	$1.97X10^4$
F-041	69.5	$1.84X10^4$
F-026	53.7	$4.54X10^4$
F-037	53.7	$2.52X10^4$
F-050	53.7	$4.87X10^4$
F-017	37.9	$1.218X10^5$
F-039	37.9	$9.89X10^4$
F-044	37.9	$2.331X10^5$
F-018	31.6	$4.390X10^5$
F-033	31.6	$6.256X10^5$
F-042	31.6	$2.640X10^5$
F-020	25.3	$9.455X10^5$
F-025	25.3	$3.227X10^5$
F-031	25.3	$8.624X10^5$
F-015	22.1	$1.2247X10^6$
F-043	22.1	$1.1965X10^6$
F-021	18.9	Runout
F-013	18.9	Runout

Fatigue Data for the Non-decarburized Specimen Tested in Torsion

Specimen	Torsion Stress, σ_x, ksi	Number of Cycles to Failure, N_f
F-064	70.1	$3.15X10^4$
F-068	70.1	$3.20X10^4$
F-085	54.2	$1.154X10^5$
F-059	54.2	$1.145X10^5$
F-055	54.2	$7.89X10^4$
F-078	41.4	$2.848X10^5$
F-062	41.4	$1.896X10^5$
F-061	41.4	$3.131X10^5$
F-083	35.1	$5.462X10^5$
F-070	35.1	$1.2478X10^6$
F-063	35.1	$1.7065X10^6$
F-082	28.7	Runout
F-079	28.7	$4.1197X10^6$
F-077	25.5	Runout
F-075	25.5	Runout

VITA

Walter Norbert Fett was born in St. Louis, Missouri on August 16, 1954. He attended Holy Family grade school and St. Mary's High School in St. Louis. In September, 1972, he attended Meramec Community College in St. Louis County, Missouri. In the Spring of 1974, he entered The University of Tennessee, Knoxville and received the Bachelor of Science degree in Metallurgical Engineering in June 1976. From July, 1976 to August, 1978, he was employed by the Tennessee Valley Authority at Chattanooga, Tennessee as Metals Engineer.

In September, 1978, Mr. Fett accepted a position as Graduate Assistant in the Department of Chemical, Metallurgical, and Polymer Engineering at The University of Tennessee, Knoxville. He received the Master of Science degree with a major in Metallurgical Engineering in March, 1982.